

Suppression of the Efficiency Roll-Off Characteristics in Solution-Processed Lanthanide-based Organic Light-Emitting Diodes

by

Afshin Shahalizad Namin

A thesis submitted to the Department of Physics, Engineering Physics and Astronomy
In conformity with the requirements for
the degree of Doctor of Philosophy

Queen's University

Kingston, Ontario, Canada

(January 2019)

Copyright © Afshin Shahalizad Namin, 2019

Abstract

Organic light-emitting diodes (OLEDs) have gained a tremendous amount of interest, due to their applications in display and solid-state lighting technologies. This interest mainly arises from the easy and inexpensive manufacturing processes for the fabrication of lightweight, transparent, flexible, and large-area devices. While OLEDs have now reached the stage of commercialization, there are still some serious issues associated with exciton-exciton and exciton-polaron annihilation mechanisms, which reduce their efficiency particularly under the high current densities required to achieve a high level of brightness. This phenomenon is known as *efficiency roll-off*. On the other hand, since most luminescent organic semiconductors are in principle four-level lasing systems, color-tunable and easy-to-manufacture optically pumped organic solid-state lasers (OSLs) have attracted a lot of attention, due to their applications in biological sensing, spectroscopy, and data communication. However, highly demanded portable electrically driven continuous-wave (CW) OSLs (organic diode lasers) have not been realized to date. This is mainly because of the above-mentioned efficiency roll-off issue under the high current densities required to achieve lasing threshold in OLEDs.

Visible-emitting trivalent lanthanide ions (Ln^{3+}) are promising emitters for OLED applications. They are also known for their excellent lasing properties, owing to their long excited-state lifetimes, favoring population inversion in optically pumped plastic lasers and amplifiers. Furthermore, near infrared (NIR)-emitting trivalent lanthanide ions are important emitters in telecommunication applications in the 900-1600 nm spectral range. Despite the fact that lanthanide-based emitters have been studied in the NIR-emitting OLEDs, their efficiency is still much lower than in their visible-emitting counterparts. Moreover, like other types of OLED, lanthanide-based devices suffer from the aforementioned efficiency roll-off mechanisms. In the

present thesis, we show enhanced efficiency from solution-processed NIR-emitting lanthanide-based OLEDs. We also demonstrate unprecedented low efficiency roll-off characteristics in both visible and NIR-emitting lanthanide-based devices.

This thesis is dedicated to my wonderful parents, siblings, and lovely wife.

For their love and endless support.

Organization of the Thesis

Chapter 1 is an overview on the emission properties of luminescent organic semiconductors and lanthanide-based emitters in OLEDs and their lasing properties in optically pumped lasers, the optical losses limiting the light outcoupling efficiency of OLEDs, exciton-exciton and exciton-polaron annihilation mechanisms causing the efficiency roll-off issue, magnetic field effects in OLEDs, and plasmonic nanostructures. In Chapter 2 and Chapter 3, the results for solution-processed NIR-emitting lanthanide-based devices with unprecedented low efficiency roll-off characteristics will be presented. Suppression of the exciton-exciton and exciton-polaron annihilation mechanisms is achieved by careful control of the charge transport as well as excitonic processes in the devices. Specifically, we will show in those chapters that employing a suitable single host material or an *exciplex-forming* co-host consisting of electron donor and electron acceptor materials can significantly improve the device performances and greatly suppress the exciton-exciton and exciton-polaron annihilation mechanisms. In Chapter 4, we will show that application of a relatively large external magnetic field not only improves the luminescence of the visible-emitting lanthanide-based devices but also remarkably suppresses the efficiency roll-off characteristics associated with the exciton-polaron annihilation. Aside from the importance of roll-off suppression, which is related to the optimization of the excitonic and charge transport processes, the efficiency of OLEDs can be improved as well through enhancing the light outcoupling efficiency by device engineering. For this reason, in Chapter 5, we will investigate the possibility of enhancing the light outcoupling efficiency of lanthanide-based devices by incorporating plasmonic gratings into their structures. Finally, in Chapter 6, we will briefly summarize the main achievements of the present thesis and provide some suggestions for the future work.

List of Publications and Conference Contributions

- 1) **Afshin Shahalizad**, Anthony D'Aléo, Chantal Andraud, Muhammad Hasnan Sazzad, Dae-Hyeon Kim, Youichi Tsuchiya, Jean-Charles Ribierre, Jean-Michel Nunzi, and Chihaya Adachi, "Near infrared electroluminescence from Nd(TTA)₃Phen in solution-processed small molecule organic light-emitting diodes", *Organic Electronics* 44, 50 (2017).
- 2) **Afshin Shahalizad**, Dae-Hyeon Kim, Sanyasi Rao Bobbara, Youichi Tsuchiya, Anthony D'Aléo, Chantal Andraud, Jean-Charles Ribierre, Jean-Michel Nunzi, and Chihaya Adachi "Enhanced Near Infrared Electroluminescence from a Neodymium Complex in Organic Light-Emitting Diodes with a Solution-Processed Exciplex Host, *Applied Physics Letters*, 114, 033301 (2019).
- 3) **Afshin Shahalizad** and Jean-Michel Nunzi "Inhibiting the triplet-Polaron Annihilation Mechanism in Organic Light-Emitting Diodes under External Magnetic Fields", 2019 (In Progress).
- 4) **Afshin Shahalizad** and Jean-Michel Nunzi "Near Infrared Electroluminescence from Solution-processed Lanthanide-based Organic Light-Emitting Diodes", the 20th Photonics North Conference, Montreal, Canada, 5-7 June, 2018.

The results presented in Chapters 2 and 3 have been previously published in the above-mentioned Reference (1) and (2) peer-reviewed journal articles, respectively. Further, the results presented in Chapter 4 will be submitted to a peer-reviewed journal for publication (Reference 3 above). The text in Chapters 2 and 3 is the same as in References (1) and (2), respectively, with some modifications to keep the consistency and coherency of the results and discussions presented in this thesis. The required permissions for reproducing the results and discussion presented in this thesis have been obtained from the co-authors in References (1) and (2). The main experimental work presented in the above-mentioned references was carried out by Afshin Shahalizad Namin. The co-authors collaborated in experimental characterization and manuscript proofreading.

Acknowledgments

I would like to thank all the people who supported me in my PhD studies. First of all, I would like to express my gratitude to Prof. Jean-Michel Nunzi for being my academic supervisor. I appreciate the time he spent on supporting my work and reviewing this thesis. His constructive feedback with valuable suggestions led to a great improvement of this thesis.

I would also like to thank all the former and current members in our group, Dr. Somayeh M. A. Mirzaee, Dr. Leila Mazaheri, Dr. Tham Adhikari, Manal Shalabi, and Raana Pooshimin. Specially, I am grateful to Dr. Sanyasi Rao Bobbara for helping me with the time-resolved measurements presented in Chapter 3 of this thesis.

I am very grateful to my co-supervisor, Prof. Ribal Georges Sabat, for being very helpful, providing me with fruitful discussions, supporting my work in his lab at the Royal Military College of Canada, and also for the careful and competent proofreading of this thesis.

I am very grateful to Prof. Chihaya Adachi and Prof. Jean-Charles Ribierre for giving me the opportunity to become an external member of their research group at the Center for Organic Photonics and Electronics Research (OPERA) at Kyushu University in Japan. I would also like to thank Dr. Youichi Tsuchiya for helping me with the electrochemical measurements (Chapter 2), and Dr. Dae-Hyeon Kim and Muhammad Hasnan Sazzad for helping me with the spectroscopic measurements and characterizations (Chapters 1 and 2) during my visit to OPERA.

Many thanks goes out to Prof. Anthony D'Aléo (Aix Marseille University, France) and Prof. Chantal Andraud (Université Claude Bernard Lyon, France) for synthesizing the NIR-emitting lanthanide complex needed in my experiments.

I am also grateful to my PhD committee members, Prof. Jun Gao, Prof. Hany Aziz, Prof. Jeffrey Giacomini, Prof. Alex Wright, and Prof. Tucker Carrington. Special thanks also goes out to the Head of the Department of Physics, Prof. Marc Dignam, to the Co-ordinator of Graduate Studies, Prof. Stéphane Courteau, to the Graduate Program Assistant, Loanne Meldrum, and to the administrative staff of the Department of Physics at Queen's University for being extremely helpful during my PhD studies.

Finally, I am very much indebted to my friends, Hossein Seifoory, Hossein Movla, and family for their full support and encouragement during my PhD studies and during the preparation of this thesis.

Table of Contents

Abstract.....	i
Organization of the Thesis.....	iv
List of Publications and Conference Contributions.....	v
Acknowledgments.....	vi
List of Figures.....	xi
List of Tables.....	xiv
List of Abbreviations.....	xv
List of Symbols.....	xviii
Chapter 1: Introduction.....	1
1.1 Organic Light-Emitting Diodes (OLEDs): How an OLED works.....	1
1.2 Fluorescent, Phosphorescent, and Thermally Activated Delayed Fluorescent (TADF) OLEDs.....	3
1.3 Efficiency of OLEDs.....	6
1.4 Fabrication Techniques of OLEDs: Advantages of Solution-Processed Small Molecule Devices.....	7
1.5 Loss Mechanisms in OLEDs.....	9
1.5.1 Device Structural Losses.....	9
1.5.2 Efficiency Roll-off Mechanisms in OLEDs.....	11
1.5.2.1 Triplet-Triplet Annihilation.....	11
1.5.2.2 Singlet-Singlet Annihilation.....	13
1.5.2.3 Singlet-Triplet Annihilation.....	14
1.5.2.4 Triplet-Polaron Annihilation and Singlet-Polaron Annihilation.....	14
1.5.2.5 Electric Field-induced Exciton Quenching and Joule Heating.....	15
1.6. Exciplex-based OLEDs: Highly Efficient Devices with very Low Roll-off.....	15
1.7 Organic Solid-State Lasers (OSLs): Challenges and Prospects towards the Realization of Electrically Driven OSLs.....	19
1.8 Lanthanide-based Complexes.....	24
1.8.1 Sensitization of Lanthanide-based Complexes.....	24
1.8.2 Lasing Properties of Lanthanide-based Complexes.....	26
1.8.3 Lanthanide-based OLEDs.....	27

1.9 Magnetic Field Effects in OLEDs.....	29
1.9.1 The Loosely-bound Polaron Pair and Bipolaron Models.....	30
1.9.2 The Triplet Exciton-Polaron Quenching Model.....	32
1.9.3 The Δg Mechanism.....	33
1.10 Plasmonics.....	34
1.10.1 Surface Plasmon Polaritons (SPPs).....	34
1.10.2 Localized Surface Plasmon Polaritons (LSPPs).....	35
Chapter 2: Near Infrared Electroluminescence from Nd(TTA) ₃ Phen in Solution-Processed Small Molecule OLEDs with very Low Efficiency Roll-off.....	38
2.1 Experimental Details.....	39
2.1.1 Materials and Electrochemical Measurements.....	39
2.1.2 Device Fabrication and Characterizations.....	40
2.2 Results and Discussion.....	42
2.2.1 Electrochemical Measurements.....	42
2.2.2 Photophysical Characterizations.....	43
2.2.3 Characterization of the Blend Surface Morphology by AFM.....	47
2.2.4 Electroluminescence Spectra of the NIR OLEDs.....	49
2.2.5 Electrical and Efficiency Characterizations of the NIR OLEDs.....	52
2.3 Efficiency Roll-off Analysis.....	55
Chapter 3: Achieving very Low Efficiency Roll-off in Lanthanide-based OLEDs with a Solution-Processed Exciplex Host.....	59
3.1 Experimental Details.....	59
3.2 Results and Discussion.....	60
3.2.1 Characterization of the Blend Surface Morphology by AFM.....	60
3.2.2 Electroluminescence Spectrum of the NIR OLED and Photoluminescence Spectra of the Materials.....	61
3.2.3 Transient Photoluminescence Measurements.....	65
3.2.4 Electrical and Efficiency Characterizations of the NIR OLED.....	67

3.3 Efficiency Roll-off Analysis.....	69
Chapter 4: Reducing the Triplet-Polaron Annihilation Mechanism in Lanthanide-based OLEDs under External Magnetic Fields.....	71
4.1 Experimental Details and Materials.....	71
4.2 Charge Transport Process in the Devices.....	74
4.3 Sensitization Mechanism of the Eu^{3+} Ion in the Lanthanide Complex.....	75
4.4 Results and Discussion.....	77
4.4.1 Effects of the External Magnetic Field on the External Quantum Efficiency and Luminance of the Devices.....	77
4.4.2 Efficiency Roll-off Analysis.....	81
Chapter 5: Possibility of Light Extraction Enhancement by Incorporating Azobenzene Photo-Induced Plasmonic Gratings into Lanthanide-based OLEDs.....	85
5.1 Surface Relief Gratings based on Photo-Responsive Materials.....	85
5.2 Design of Plasmonic Gratings and Grating-assisted Light Outcoupling Structures.....	86
5.3 Experimental Details on the Fabrication of Plasmonic Gratings.....	88
5.4 Results and Discussion.....	90
Chapter 6: Conclusions and Future Work.....	96
Bibliography.....	100

List of Figures

Figure 1.1: (top) Schematic of conventional three-layer OLEDs, and (bottom) energy level diagram of the organic layers and the transparent (anode) and metallic (cathode) electrodes.....	2
Figure 1.2: Singlet and triplet exciton formation based on the relative spins of electrons and holes.....	4
Figure 1.3: Ground and excited-state singlet and triplet energy levels in organic materials (Jablonski diagram)	5
Figure 1.4: Jablonski diagram of TADF compounds.....	5
Figure 1.5: (a) Light trapping inside an OLED structure, (b) Enhanced light outcoupling efficiency in the presence of a corrugated (grating) structure.....	10
Figure 1.6: (a) Jablonski diagram of guest-guest triplet-triplet annihilation in a host-guest (donor-acceptor) system and (b) Dexter-type energy transfer via electron exchange in a donor-acceptor system.....	12
Figure 1.7: Förster-type energy transfer between a donor (D) molecule in the excited state and an acceptor (A) molecule in the ground state.....	13
Figure 1.8: Exciton formation and electron-hole recombination in (a) conventional and (b) exciplex OLEDs.....	16
Figure 1.9: Jablonski diagram of exciplex formation in a donor-acceptor system.....	18
Figure 1.10: (a) Simplified Jablonski diagram of a four-level fluorescent gain medium, and (b) ASE measurement setup.....	21
Figure 1.11: Sensitization of lanthanide ions via energy transfer from the ligands in a lanthanide complex (antenna effect).....	25
Figure 1.12: (a) Precession of the spin of a polaron about a hyperfine field in the absence of any external magnetic field and (b) the loosely-bound polaron pair model.....	31
Figure 1.13: Schematic diagram for positive and negative MC due to dissociation of singlet states and negative MC due to charge reaction with triplet states.....	33
Figure 1.14: Sketch of a spherical metallic nanoparticle in an external electromagnetic field propagating in the z-direction.....	37
Figure 2.1: Chemical structures of the materials used in the device structure.....	39
Figure 2.2: (a) Cyclic and (b) differential-pulse voltammograms of Nd(TTA) ₃ Phen in DMF.....	43
Figure 2.3: (a) Absorption spectrum of Nd(TTA) ₃ Phen in 1mM dichloromethane (DCM) solution, and steady-state PL spectrum of mCP neat film. (b) PL spectrum from Nd(TTA) ₃ Phen (16 wt.%) in mCP host using an excitation wavelength of 337 nm.....	45
Figure 2.4: Energy diagram of the molecular system used in this work.....	47
Figure 2.5: AFM images of the spin-coated mCP:Nd(TTA) ₃ Phen blend films for different doping concentrations: (a) 7 wt.%, (b) 13 wt.%, (c) 16 wt.% and (d) 20 wt.%.....	48

Figure 2.6: EL spectra of mCP (in the visible region) and Nd(TTA) ₃ Phen (7 wt.%) (in the NIR region) at different driving voltages in device A.....	49
Figure 2.7: The energy level alignments of the materials.....	50
Figure 2.8: EL spectra of mCP (in the visible region) and Nd(TTA) ₃ Phen (13 wt.%) (in the NIR region) at different driving voltages in device B.....	51
Figure 2.9: EL spectra of mCP (in the visible region) and Nd(TTA) ₃ Phen (16 wt.%) (in the NIR region) at different driving voltages in device C.....	51
Figure 2.10: EL spectra of mCP (in the visible region) and Nd(TTA) ₃ Phen (20 wt.%) (in the NIR region) at different driving voltages in device D.....	52
Figure 2.11: (a) Current density vs. voltage and (b) EQE vs. current density plots.....	54
Figure 2.12: T-P (blue) and T-T (red) models fitted to the normalized ($\eta_0 = 1$) experimental EQE data. $J_0 = 109.5 \text{ mA/cm}^2$, $J_e = 1130 \text{ mA/cm}^2$, $m = 0.14$	58
Figure 3.1: Chemical structures of the materials used in the device structure.....	60
Figure 3.2: AFM images of the spin-coated SPPO13:TCTA (6:3) and SPPO13:TCTA: Nd(TTA) ₃ Phen (6:3:1) blend films.....	61
Figure 3.3: Normalized NIR electroluminescence spectrum of the device recorded at 15 V.....	62
Figure 3.4: Normalized absorption spectrum of Nd(TTA) ₃ Phen, and steady-state photoluminescence spectra of SPPO13, TCTA, SPPO13:TCTA (6:3 weight ratio), and SPPO13:TCTA:Nd(TTA) ₃ Phen (6:3:1 weight ratio).....	63
Figure 3.5: Energy level alignments of the materials in the device structure.....	64
Figure 3.6: Energy diagram of the molecular system.....	64
Figure 3.7: Photoluminescence transient measurements of the host materials and blend systems.....	66
Figure 3.8: Steady-state PL spectra of SPPO13:TCTA and SPPO13:TCTA:Nd(TTA) ₃ Phen thin films....	67
Figure 3.9: (a) EQE vs. current density and (b) current density vs. voltage plots.....	68
Figure 3.10: Normalized EQE vs. current density plot fitted to the T-P model ($J_e = 299.5 \text{ mA/cm}^2$, $m = 0.8$).....	69
Figure 4.1: Chemical structures of the materials used in the devices.....	73
Figure 4.2: Energy level alignments of the materials used in the device structure.....	74
Figure. 4.3: (a) The photoluminescence (PL) spectra of SimCP2, PBD, SimCP2:PBD blend, and the absorption spectrum of Eu(DBM) ₃ Phen and (b) the electroluminescence (EL) spectrum recorded at 10 V.....	76
Figure. 4.4: Energy diagram of SimCP2 and PBD host materials, DBM and Phen ligands, and the transition energy levels of the Eu ³⁺ ion.....	76

Figure 4.5: (a) External quantum efficiency (EQE) vs. current density and (b) luminance vs. voltage characteristics of the undoped device.....	78
Figure 4.6: (a) External quantum efficiency vs. current density and (b) luminance vs. voltage characteristics of the NP-doped device.....	80
Figure 4.7: Absorption spectrum of magnetite (Fe_3O_4) nanoparticles dispersed in dichloromethane.....	80
Figure 4.8: Normalized external quantum efficiency (EQE) vs. current density plots of the undoped device under (a) $B = 0$ ($J_e = 19.63 \text{ mA/cm}^2$, $m = 0.08$), and (c) $B = 235 \text{ mT}$ ($J_e = 37.05 \text{ mA/cm}^2$, $m = 0.14$) fitted to the T-P model.....	83
Figure 4.9: Normalized external quantum efficiency (EQE) vs. current plots of the Fe_3O_4 -doped device under (a) $B = 0$ ($J_e = 20.54 \text{ mA/cm}^2$, $m = 0.08$), and (c) $B = 235 \text{ mT}$ ($J_e = 64.86 \text{ mA/cm}^2$, $m = 0.23$) fitted to the T-P model.....	83
Figure 4.10: Schematic of singlet-polaron and triplet-polaron annihilation.....	84
Figure 5.1: Molecular structures of Azobenzene-based chromophores can change in response to light and temperature.....	86
Figure 5.2: Light incident on a 1D metallic diffraction grating.....	87
Figure 5.3: Chemical structure of the material used for the fabrication of plasmonic gratings.....	89
Figure 5.4: Optical setup for surface relief grating inscription.....	89
Figure 5.5: Reflectance SPR spectra of Au-coated 1D surface plasmon gratings with different periods: (a) $\Lambda=340 \text{ nm}$, SPR=616 nm; (b) $\Lambda=350 \text{ nm}$, SPR=624 nm; (c) $\Lambda=355 \text{ nm}$, SPR=636 nm; (d) $\Lambda_1= \Lambda_2=350 \text{ nm}$, SPR=626 nm.....	91
Figure 5.6: AFM images of 1D and 2D gratings. (a) $\Lambda=340 \text{ nm}$, (b) $\Lambda=350 \text{ nm}$, (c) $\Lambda=355 \text{ nm}$, (d) (Au-coated) $\Lambda_1= \Lambda_2=350 \text{ nm}$	92
Figure 5.7: Reflectance SPR spectra of Au-coated 1D surface plasmon gratings with different periods for OLEDs: (a) $\Lambda=340 \text{ nm}$, SPR=606 nm; (b) $\Lambda=350 \text{ nm}$, SPR=614 nm; (c) $\Lambda=360 \text{ nm}$, SPR=624 nm; (d) $\Lambda=370 \text{ nm}$, SPR=632 nm.....	93
Figure 5.8: 1D and 2D AFM images of the gratings with $\Lambda=370 \text{ nm}$ and SPR=632 nm.....	94
Figure 6.1: Transmittance spectrum of a 100 nm thick ITO-coated glass substrate.....	97

List of Tables

Table 2.1: Summary of the singlet and triplet energies of mCP, TTA, and Phen ligands.....	47
Table 4.1: Summary of the singlet and triplet energies of SimCP2, PBD, DBM and Phen ligands.....	77

List of Abbreviations

Abs.	Absorption
ASE	Amplified spontaneous emission
ADN	9,10-di(naphtha-2-yl)anthracene
Alq3	tris(8-quinolinolato) aluminum(III)
AFM	Atomic Force Microscope
BCP	2,9-dimethyl-4,7-diphenyl-1,10-phenanthroline
CW	Continuous-wave
CV	Cyclic voltammogram
CBP	4,4'-N,N'-dicarbazole-biphenyl
D-Fluo.	Delayed-fluorescence
DFB	Distributed feedback
DCM2	4-(dicyanomethylene)-2-methyl-6-julolidyl-9-enyl-4H-pyran
DCM	Dichloromethane
DBM	1,3-diphenylpropane-1,3-dione
EL	Electroluminescence
EML	Emissive layer
ETL	Electron transporting layer
EBL	Electron blocking layer
EQE	External quantum efficiency
EM	Electromagnetic
Fluo.	Fluorescence
FRET	Förster resonance energy transfer
HTL	Hole transporting layer
HBL	Hole blocking layer
HOMO	Highest occupied molecular orbital
ITO	Indium Tin Oxide
IQE	Internal quantum efficiency

ISC	Intersystem crossing
IC	Internal conversion
IRF	Instrument response function
LED	Light-emitting diode
LCD	Liquid crystal display
LUMO	Lowest unoccupied molecular orbital
LMCT	Ligand-to-metal charge transfer
LiF	Lithium Fluoride
LSPP	Localized Surface Plasmon Polariton
MC	Magneto-conductance
MEL	Magneto-electroluminescence
mCP	1,3-bis(9-carbazolyl)benzene
NIR	Near infrared
OLED	Organic light-emitting diode
OSL	Organic solid-state laser
PL	Photoluminescence
PLQY	Photoluminescence quantum yield
PVD	Physical vapor deposition
Pho.	Phosphorescence
Phen	1,10-phenanthroline
PVK	Poly(N-vinylcarbazole)
PBD	2-(4-biphenyl)-5-(4-tert-butylphenyl-1,3,4-oxadiazole)
PEDOT:PSS	Poly(3,4-ethylenedioxythiophene):poly(styrene sulfonate)
PVA	Polyvinyl alcohol
p-i-n	p-doped-intrinsic-n-doped
RISC	Reverse intersystem crossing
SSET	Singlet-singlet energy transfer
S-S	Singlet-singlet
S-T	Singlet-triplet
S-P	Singlet-polaron

SPP	Surface Plasmon Polariton
SPPO13	2,7-bis(diphenylphosphoryl)-9,9'-spirobifluorene
SimCP2	Bis[3,5,-di(9H-carbazol-9-yl) phenyl]diphenylsilane
SPR	Surface plasmon resonance
TADF	Thermally activated delayed fluorescence
T-T	Triplet-triplet
TTET	Triplet-triplet energy transfer
T-P	Triplet-polaron
TTA	thenoyltrifluoroacetone
TM	Transverse magnetic
TE	Transverse electric
TPBi	2,20,2''-(1,3,5-benzinetriyl)-tris(1-phenyl-1-H-benzimidazole)
TCTA	4,4',4''-tris(carbazol-9-yl)triphenylamine
TCSPC	Time-correlated single-photon counting
UV	Ultraviolet
WOLED	White organic light-emitting diode

List of Symbols

The following symbols are listed in order of appearance in the main text.

Ir	Iridium
Pt	Platinum
Os	Osmium
ΔE_{ST}	Singlet-triplet energy difference
k_r	Radiative decay rate
k_{nr}	Non-radiative decay rate
η_{ext}	External quantum efficiency
η_{int}	Internal quantum efficiency
γ	Ratio of the emissive excitons to the injected electrons
χ	Ratio of the singlet to triplet excitons
η_{rad}	Effective radiative efficiency
η_{out}	Light outcoupling efficiency
η_L	Luminance efficiency
η_P	Power efficiency
L	Luminance
λ	Wavelength
q	Elementary charge (1.60×10^{-19} C)
h	Planck's constant (6.63×10^{-34} J.s)
c	Speed of light in vacuum (2.99×10^8 m/s)
A	OLED area
J	Current density
V	Voltage
I_{OLED}	OLED current
$R(\lambda)$	Photosensitivity of photodiode
$I_{det}(\lambda)$	Photocurrent of photodiode
Φ_0	Peak photopic eye response
$g(\lambda)$	Photopic response shape function

f	OLED-to-photodiode coupling factor
T_n	Higher-lying excited triplet state
X	Intermediate state
D	Electron donor
A	Electron acceptor
K_{TT}	Triplet-triplet annihilation rate constant
K_{SS}	Singlet-singlet annihilation rate constant
K_{ST}	Singlet-triplet annihilation rate constant
$K_{TP,e}$	Triplet-polaron rate constant for electron
$K_{TP,h}$	Triplet-polaron rate constant for hole
$P^{+/-}$	Hole/electron polaron
g	Gain
σ	Stimulated emission cross section
N	Population inversion density
J_{th}	Threshold current density
$h\nu$	Energy of photons
Ln^{3+}	Trivalent lanthanide ion
$e-h$	Electron-hole
n	Charge carrier density
μ	Charge carrier mobility
E	Electric field
B_{ex}	External magnetic field
B_{hf}	Hyperfine field
K_{ISP}	Singlet-to-triplet electron-hole polaron pair intersystem crossing rate
K_{ISC}	Singlet-to-triplet exciton intersystem crossing rate
g^-	Electron Landé-g factor
g^+	Hole Landé-g factor
μ_B	Bohr magneton
Φ	Potential

ϵ_m	Dielectric function of metal
ϵ_d	Dielectric function of dielectric material
a	Radius of metallic nanoparticle
P	Polarization
α	Polarizability
SiO_2	Silica
E_{ox}^0	Oxidation potential
E_{red}^0	Redox potential
Fc	Ferrocene
Al	Aluminum
τ	Lifetime
Fe_3O_4	Magnetite
$J_{1/2}$	Critical current density
k	Wavevector
ω	Frequency
θ_i	Angle of incidence
Λ	Grating period (spacing)
λ_{SP}	Surface plasmon excitation wavelength
λ_{em}	Emission wavelength
$\epsilon_{r,m}$	Real part of the metal dielectric function
n_d	Refractive index of dielectric
Ag	Silver
Au	Gold
1D	One-dimensional
2D	Two-dimensional

Chapter 1: Introduction

1.1 Organic Light-Emitting Diodes (OLEDs): How an OLED works

Since demonstration of the first small molecule organic light-emitting diodes (OLEDs) by Tang and VanSlyke in 1987 [1] and observation of electroluminescence (EL) from conjugated polymers by Friend et al. in 1999 [2], these devices have attracted a tremendous amount of interest, owing to their applications in full-color flat-panel displays and solid-state lighting. This interest arises from the fact that OLEDs take advantage of easy, inexpensive, and low-temperature fabrication processes in comparison to their inorganic counterparts [3-5]. Additionally, unlike rigid inorganic LEDs, the possibility of solution processing on flexible substrates enables fabrication of lightweight, large area, transparent, foldable, and wearable OLEDs [6,7]. Nowadays, OLEDs are at the stage of commercialization and several companies are currently producing highly efficient OLED TVs, smartphone OLED displays as well as white OLEDs (WOLEDs) for solid-state lighting [6-9]. Furthermore, compared with liquid crystal displays (LCDs), OLED displays exhibit higher RGB color contrast, higher brightness, higher response time, lower power consumption, and wider viewing angles [8-10]. Particularly, in contrast to LCDs, since there is no white backlight in OLEDs, OLED displays are ultra-thin and more efficient. Even though the cost of OLED production is still higher than that of LCDs, hopefully, this issue would be resolved in the near future because OLED displays have the potential to be produced by inexpensive solution processing techniques [3,4,8].

In general, there are three types of OLEDs based on the emissive organic semiconductors used in their emissive layer (EML). They include red, green, and blue-emitting small molecule, polymer, and hybrid OLEDs, where both π -conjugated polymers and small molecules are used. **Figure 1.1** shows the schematic of a conventional three-layer bottom-emitting OLED with electron

transporting layer (ETL), hole transporting layer (HTL), and EML. Charge transport and light emission mechanisms are also shown. OLEDs with more sophisticated architectures have an additional electron blocking layer (EBL) and a hole blocking layer (HBL) to confine the emissive excitons into the EML and to prevent formation of excitons¹ in the HTL and ETL. The former is fabricated between the EML and HTL and the latter is fabricated between the EML and ETL.

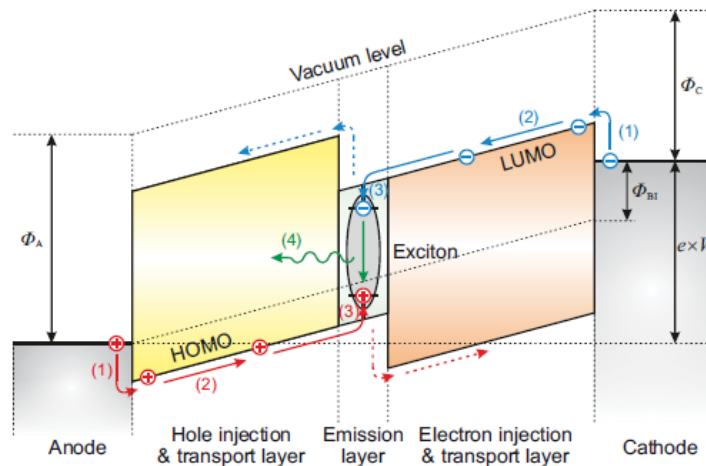
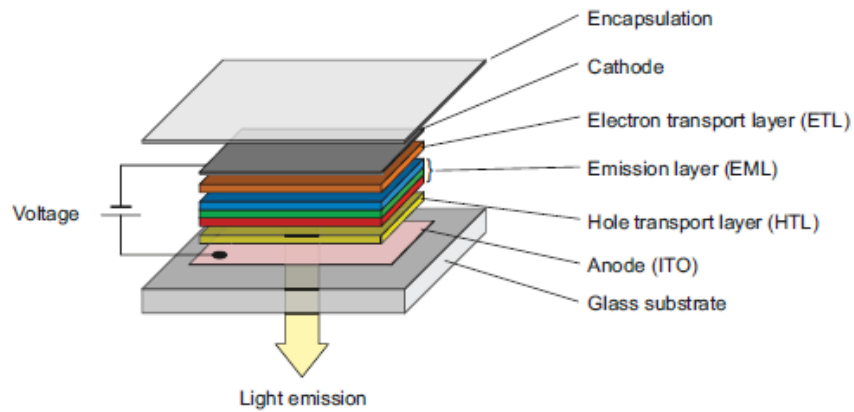


Figure 1.1: (top) Schematic of conventional three-layer OLEDs, and (bottom) energy level diagram of the organic layers and the transparent (anode) and metallic (cathode) electrodes. The electron and hole transporting layers facilitate the charge transport process in the device by reducing the energy barriers between the electrodes and the emission layer. Adapted with permission from Ref. [11].

¹ An exciton is a bound state of an electron and a hole, which are attracted to each other by the electrostatic Coulomb force.

In an OLED, a stack of organic semiconductor layers is sandwiched between an electrode with a low workfunction (cathode) and an electrode with a high workfunction (anode). The organic layers can be fabricated by thermal and/or solution processing techniques [12]. The cathode is thermally deposited onto the organic layers. In the charge transport process, electrons and holes are respectively injected from the cathode (e.g. Aluminum or silver) and anode (e.g. Indium Tin Oxide, ITO) under forward bias and then transported through the ETL and HTL. After that, electrons and holes move towards the EML where they meet to form singlet and triplet excitons. The generated excitons can then recombine radiatively to emit EL that comes out through the bottom transparent electrode. Since most emissive organic semiconductors are typically sensitive to oxygen and moisture, OLEDs have to be encapsulated in practical applications in order to avoid quenching of the radiative excitons.

1.2. Fluorescent, Phosphorescent, and Thermally Activated Delayed Fluorescent (TADF) OLEDs

Depending on the emission nature of the emissive organic material used in the EML, there are three generations of OLEDs: fluorescent (the first generation), phosphorescent (the second generation), and thermally activated delayed fluorescent (TADF) (the third generation) OLEDs. The excitation mechanism in OLEDs is electrical, so singlet and triplet excited states are created based on the relative spin orientations of injected electrons and holes, as shown in **Fig. 1.2**. In a fluorescent OLED, only 25% of the electrically generated excitons are emissive singlet excitons and 75% of the excitons are lost because the transitions from the excited triplet state T_1 to the singlet ground state S_0 is forbidden [13,14]. Therefore, while the photoluminescence quantum yield (PLQY) in fluorescent materials can be theoretically as high as 100%, the maximum internal quantum efficiency (IQE) in fluorescent devices is limited to only 25%. **Figure 1.3** displays the

singlet and triplet energy levels and the radiative and non-radiative transitions in organic materials under optical excitation. In phosphorescent OLEDs, however, all the electrically generated singlet and triplet excitons are emissive, due to the presence of heavy metals (e.g. Ir, Pt, Os) in the chemical structures of organometallic phosphorescent materials, favoring the spin-orbit coupling and subsequently making the $T_1 \rightarrow S_0$ transition possible. Thus, IQE of nearly 100% is achievable in phosphorescent devices [15]. However, phosphorescent materials have several problems such as their chemical structures being limited to expensive rare metals and difficulty for the realization of stable blue-emitting OLEDs with long lifetimes [16]. Interestingly, TADF materials (developed for the first time by the Adachi's group [17]) can exhibit IQE of 100% in the absence of any heavy metal in their chemical structures [16-22]. As the Jablonski diagram in **Fig. 1.4** shows, this is obtained because the singlet-triplet energy difference (ΔE_{ST}) in these materials is extremely small (< 0.1 eV), making the endothermic reverse intersystem crossing (RISC) (energy upconversion) from the T_1 to S_1 levels possible at room temperature.

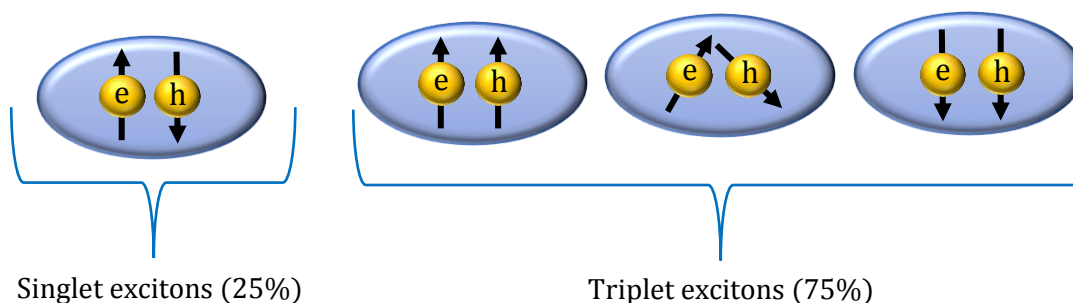


Figure 1.2: Singlet and triplet exciton formation based on the relative spins of electrons and holes.

Such a small ΔE_{ST} can be obtained by chemically attaching electron-donating and electron-withdrawing moieties in the molecular structures of TADF compounds in a way the highest occupied molecular orbital (HOMO) and the lowest unoccupied molecular orbital (LUMO) are spatially separated [16-22]. This is because ΔE_{ST} is proportional to the exchange integral and

decreases as the spatial overlap between the ground (HOMO) and excited (LUMO) state wavefunctions decreases.

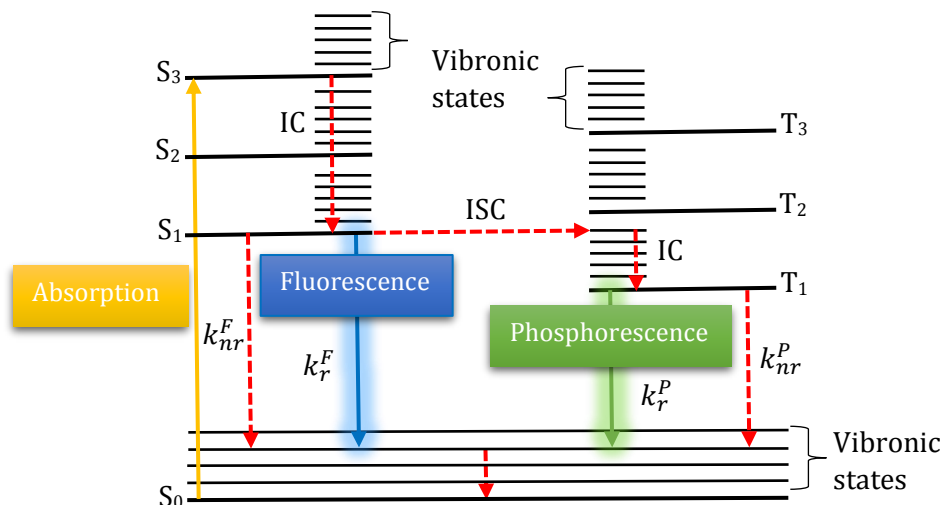


Figure 1.3: Ground and excited-state singlet and triplet energy levels in organic materials (Jablonski diagram). IC: internal conversion between singlet or triplet vibronic states, ISC: $S_1 \rightarrow T_1$ intersystem crossing, k_r^F (k_r^P) and k_{nr}^F (k_{nr}^P) are respectively radiative and non-radiative fluorescence and phosphorescence decay rates. The non-radiative transitions (IC and ISC) are shown with dashed red arrows. Apparently, since the transition energies of the singlet and triplet states are lower than that of the optical excitation energy (usually in the UV spectral region), the fluorescence and phosphorescence emission wavelengths are red shifted compared with the excitation wavelength (called *Stokes shift*). Since the $T_1 \rightarrow S_0$ is a forbidden transition in fluorescence materials, the triplet excited states have very long lifetimes (μs to ms), making them non-radiative at room temperature. Fluorescence emission and optical absorption usually occur in a few ns and fs , respectively.

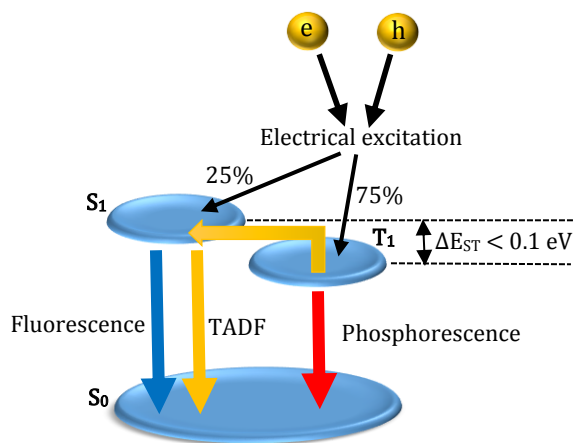


Figure 1.4: Jablonski diagram of TADF compounds.

1.3 Efficiency of OLEDs

In spite of the fact that the IQE of phosphorescent and TADF materials can reach nearly 100%, the external quantum efficiency (EQE) of OLEDs is limited by some other factors. EQE is defined as the following equation [12]:

$$\eta_{ext}(\%) = \frac{\text{Number of photons emitted}}{\text{Number of electrons injected}} \times 100 = \gamma\chi\eta_{rad}\eta_{out} = \eta_{int}\eta_{out} \quad (1.1)$$

where η_{ext} and η_{int} are respectively the EQE and IQE, γ is the ratio of the emissive excitons to the injected electrons, χ is the ratio of the singlet to triplet excitons, η_{rad} is the effective radiative efficiency (PLQY) of the emitter, and η_{out} is the light outcoupling efficiency. Therefore, in order to obtain highly efficient devices, all of these parameters should be optimized.

Additionally, performances of OLEDs can be described by luminance efficiency and power efficiency. EQE, luminance efficiency, and power efficiency can be calculated by the following equations, as proposed by Forrest et al. [23]:

$$\eta_{ext}(\%) = \frac{q \int \lambda I_{det}(\lambda) d\lambda}{hc I_{OLED} \int R(\lambda) d\lambda} \quad (1.2)$$

$$\eta_L (cd/A) = \frac{AL}{I_{OLED}} = \frac{L}{J} \quad (1.3)$$

$$\eta_P \left(\frac{lm}{W}\right) = \frac{\Phi_0 \int g(\lambda)\lambda I_{det}(\lambda)/R(\lambda) d\lambda}{f I_{OLED} V} \quad (1.4)$$

where η_L and η_P are respectively the luminance efficiency (candela per Ampere, cd/A) and power efficiency (lumen per Watt, lm/W), L (candela per meters squared, cd/m²) is the luminance (or brightness). λ , q , h , and c are the wavelength, elementary charge, Planck's constant, and speed of light in vacuum, respectively. A , I_{OLED} , J and V are the area, current, current density, and bias

voltage of the OLED, respectively. $R(\lambda)$ and $I_{det}(\lambda)$ are respectively the photosensitivity and photocurrent of the photodiode. Further, Φ_0 , $g(\lambda)$, and f are the peak photopic eye response, photopic response shape function, ($g(\lambda=555 \text{ nm}) = 1$), and OLED-to-photodiode coupling factor, respectively. In this thesis, the efficiency of visible-emitting OLEDs reported in Chapter 4 was experimentally measured by placing the devices directly on a silicon photodiode. If the OLED area is much smaller than that of the photodiode, we can consider that $f = 1$. The EL spectrum, the photosensitivity spectrum and photo-generated current of the photodiode, the human photopic response (spectrum) of the human eye, and the electrical characteristics of the devices are all taken into calculation. However, this procedure does not work for the near infrared (NIR)-emitting devices presented in Chapter 2 and Chapter 3 because NIR light is not visible by the human eye. The procedure employed for the efficiency measurements of the NIR-emitting OLEDs will be described in Chapter 2.

1.4 Fabrication Techniques of OLEDs: Advantages of Solution-Processed Small Molecule Devices

Thin films of organic semiconductor materials in an OLED can be fabricated by thermal and solution processing methods. In the former, the organic material of interest (small molecule semiconductors) is evaporated from a thermal source onto ITO-coated glass substrates by the physical vapor deposition (PVD) technique [5,12,24]. Semiconductor polymers possess very high molecular weights, so they cannot be evaporated. Thus, this method of thin film fabrication works only for small molecule compounds. It is also possible to deposit several small molecule materials simultaneously from different thermal sources by adjusting the rate of evaporation and other deposition parameters. Specifically, it is usually necessary to co-deposit two or three different small molecule materials to fabricate the EML of OLEDs. This is because emitters in OLEDs are

typically required to be doped into suitable host materials to obtain efficient host-to-guest energy transfer and to prevent concentration quenching on the guest molecules [25]. In the latter case, very low concentrations of emitters are diluted in commonly used host matrixes. Co-deposition of electron and hole transporting materials also helps to ensure a well-balanced charge transport in the EML, improving the ratio of the emissive excitons to the injected electrons (γ). Moreover, in spite of the fact that the thicknesses of the organic layers and other growth parameters can be controlled largely by evaporation technique [26], this method is expensive and complicated, requires high temperatures and vacuum pressures, and is limited to the fabrication of small-area devices [5,12,24].

In the solution processing method, solutions of small molecule materials and/or conjugated polymers are prepared in common organic solvents and then the organic thin films are fabricated onto ITO-coated glass substrates. For example, this can be done by the spin-coating, inkjet-printing, or screen-printing techniques [5,12]. After that, if a high-boiling point solvent is used, it is necessary to bake the samples on a hotplate to remove the remaining solvent. This is because any remaining solvent molecule in the voids of the solution-processed thin film can contribute to the quenching of the radiative excitons, lowering the efficiency, lifetime, and stability of the device [27,28]. Compared with thermal processing, solution processing is a more demanding technique for large-area manufacturing purposes. This method is also economically more attractive in terms of minimized material usage and its compatibility with the inexpensive aforementioned solution processing techniques, which makes the roll-to-roll fabrication of flexible and transparent devices on plastic substrates possible [29-32]. Moreover, solution-processable organic small molecule semiconductors are promising systems for OLEDs in terms of charge transport properties, device quantum efficiency, stability, and lifetime [27]. If chosen properly, analogous to thermally-

processed organic blends, a mixed host of solution-processed electron and hole transporting small molecule materials can greatly enhance the efficiency of OLEDs through providing balanced charge transport in the EML [28]. Luminescent small molecule semiconductors have several advantages over their polymer counterparts [27]: better charge balance, higher quantum efficiency and reproducibility. Thin films of solution-processed small molecule and polymer blends can also be fabricated in OLED architectures.

In the lanthanide-based OLEDs presented in the following chapters, the solution processing technique was used to fabricate the HTL, EBL, and the EML but the evaporation method was employed to fabricate the ETL and HBL of the devices. In addition, solution processing is a more appropriate method for the fabrication of lanthanide-based OLEDs because it has been previously shown that lanthanide complexes usually decompose under the high temperatures required for deposition [33].

1.5 Loss Mechanisms in OLEDs

Loss mechanisms in OLEDs can be divided into two main categories [34]: i) Device structural losses, limiting the light outcoupling efficiency: losses due to the interactions of the generated light inside the device with the cathode, and light trapping (waveguiding effects). ii) Losses due to the exciton-exciton and exciton-polaron interactions, causing so-called *efficiency roll-off*. In the following, we will briefly describe the loss mechanisms that should be avoided to achieve high-efficiency devices with low efficiency roll-off.

1.5.1 Device Structural Losses

In an OLED, a large fraction of the light generated inside the device is lost due to the total internal reflection happening in the charge transporting layers (i.e. ETL and HTL), EML, ITO, and

glass substrate [35-37]. This happens because of the difference in the refractive indexes of the organic layers, ITO, and glass substrate. In addition, more than 50% of the generated light inside an OLED is lost due to the coupling to surface plasmon polaritons (SPPs) at the cathode/ETL interface [34-39]. SPPs are described later in this chapter. Since EQE of OLEDs is influenced by the IQE and light outcoupling efficiency, these losses indeed limit the light extraction efficiency of OLEDs to ca. 20-30% [34-36]. **Figure 1.5(a)** shows the light trapping between the organic layers, the glass substrate, and the light coupling to SPPs at the cathode/organic interface. Nevertheless, the light outcoupling efficiency in OLEDs can be enhanced by using some techniques. For example, as **Fig. 1.5(a)** shows, fabrication of a micro-array with a high refractive index on the backside of the glass substrate can enhance the light outcoupling efficiency of bottom-emitting OLEDs [32,38,39]. Furthermore, as shown in **Fig. 1.5(b)**, incorporation of a dielectric or SPP diffraction grating into OLEDs can enhance their light outcoupling efficiency [40-44].

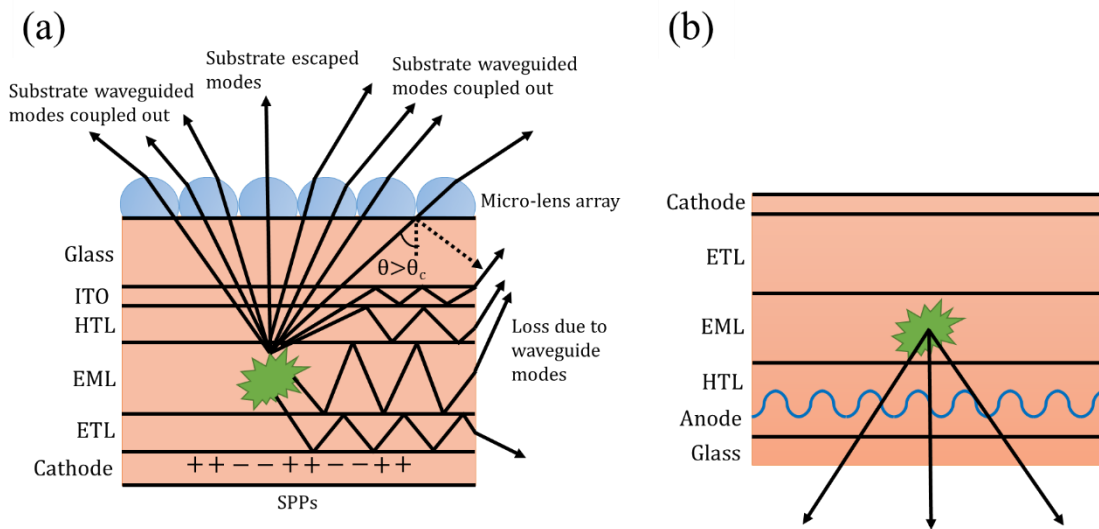


Figure 1.5: (a) Light trapping inside an OLED structure, (b) Enhanced light outcoupling efficiency in the presence of a corrugated (grating) structure.

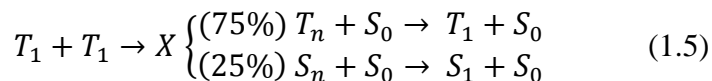
1.5.2 Efficiency Roll-Off Mechanisms in OLEDs

Apart from the device structural losses, some other losses called *efficiency roll-off* mechanisms affect the efficiency of OLEDs particularly under high currents. Efficiency roll-off mechanisms in OLEDs occur mainly due to the quenching of singlet and triplet excitons by other excitons (bimolecular annihilation processes) or by polarons¹ [45]. In host-guest systems, these loss mechanisms can occur between the molecules of the guest (guest-guest annihilation), molecules of the host (host-host annihilation), or between the molecules of the host and guest (host-guest annihilation) [46]. In the following, we briefly describe the exciton-exciton and exciton-polaron annihilation mechanisms.

1.5.2.1 Triplet-Triplet Annihilation

Triplet-triplet (T-T) annihilation is the most common quenching mechanism in phosphorescent OLEDs particularly at high current densities [47-53]. As mentioned earlier, the energy of an optically or electrically excited organic molecule can be transferred from the S_1 state to the long-lived T_1 state through intersystem crossing (ISC). In OLEDs, triplet exciton density can be very large at high current densities. The T-T annihilation process occurs when a molecule that is in the excited state T_1 absorbs a photon toward a higher-lying excited triplet state T_n . $T_1 \rightarrow T_n$ transition is a spin-allowed process. T_n state can then decay non-radiatively back to T_1 state but at least one triplet exciton is lost in this process [46]. Since one singlet exciton can be produced, the T-T annihilation may increase the efficiency of fluorescent OLEDs [54-58]. In the T-T process, the interaction between two triplet excitons creates an intermediate state X with T-T annihilation rate constant K_{TT} . This process then follows one of the two following pathways:

¹ A polaron is a quasiparticle created due to the interactions between a moving charge and atoms in a solid material.



Furthermore, since the T-T process proceeds with the short-range Dexter-type energy transfer mechanism, the interaction between triplet excitons occurs only when they are very close to each other (typically over intermolecular or intramolecular distances smaller than 2 nm [59]). The interacting triplet excitons can reside on the same molecule or on different molecules in host-guest (donor-acceptor, D-A) systems. For example, **Fig. 1.6(a)** illustrates the guest-guest T-T process in a host-guest system. Dexter-type energy transfer process is also shown in **Fig. 1.6(b)**.

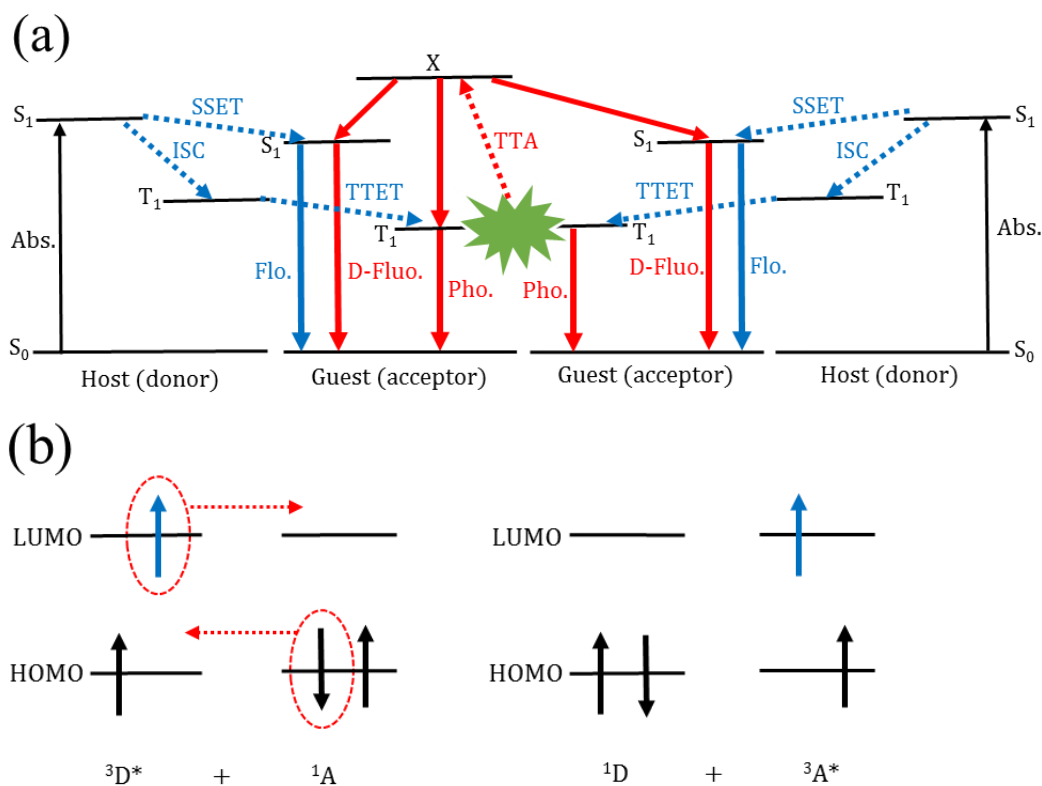


Figure 1.6: (a) Jablonski diagram of guest-guest T-T annihilation in a host-guest (donor-acceptor) system. If the emitter is fluorescent, the T-T annihilation may increase its efficiency in the device through relaxation of the intermediate state X to the singlet state S_1 . This second component of the fluorescence that is due to the T-T process is delayed. However, if the emitter is phosphorescent, the T-T process will definitely decrease its efficiency in the device because one triplet exciton is lost in this process. Abs.: absorption, ISC: intersystem crossing, SSET: singlet-singlet energy transfer, TTET: triplet-triplet energy transfer, Fluo.: fluorescence, D-Fluo.: delayed-fluorescence, X: intermediate state. (b) Dexter-type energy transfer via electron exchange in a donor-acceptor system.

1.5.2.2 Singlet-Singlet Annihilation

Singlet-singlet (S-S) annihilation is another bimolecular annihilation process that is detrimental in fluorescent OLEDs [60-62]. In phosphorescent OLEDs, there is a rapid ISC from S_1 state to T_1 state, so the S-S annihilation is usually negligible in these devices. The difference between the S-S and T-T mechanisms is that the former proceeds mainly via Förster-type energy transfer mechanism, that is, it can occur between two molecules in a long intermolecular (different molecules) or intramolecular (molecules of the same kind) distance. The S-S process can also proceed with Dexter mechanism. Förster-type energy transfer or Förster resonance energy transfer (FRET) is a long-range process, so it takes place much faster than Dexter process [63]. In the S-S process, one singlet exciton in the excited S_1 state is lost due to the energy transfer to another molecule in the excited state S_1 . **Figure 1.7** schematically shows this process. The interaction between two molecules that are in their S_1 state creates an intermediate excited state X with S-S annihilation rate constant K_{SS} . This process proceeds through the following pathway:

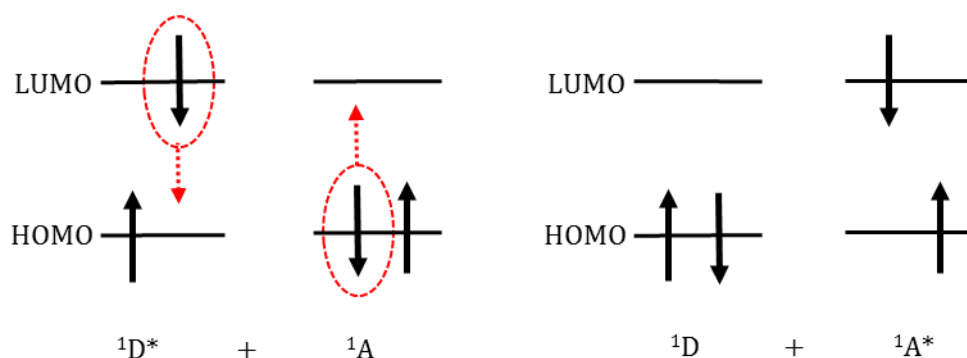
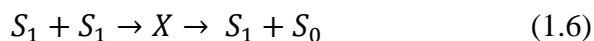
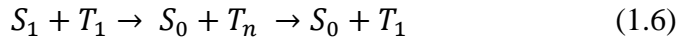


Figure 1.7: Förster-type energy transfer between a donor (D) molecule in the excited state and an acceptor (A) molecule in the ground state.

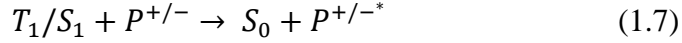
1.5.2.3 Singlet-Triplet Annihilation

Singlet-triplet (S-T) annihilation -that is more detrimental in fluorescent OLEDs than phosphorescent OLEDs- occurs under interaction of singlet excitons with triplet excitons [64-68]. In this process, analogous to the T-T annihilation, the triplet state is promoted to a higher-lying T_n state with the S-T annihilation rate constant K_{ST} , which leads to the singlet state being lost. However, the reverse process is not possible, that is, the triplet exciton cannot promote the singlet exciton to a higher-lying singlet state [45,46]. This is because the transition from triplet states to the singlet ground state is a spin-forbidden process. Similar to the S-S process, the interaction between a singlet exciton and a triplet exciton in the S-T annihilation is a Förster-type energy transfer process. Moreover, the S-T annihilation is one of the most detrimental exciton quenching mechanisms at high current densities because, analogous to the T-T annihilation, this process depends highly on the triplet exciton population that is more pronounced at high current densities [50,66]. The following pathway describes the S-T mechanism:



1.5.2.4 Triplet-Polaron Annihilation and Singlet-Polaron Annihilation

In addition to the exciton-exciton annihilation processes described above, excitons can be annihilated through interacting with free/trapped charge carriers (polarons) [69-73]. Exciton-polaron annihilation processes can cause serious efficiency-roll off particularly under high current densities in both fluorescent (singlet-polaron annihilation, S-P) and phosphorescent (triplet-polaron annihilation, T-P) OLEDs. This is because at high current densities, the number of polarons in the device is much larger than the number of generated excitons, increasing the chance for exciton-polaron interactions. The T-P rate constants for electron ($K_{TP,e}$) and hole polarons ($K_{TP,h}$) are different. The S-T and T-P processes are described as follows:



where $P^{+/-}$ and $P^{+/-*}$ represent the hole/electron polarons in the ground and excited states, respectively. Further, exciton-polaron annihilation mechanisms mainly occur via long-range Förster-type energy transfer process. This means that the excitonic energy in an exciton-polaron process is transferred to polarons because they have very broad absorption bands overlapping with the emission of the radiative excitons [74].

1.5.2.5 Electric Field-induced Exciton Quenching and Joule Heating

Electric field-induced exciton quenching refers to the dissociation of excitons into free charge carriers at high voltages [75-79]. In this process, the secondary charge carriers resulting from the dissociation of excitons escape from the EML, so they no longer contribute to the light emission in the device. This loss mechanism depends on the exciton formation process, properties of the organic materials used in the device structure, and the temperature [75-79].

Joule heating (or thermal exciton quenching) occurs due to the Ohmic losses during charge injection and transport in OLEDs [80-84]. The effects of *Joule heating* on the efficiency roll-off is very similar to exciton-exciton and exciton-polaron quenching mechanisms described earlier [46]. For this reason, a lot of care should be taken when distinguishing between *Joule heating* and other annihilation processes.

1.6. Exciplex-based OLEDs: Highly Efficient Devices with very Low Roll-Off

Even though the IQE of fluorescent OLEDs is limited to only 25%, under specific circumstances, an excited-state complex called exciplex formed between fluorescent donor and acceptor molecules can enhance this theoretical limit in the exciplex-based devices [85-91]. **Figure 1.8** displays exciton formation and electron-hole recombination in the conventional and exciplex-

based OLEDs. As **Fig. 1.8(b)** displays, at the interface of a donor-acceptor system, an exciplex complex forms only when one of the molecules is in the excited state and the other molecule is in the ground state. Therefore, exciplex complex formation -that is a bimolecular process- takes place only in the excited state and no exciplex complex can exist in the ground state [92-95]. Another important condition for exciplex formation is that the energy offset between the LUMO of the acceptor and the HOMO of the donor has to be smaller than the HOMO-LUMO bandgaps of the components [92-95]. For this reason, the emission peak of an exciplex is usually red shifted (bathochromic shift) compared to the emission peaks of the constituent donor and acceptor materials. The exciplex emission spectrum is also structure-less and broader than the emission spectra of the constituent donor and acceptor materials. The broad emission of exciplex complexes makes it particularly very suitable for the fabrication of exciplex-based WOLEDs [96-99].

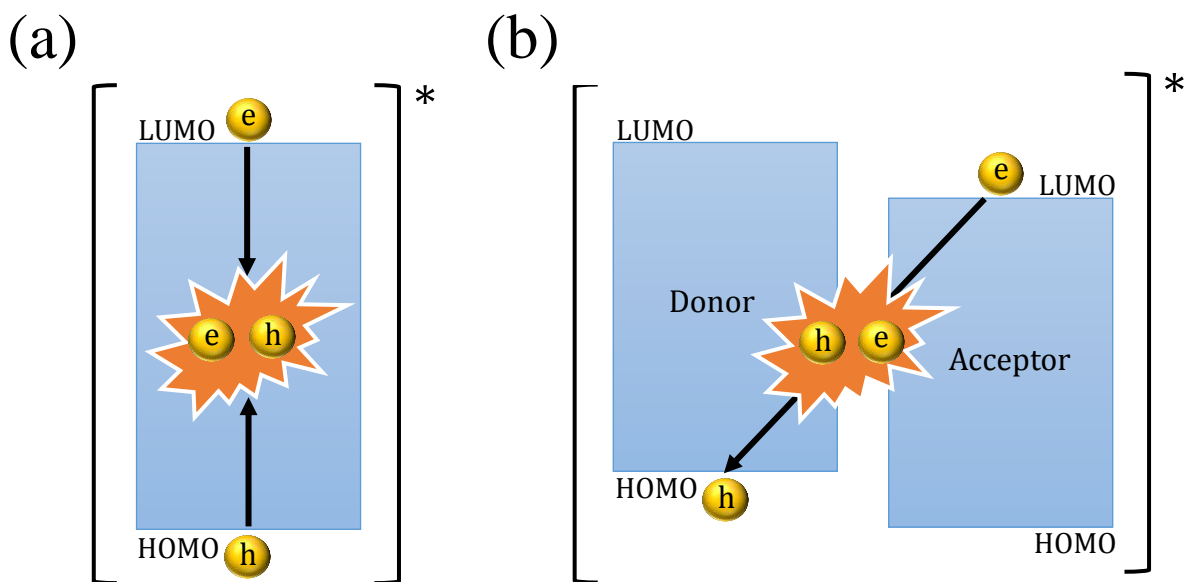


Figure 1.8: Exciton formation and electron-hole recombination in (a) conventional and (b) exciplex OLEDs. In an OLED, the HTL and ETL are the donor (D) and acceptor (A) materials that are deposited on top of each other, forming an interface for the exciplex emission. Exciplex emission can also be obtained at the molecular interfaces in a blend of a donor and an acceptor in the EML. In the latter case, the donor-acceptor blend can act as a co-host system for fluorescent, phosphorescent, or TADF dopants.

As **Fig. 1.8** shows, unlike in conventional OLEDs, electrons and holes at the donor-acceptor interface recombine without the need for overcoming the energy barrier at the interface. As a result, because exciplex emission is a barrier-free recombination process, efficient exciplex-based devices can be fabricated under low driving voltages [85-89]. Further, we pointed out in section 1.2 that TADF emission occurs when donor and acceptor molecules are chemically attached, giving rise to very small ΔE_{ST} . Analogous to TADF compounds, the HOMO and LUMO molecular orbitals are spatially separated in a donor-acceptor exciplex system [88]. For this reason, singlet and triplet exciplex energy levels are known to be very close to each other ($\Delta E_{ST} \sim 0-50$ meV), due to small electron exchange interaction [85,88,100] (see **Fig. 1.9**). Thus, analogous to TADF process, a RISC from the singlet exciplex energy level to the triplet exciplex energy level is possible, leading to a delayed fluorescence. Consequently, exciplex systems can undergo TADF emission with theoretical IQE of up to 100% but without the need for complicated chemical synthesis processes required for synthesizing TADF materials [89]. This indicates that highly-efficient exciplex-based OLEDs can be fabricated from a wide variety of fluorescent electron and hole transporting materials commonly used in conventional OLEDs, exceeding the theoretical 25%-IQE limit in conventional fluorescent devices. The Jablonski diagram in **Fig. 1.9** also shows that the singlet and triplet energy levels are usually lower than in the individual donor and acceptor materials. Moreover, exciplex emission can be obtained by blending donor and acceptor materials with bipolar small molecule materials (with donor-acceptor or donor-acceptor-donor molecular structures) [101-103]. One of the biggest advantages of using bipolar small molecule materials is that, compared to pure donor materials, they are able to transport both electrons and holes with almost the same electron and hole mobility, enhancing the charge balance efficiency in OLEDs [28,104].

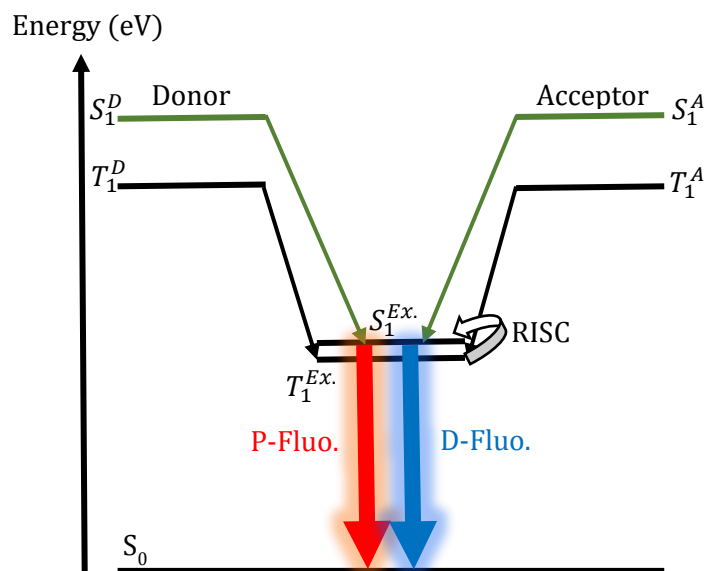


Figure 1.9: Jablonski diagram of exciplex formation in a donor-acceptor system. $S_1^D/S_1^A/S_1^{Ex}$ and $T_1^D/T_1^A/T_1^{Ex}$ represent the donor/acceptor/exciplex singlet and triplet energy levels, respectively. Similar to TADF, fluorescence from an exciplex system contains both prompt (P-Fluo.) and delayed (D-Fluo.) components.

In recent years, it has also been demonstrated that electron transporting/hole transporting and electron transporting/bipolar exciplex systems are very promising hosts for fluorescent, phosphorescent, and TADF dopants, making fabrication of highly efficient devices possible [105-109]. The advantages of using exciplex hosts in these devices are as follows: i) Exciplex OLEDs take advantage of the balanced charge transport provided by the mixed host, enhancing the charge balance efficiency. ii) The energy of an *exciplex-forming* host can be absorbed by the dopant (emitter) if the emission of the interfacial exciplexes overlaps with the absorption of the emitter. The energy transfer from the singlet and triplet exciplexes to the emitter can take place via Förster and/or Dexter processes. For efficient energy transfer from exciplexes to the emitter, the triplet energy of the constituent donor and acceptor materials and triplet exciplexes must be higher than that of the emitter [88,89]. This is necessary to confine the radiative excitons on the emitter molecules. Otherwise, guest-to-host energy-back transfer would decrease the overall efficiency of

the device. iii) As stated earlier, because the electrons and holes accumulated at the donor/acceptor interface can recombine directly without overcoming the energy barrier at the interface, very low turn-on voltages and subsequently high efficiency devices are achievable.

More importantly, this barrier-free process makes the exciplex-based OLEDs exhibit very low efficiency roll-off characteristics due to the reduced T-T and T-P mechanisms [110-113]. The detailed reason accounting for the low roll-off in these devices is as follows: As mentioned in section 1.5, in an OLED with a unipolar host, existence of an energy barrier at the ETL/EML interface makes the emission zone be very close to the interface. This consequently causes a severe roll-off due to the T-P and T-T processes because the accumulated polarons at the interface can easily interact with the radiative excitons and quench them. However, because exciplex emission is a barrier-free process, an exciplex co-host system extends the emission zone to the entire EML, reducing the accumulated polarons and triplet excitons at the interface so that the T-P and T-T processes can be reduced. This is the main motivation for Chapter 3 where we will present our results for some lanthanide-based OLEDs with an electron transporting/bipolar co-host system.

1.7 Organic Solid-State Lasers (OSLs): Challenges and Prospects towards the Realization of Electrically Driven OSLs

In recent decades, optically pumped organic solid-state lasers (OSLs) and plastic amplifiers have attracted a lot of attention [114-123]. Easy processing in both fabrication and molecular designing, potential applications as compact light sources in integrated circuits, tunable optical (tunable emission color) and electrical properties through molecular engineering, high gain coefficients due to high stimulated emission cross sections, compatibility for integration with existing technologies such as photonic circuits and waveguides, and potential applications in chemical and biological sensing and spectroscopy, and data communication are some of the most

important characteristics that make the OSL research very attractive [124-127]. In general, gain media in OSLs and amplifiers can be divided into three main categories [125]: 1) dye-doped polymers, 2) organic semiconductors (π -conjugated polymers and small molecules), and 3) rare-earth-doped polymers. One of the most important characteristics of organic semiconductors that makes them interesting gain mediums for OSLs is that most organic semiconductor materials are in principle four-level lasing systems so that the overlap between the stimulated emission and excited state absorption spectra could be very weak (because of the Stokes shift) [124,125]. **Figure 1.10(a)** shows population inversion and stimulated emission of a four-level fluorescent organic semiconductor lasing system. We know from the physics of lasers that compared to three-level systems, population inversion in four-level systems can be achieved at lower pump densities. This is because in a four-level system lasing can be obtained even when most of the molecules are in the ground state [128].

In general, a very thin layer of an organic material can absorb a large fraction ($\sim 90\%$) of the excitation photons [124-126]. Such large optical absorption can subsequently lead to a large net gain. Gain is given by $g = \sigma N$ where σ and N are the stimulated emission cross section and population inversion density (i.e. the density of electrons in the excited state), respectively. A net gain in an organic material can be achieved if the losses are overcompensated. The common stimulated cross section values for most conjugated polymers are in the order of 10^{-15} cm^{-2} , which is much higher than that in lanthanide-based complexes (10^{-23} - 10^{-21} cm^{-2}) [124]. Indeed, the larger stimulated cross section in conjugated polymers is due to the fact that π - π^* optical transitions in π -conjugated polymers are allowed but in the case of lanthanide complexes $4f$ - $4f$ transitions are parity-forbidden, making direct sensitization of lanthanide ions inefficient. We will describe the optical properties of lanthanide complexes in the next section.

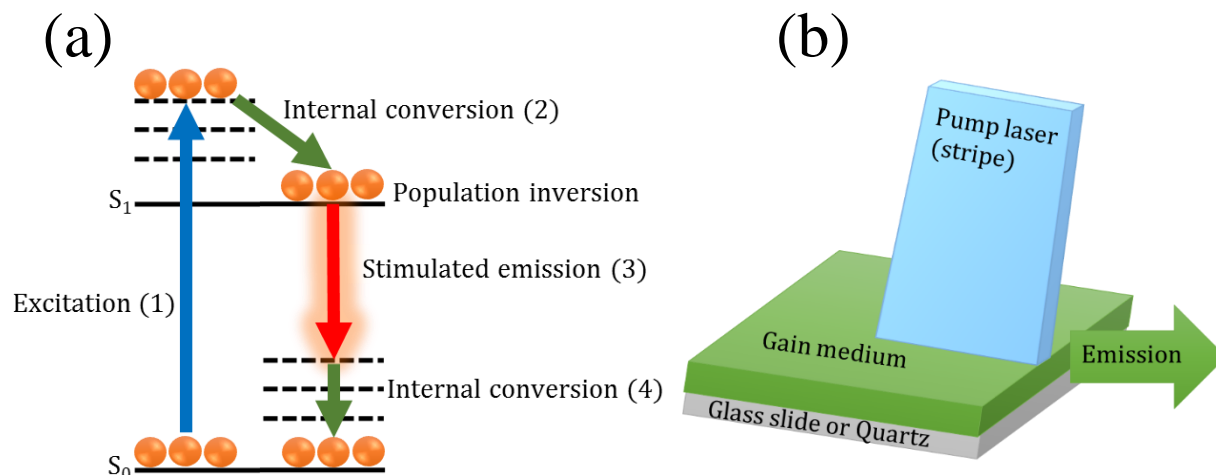


Figure 1.10: (a) Simplified Jablonski diagram of a four-level fluorescent gain medium. Self-absorption (loss) in such a system could be very small if the Stokes shift is large enough, and (b) ASE measurement setup. Most organic semiconductors are excited by UV light (e.g. by pulsed N_2 laser, 337 nm) but after illumination, they emit at longer wavelengths in the visible or near infrared spectral regions. Using a cylindrical lens, the laser beam is shaped into an extremely narrow stripe before impinging on the organic thin film deposited on a substrate. This is because in a long and narrow stripe, most of the light is emitted from the end of the stripe. The emission from the gain medium is detected from the edge of the sample.

As **Fig. 1.10(b)** shows, amplified spontaneous emission (ASE) from organic semiconductors can be obtained under optical pumping. To investigate the existence of gain in an organic material, the pump intensity is gradually increased and the output intensity (or optical power) from the edge of the film is monitored. The output intensity increases linearly at low pump intensities but when ASE is achieved, a spectral narrowing in the output photoluminescence (PL) spectrum as well as an enhanced (amplified) intensity are observed. At the threshold pump intensity, the output intensity grows exponentially. ASE photons are not coherent and thus to obtain stimulated emission, a resonator must be incorporated into the gain medium to provide feedback [129-132]. Some important issues must be considered to achieve a low-threshold ASE from organic materials [124-127]: Firstly, achieving ASE in an organic material requires a high PLQY and a high chromophore density. However, concentration quenching is a serious limitation for achieving high PLQY particularly in the case of most dyes and lanthanide ions. Concentration quenching can be avoided by increasing the spacing of the emitting molecules via blending in a host matrix. In the

case of π -conjugated polymers, concentration quenching can also be avoided using bulky side chains because bulky side groups result in a large steric hindrance between adjacent molecules, lowering the chance for formation of aggregates [133]. Secondly, the excited state lifetime (the lifetime of the lasing level) in common organic semiconductors is very short (several ns), leading to a poor population inversion. For this reason, very high pumping rates are usually required to achieve ASE threshold. Thirdly, common organic semiconductors are fluorescent materials in which only the photo-generated singlet excitons are emissive and the triplet excitons are lost. As a result, triplet population resulting from ISC from S_1 to T_1 in organic semiconductors is an unwanted mechanism reducing the number of emissive singlet excitons. Nevertheless, high singlet population can be easily achieved using short pulsed optical pumping. Short pump pulse widths ranging from 100 fs to 10 ns are required to ensure that the organic gain medium has sufficient time to recover between successive pump pulses. In addition, repetition rates ranging from 10 Hz to 10 KHz are required to allow dissipation of triplet populations between the successive pulses. Interestingly, Adachi's group has also recently reported low-threshold ASE from TADF materials [134,135].

Even though optically pumped OSLs have now reached the stage of commercialization (e.g. VISOLAS GmbH, Germany [136]), highly demanded electrically pumped OSLs have not been realized to date. To this end, OLEDs are promising candidates but there are serious issues associated with the low mobility of charge carriers in organic materials and losses due to the injection contacts [137-139]. To distinguish between an OLED and a laser, one must consider some important differences: i) In comparison to an OLED, population inversion in a laser diode requires very large injection current densities. Indeed, below a threshold current density, J_{th} , the system operates in its LED state but above the J_{th} , the system works in its laser operation state. J_{th}

is defined as $J_{th} = \frac{q}{hv} I_{th}$ where q is the elementary charge, hv is the energy of the pump photons, and I_{th} is the ASE optical pump threshold [124]. In a very crude estimation, a J_{th} on the order of $1\text{kA}/\text{cm}^2$ is required to achieve population inversion in fluorescent OLEDs. Of course, a conventional OLED cannot sustain such a high current density because it would produce a large amount of *Joule heat*, which would melt the organic materials in the device under continuous electrical pumping. Nevertheless, under very short electrical pulses, very large injection current densities (several kA/cm^2) have been recently reported by using sapphire substrates that can dissipate the *Joule heat* [140]. Despite this promising result, injection of large continuous current densities is still a big challenge. ii) Compared to an OLED, a laser system is highly influenced by the optical losses associated with the contacts (i.e. SPPs) in the cavity, as discussed in section 1.5. Because charge carriers in organic materials have very low mobility [141], it is not practically possible to move the contacts apart [125,137]. The existence of optical losses in OLEDs requires the light generated in the cavity to be amplified through the feedback provided by a resonator (e.g. a distributed feedback (DFB) resonator [129-132]) to travel several times inside the cavity to overcompensate the losses. iii) Importantly, in addition to the optical losses, efficiency roll-off processes particularly due to the accumulated triplet excitons interacting with singlet excitons and polarons shut down the continuous-wave (CW) operation under large current densities required to achieve lasing [137-139,142]. In a pioneering work, Zhang and Forrest introduced a triplet manager, ADN, into $\text{Alq}_3\text{:DCM2}$ host-guest fluorescent system to prevent triplet accumulation in their devices and they claimed CW operation over a duration of a few tens of microseconds [143]. Interestingly, Adachi's group also proposed oxygen as a triplet quencher to suppress S-T annihilation in organic semiconductor laser materials [144]. Moreover, this group reported quasi-CW operation at very high electrical pulse repetition rates (several MHz) [145,146]. However, true

CW operation in OLEDs has not been achieved to date. iv) While in all the reported optically pumped OSLs only fluorescent (and just recently TADF) emitters have been studied [114-123,134,135], the research in OLED technologies is still mainly devoted to phosphorescent OLEDs because they exhibit much higher IQE (~100%) compared to fluorescent materials (25%). As discussed earlier, phosphorescence is a forbidden transition, so to achieve lasing in a phosphorescent OLED, the laser gain area must be several times longer than in fluorescent OLEDs, which is practically impossible [124-127]. For these reasons, Samuel et al have suggested indirect pumping of organic semiconductor gain mediums by GaN diodes, as a promising alternative for electrically pumped CW operation [147]. Based on what we discussed above, an important conclusion is that even though a gain material with high a PLQY is desirable, it does not necessarily guarantee achieving CW operation in OLEDs because of the aforementioned loss mechanisms.

1.8 Lanthanide-based Complexes

1.8.1 Sensitization of Lanthanide-based Complexes

In the past decades, there has been a growing interest in using trivalent lanthanide ions (Ln^{3+}) in molecular bio-imaging [149,150], sensors [151,152], optoelectronic devices [153-156], lasers and amplifiers [157-160], owing to their extremely narrow emission bands and long excited-state lifetimes. The electronic configuration of the lanthanide ions is $[\text{Xe}]4f^n$ ($n = 0-14$), so the $4f$ orbitals are shielded by the $5S^25P^6$ subshells [161,162]. For this reason, all the lanthanide ions exhibit very similar chemical behaviors. Since $4f-4f$ transitions in lanthanide ions are parity-forbidden, these ions have very small molar absorption coefficients, making their direct excitation rather inefficient by low-power light sources [161,162]. For this reason, high-power light sources

(i.e. lasers) are employed for direct excitation of lanthanide ions. Indirect excitation of lanthanide ions is also possible by chemically attaching lanthanide ions to organic ligands (forming an *organometallic lanthanide complex*) that can absorb UV light and then transfer their energy to the central lanthanide ion via Förster and/or Dexter processes in a mechanism called *antenna effect*, or via ligand-to-metal charge transfer (LMCT) [163]. **Figure 1.11** schematically shows the sensitization of lanthanide ions through *antenna effect*. Moreover, in a lanthanide complex, the ligands protect the emission of the central lanthanide ion from being quenched by its surroundings (e.g. oxygen, moisture, solvent) [161-163].

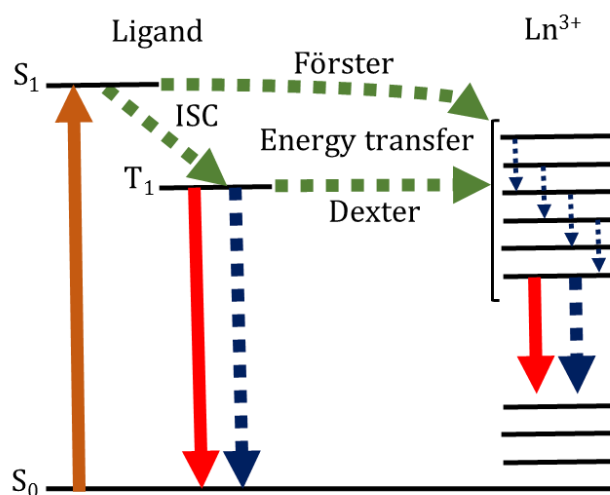


Figure 1.11: Sensitization of lanthanide ions via energy transfer from the ligands in a lanthanide complex (antenna effect): the ligand is excited, the excited state energy undergoes ISC to the triplet energy level, and then the energy from the triplet level is transferred to the lanthanide ion. Direct sensitization from the singlet level to the lanthanide ion may also be possible. Radiative and non-radiative transitions are shown with solid and dotted arrows, respectively. Ln^{3+} : trivalent lanthanide ion.

Efficient energy transfer from the ligands to the lanthanide ion requires the triplet energy levels of the ligands to be higher than the excited state level of the lanthanide ion [164-166]. Otherwise, no energy transfer from the ligands to the lanthanide ion can occur. Further, if the triplet energy levels of the ligands are energetically very close to the emission level of the lanthanide ion, energy-back transfer from the lanthanide ion to the ligands is possible, lowering the PLQY of the complex. As

a result, a great care must be taken in choosing suitable ligands to ensure efficient energy transfer from the ligands to the central lanthanide ion.

1.8.2 Lasing Properties of Lanthanide-based Complexes

Similar to organic semiconductors, lanthanide complexes are three-level or four-level lasing systems [157-160]. In comparison to organic semiconductors, the most important advantage of lanthanides for lasing systems is that they exhibit very long excited state lifetimes, favoring efficient population inversion [153]. Due to the forbidden $4f-4f$ transitions, PL lifetimes of trivalent lanthanides (\sim ms) are several orders of magnitude longer than in most semiconductor polymers (\sim ns). For this reason, lanthanides exhibit lower stimulated emission cross sections than luminescent conjugated polymers [120,126]. However, the crystal field produced by the organic ligands in an organometallic lanthanide complex makes the $4f$ transitions in the central lanthanide ion partially allowed [161-163]. The common stimulated emission cross section values in visible-emitting lanthanide complexes are on the order of 10^{-21} cm², much lower than in 4-level lasing conjugated polymers (10^{-15} cm²) [124]. Stimulated emission cross sections in NIR-emitting lanthanide complexes are even lower (10^{-22} - 10^{-23} cm²) in comparison to visible-emitting lanthanide complexes because of low PLQYs and small radiative decay rates in NIR-emitting complexes [167]. The low stimulated emission cross section increases the pump intensity required to achieve ASE from several μ J/cm² in organic semiconductors to several mJ/cm² in lanthanide complexes. Indeed, the main reason for the low PLQY in NIR-emitting lanthanide complexes is non-radiative coupling of NIR emission to the highly oscillating O-H and C-H bonds present in the organic ligands [168]. Nevertheless, the only true optically pumped CW lasing was reported by Grivas et al. for a NIR-emitting fluorinated Neodymium (Nd³⁺)-based complex (Nd(TTA)₃Phen) doped into a fluorinated host material (6-FDA) in a channel waveguide but under

a threshold pump power of about 50 mW [169,170]. The Nd³⁺ ion in the lanthanide complex was excited directly by a Ti:Sapphire laser (i.e. not through *antenna effect*). No signs of device degradation was observed for a period of 2 h under CW operation. The main purpose of the fluorination of the complex (the ligands) and host material was to prevent the NIR emission from being quenched by C-H and O-H bonds. Indeed, in *Fluorination* and *Deuteration* processes, H atoms in highly vibrating C-H and O-H bonds are replaced by heavier Fluorine (F) and Deuterium (D) atoms, respectively [171-174]. In Chapters 2 and 3, we will show our results for NIR-emitting OLEDs based on Nd(TTA)₃Phen complex.

1.8.3 Lanthanide-based OLEDs

Apart from unique emission properties of lanthanide complexes for lasing applications, lanthanide complexes have gained a lot of attention as emitters in OLEDs, owing to their high quantum efficiency and color purity [175,176]. In principle, despite the long lifetimes, achieving PLQYs of 100% in lanthanide complexes is theoretically possible because, as mentioned earlier, both singlet and triplet excited states on the ligands can contribute to the sensitization of central lanthanide ions in these complexes. For example, Hasegawa et al. have reported PLQYs of over 95% for Europium (Eu³⁺)-based complexes [177]. Particularly, Thulium (Tm³⁺), Terbium (Tb³⁺), and Eu³⁺ emit the blue (at ~ 480 nm, ¹G₄ → ³H₆), green (at ~ 545 nm, ⁵D₄ → ⁷F₄), and red (at ~ 612 nm, ⁵D₀ → ⁷F₂) primary colors, respectively, making them suitable emitters for full-color OLED displays [178-182]. There are usually more than one radiative electric dipole transition (emission peak) in trivalent lanthanide ions. Furthermore, emission of lanthanides is nearly monochromatic, which is an important requirement to achieve high color contrast in full-color display applications. Of course, in terms of color purity, lanthanides are irreplaceable by other fluorescent, phosphorescent, and TADF materials because EL spectra of devices fabricated from

these materials are very broad. Moreover, by mixing the blue, green and red colors, visible-emitting lanthanide complexes can be used in WOLEDs for solid-state lighting [183-185]. However, performances of lanthanide-based OLEDs are still much lower than other types of OLED. This is mainly because of the low electroactivity of lanthanide complexes, which makes charge carrier injection and transport rather inefficient in these devices [186]. For this reason, lanthanide-based devices usually operate under high driving voltages. This issue can be partly resolved by using sophisticated organic electron-donating and electron-withdrawing ligands, enabling efficient charge injection into lanthanide complexes in OLED architectures [186]. Additionally, analogous to other types of OLED, upon doping in a suitable host material, energy transfer via Förster and/or Dexter processes can greatly enhance the performances of lanthanide-based devices.

NIR-emitting trivalent lanthanide ions are widely studied for their applications in optical telecommunications, optical bioimaging, solar energy conversion, and photonic devices [187-193]. There are multiple emission peaks in the NIR and mid IR-emitting Neodymium (Nd^{3+}), Erbium (Er^{3+}), Ytterbium (Yb^{3+}), Holmium (Ho^{3+}), and Praseodymium (Pr^{3+}) lanthanide ions [194-202]. In most of the above-mentioned applications, external high-power lasers are utilized for direct excitation of lanthanide ions. This, of course, limits their applications in portable electrically driven devices where electrical pumping is of more interest. To this end, taking advantage of inexpensive and sophisticated manufacturing techniques used in OLED technologies, lanthanide-based NIR OLEDs may be promising candidates because they can be integrated with, for example, lab-on-chip photonic integrated circuits without the need for external lasers for excitation [126]. However, reports on NIR OLEDs based on NIR-emitting lanthanide complexes are still scarce in comparison to their visible-emitting counterparts [203-213]. Moreover, due to coupling of NIR

light to C-H and O-H bonds, performances of NIR OLEDs are still much lower than in visible-emitting devices.

1.9 Magnetic Field Effects in OLEDs

In recent years, it has been demonstrated that external magnetic fields can affect the conductivity and luminescence of organic semiconductors in OLEDs, without using any magnetic electrodes [214-218]. These phenomena are known as magneto-conductance (MC) (or magneto-resistance) and magneto-electroluminescence (MEL), respectively. As described in the following, these effects occur mainly due to the modification of polaron-spin and excited state dynamics under an applied magnetic field. This is different from spin-valve devices where spin-up and spin-down charge carriers are directly injected from magnetic electrodes [219-222]. Current density in OLEDs is given by $J = n\mu E$ where n , μ , and E are the charge carrier density, charge carrier mobility, and applied electric field, respectively. Under an external magnetic field, the conductivity of an organic semiconductor in an OLED can be modified by magnetic field-dependent carrier mobility and/or magnetic field-dependent carrier density because the electric field is not affected by the applied magnetic field [223]. Depending on the nature of organic semiconductors and device architectures, both positive (increased) and negative (decreased) MC and MEL have been observed in fluorescent, phosphorescent and TADF OLEDs [224-232]. In that context, various models have been proposed to explain the observed MC and MEL in OLEDs. These models are briefly described in the following subsections. More than one model may apply to explain the magnetic field effects in OLEDs.

1.9.1 The Loosely-bound Polaron Pair and Bipolaron Models

Unlike inorganic semiconductors where charge transport process is governed by band transport, charge transport process in organic semiconductors occurs through hopping of electrons and holes between different molecular sites, which results in a low charge carrier mobility [141]. Additionally, because molecules in organic semiconductors are bound together with weak Van Der Waals forces, they are much less rigid than inorganic semiconductors. For this reason, moving electrons and holes in an organic semiconductor can distort the molecular structure and strongly interact with phonons, giving rise to the creation of spin-1/2 quasi-particles called electron and hole polarons [233]. In an OLED, when a negative and a positive polaron come to a close proximity on different molecular sites, they form a two-particle system called *e-h polaron pair*. Polaron pair formation is the step before exciton formation. Exciton formation occurs when both negative and positive polarons are on the same molecular site. For this reason, Coulombic binding energy of singlet and triplet polaron pairs is smaller than singlet and triplet excitons.

The loosely-bound polaron pair model relies on perturbation of the singlet and triplet e-h polaron pair population in the presence of an external magnetic field (B_{ex}) [225,234,235]. In the absence of any magnetic field, the spins of paramagnetic electron and hole polarons precess about the hydrogen hyperfine fields (B_{hf}). The hyperfine fields in an organic semiconductor are created due to the magnetic moments of the hydrogen nuclei. The directions of hyperfine fields in an organic semiconductor vary on different molecular sites, so the hyperfine fields mix the reactions between paramagnetic polarons residing on the neighboring molecular sites. This leads to the formation of mixed singlet and triplet e-h polaron pairs with a 1:3 ratio (i.e. 25% singlets and 75% triplets), followed by either singlet and triplet exciton formation due to Coulomb attraction between polarons of opposite sign or dissociation of the excited states back into the constituent free charge

carriers. However, as shown in **Fig. 1.12**, an external magnetic field (B_{ex}) can perturb the spin mixing between the singlet and triplet entities because the randomly-oriented local hyperfine fields can now be aligned in the direction of the external magnetic field (if $B_{\text{ex}} \gg B_{\text{hf}}$). In this situation, the external magnetic field changes the singlet and triplet formation rates, which consequently leads to the creation of more singlet excited states by decreasing the rate of ISC. Additionally, it has been found that singlet e-h polaron pairs in OLEDs are more prone to dissociation into free polarons compared to e-h triplet polaron pairs, producing secondary electrons and holes [236-238]. Thus, an increase in the e-h singlet-to-triplet polaron pair ratio under an applied magnetic field can result in a positive MC due to the dissociation of singlet states into free polarons. On the other hand, the increased singlet population gives rise to an enhanced MEL in fluorescent devices where only singlet states are emissive.

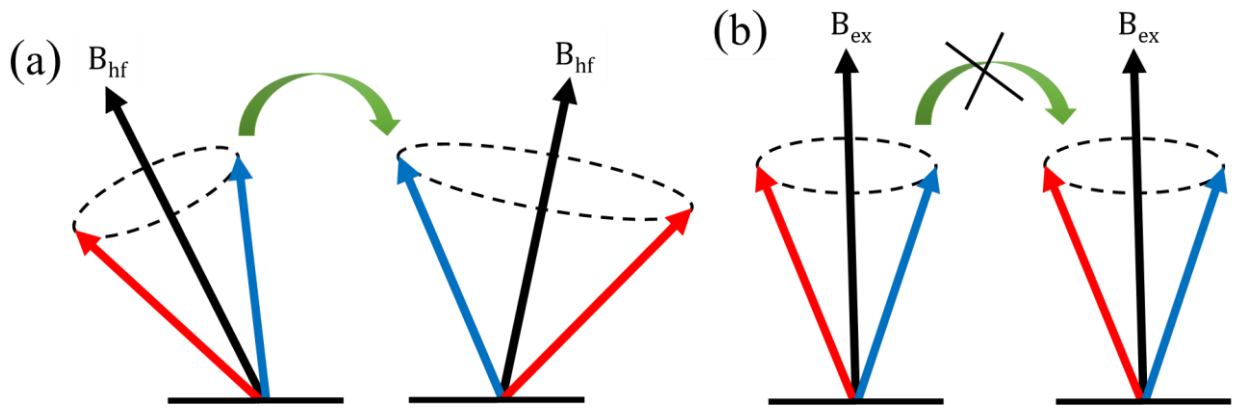


Figure 1.12: (a) Precession of the spin of a polaron about a hyperfine field in the absence of any external magnetic field, and (b) the loosely-bound polaron pair model. In this model, when an external field is applied, the local hyperfine fields are aligned in the direction of the external magnetic field (if $B_{\text{ex}} \gg B_{\text{hf}}$), preventing formation of triplet states due to the reduced ISC rate. In the bipolaron model, this also prevents hopping of charge carriers with the same spin configuration due to the spin-blockade.

In an organic semiconductor, two like-charge polarons (two positive or negative polarons) can form a bipolaron during the hopping process from localized molecular sites. Due to the strong

charge exchange interaction between the on-site polarons, formation of a singlet bipolaron is energetically more favorable than formation of a triplet bipolaron [239,240]. For this reason, under application of an external magnetic field that can align the polaron-spins in an organic semiconductor, the hopping process is perturbed because of the Pauli's exclusion principle (called *spin-blockade*) (see **Fig. 1.12 (b)**). Thus, the bipolaron mechanism can lower the polaron mobility, resulting in a negative MC and MEL.

1.9.2 The Triplet Exciton-Polaron Quenching Model

The triplet exciton-polaron quenching model can explain MC and MEL based on spin-dependent reaction of triplet excitons and free or trapped polarons. Ern and Merrifield showed that quenching of triplet excitons through interaction with paramagnetic impurities (polarons) is a magnetic field-dependent mechanism that particularly depends on the relative spins of the excitons and polarons [241]. Gillin's group also showed that if triplet excitons and polarons have opposite relative spin orientations, the triplet excitons can trap the polarons, decreasing the polaron mobility and subsequently the device conductivity [242-244]. However, if they have the same spin orientations, this process cannot occur because the trapping triplet excitonic sites are blocked (*the site-blocking effect*). Furthermore, they demonstrated that application of an external magnetic field that is expected to decrease the number of triplet excitons (i.e. the trapping sites) due to the increased singlet-to-triplet exciton ratio increased the polaron mobility and conductivity of their OLEDs. Therefore, based on what we described above, we can conclude that the net MC under application of a magnetic field is given by sum of the positive MC due to the dissociation of singlet e-h polaron pairs and negative MC due to the tapping of polarons by triplet excitons (charge reaction), as schematically shown in **Fig. 1.13**.

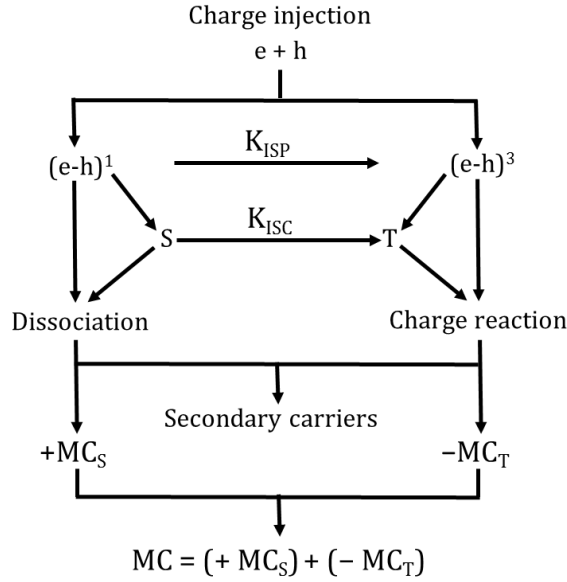


Figure 1.13: Schematic diagram for positive and negative MC due to dissociation of singlet states and negative MC due to charge reaction with triplet states. $(e-h)^1$ and $(e-h)^3$: singlet and triplet e-h polaron pairs. S and T: singlet and triplet excitons. K_{ISP} and K_{ISC} represent the singlet-to-triplet e-h polaron pair intersystem crossing rate and singlet-to-triplet exciton intersystem crossing rate, respectively.

1.9.3 The Δg Mechanism

In the presence of an applied magnetic field, the Δg mechanism relies on variation of the rate of singlet and triplet spin mixing based on the difference in the electron and hole precession Larmor frequencies, which is given by $\Delta g \mu_B B_{ex}$ where μ_B , B_{ex} , and Δg are the Bohr magneton, external magnetic field, and the difference in the electron and hole Landé-g factors (g^- and g^+), respectively [245,246]. Electrons and holes have different Landé-g factors. Thus, by changing the singlet-to-triplet ratio and subsequent dissociation of the singlet states, the Δg mechanism can modify the polaron density and MC particularly under large magnetic fields. Among the models described above, this is the only model that does not depend on random hyperfine interactions.

1.10 Plasmonics

Confinement of light at sub-wavelength scales has opened up an emerging field called plasmonics that has attracted a lot of attention due to its many applications including plasmonic lasers [247-252], biosensors and point of care applications [253-256], solar cells [257-260], light-emitting devices [261-264], nonlinear optical devices [265-269], and waveguides [270-273]. Surface plasmons are collective oscillations of free electrons (electron gas) in a metal and evanescent electromagnetic (EM) waves in a dielectric at the metal/dielectric interface [274]. There are two different types of surface plasmons: propagating *Surface Plasmon Polaritons (SPPs)* and non-propagating *Localized Surface Plasmon Polaritons (LSPPs)*, which are studied in plasmonic gratings and sub-wavelength plasmonic nanoparticles, respectively. Nevertheless, SPPs and LSPPs are similar in that they provide *confinement* and *enhancement* of electromagnetic fields at metal/dielectric interfaces beyond the diffraction limit. In the following subsections, brief descriptions of SPPs and LSPPs are given.

1.10.1 Surface Plasmon Polaritons (SPPs)

Since most metals are highly reflective at high frequencies, EM waves can propagate inside metals (in a thin layer) only at lower frequencies (i.e. in the visible and near infrared regions). Confinement of EM waves at a metal/dielectric interface leads to the creation of EM modes called SPPs propagating along the interface but evanescently confined in the perpendicular direction [274]. Additionally, SPPs cannot be excited by illuminating an EM wave directly on the interface between a metal and a dielectric. This is because the momentum of light in the dielectric is larger than that of SPPs at the interface. Thus, some special techniques are required to excite SPPs. These techniques are based on using a prism (in Otto and Kretschmann configurations) or incorporation

of gratings, providing phase matching between the momentum of light and that of the SPPs [275]. In the former, a laser beam with a transverse magnetic (TM) polarization is used to illuminate the metal/dielectric interface. The reason for using a TM-polarized light for excitation of SPPs is that transverse electric (TE) polarization that is perpendicular to the plane of propagation cannot couple to the longitudinal oscillations of surface plasmons [274,275]. In the grating method, however, it is only necessary to illuminate the surface plasmon gratings. In Chapter 5, we will describe excitation of SPPs in surface plasmon gratings and study the possibility for light extraction enhancement in grating-incorporated lanthanide-based OLEDs.

1.10.2 Localized Surface Plasmon Polaritons (LSPPs)

Localized surface plasmon polaritons (LSPPs) are non-propagating EM waves confined at the interface of a metallic nanoparticle (e.g. Ag and Au) and the surrounding dielectric [276,277]. In contrast to SPPs, LSPPs can be directly coupled to the excitation field without the need for any phase-matching technique because the momentum conservation is already fulfilled in these nanoparticles. The field enhancement mechanism for a sub-wavelength metallic nanoparticle can be addressed using the simple quasi-static approximation. Using the quasi-static approach, the interaction of a sub-wavelength spherical metal NP with an excitation EM field propagating in the z-direction $\mathbf{E} = E_0 \mathbf{e}_z$ can be investigated using the geometry shown in **Fig. 1.14**. In this configuration, the electric field in the polar coordinates inside and outside the nanoparticle is a function of r and θ , $E(r, \theta)$. By solving the Laplace equation for the potential, $\nabla^2 \Phi = 0$, and applying the boundary conditions, the potentials and the electric fields ($\mathbf{E} = -\nabla \Phi$) inside and outside the particle can be calculated, which are given by [275]:

$$\Phi_{in} = -\frac{3\varepsilon_d}{\varepsilon_m + 2\varepsilon_d} E_0 r \cos\theta \quad (1.8)$$

$$\Phi_{out} = -E_0 r \cos\theta + \frac{\varepsilon_m - \varepsilon_d}{\varepsilon_m + 2\varepsilon_d} E_0 a^3 \frac{\cos\theta}{r^2} \quad (1.9)$$

$$\mathbf{E}_{in} = \frac{3\varepsilon_d}{\varepsilon_m + 2\varepsilon_d} \mathbf{E}_0 \quad (1.10)$$

$$\mathbf{E}_{out} = \mathbf{E}_0 + \frac{3n(n.p) - p}{4\pi\varepsilon_0\varepsilon_d} \frac{1}{r^3} \quad (1.11)$$

where ε_m , ε_d , and a are the dielectric functions of the metallic nanoparticle and the surrounding dielectric medium, and the radius of the nanoparticle, respectively. \mathbf{P} is the polarization induced by the applied field, which is given by:

$$\mathbf{P} = 4\pi\varepsilon_0\varepsilon_m a^3 \frac{\varepsilon_m - \varepsilon_d}{\varepsilon_m + 2\varepsilon_d} \mathbf{E}_0 \quad (1.12)$$

The polarizability α is defined as $\mathbf{P} = \varepsilon_0\varepsilon_d\alpha\mathbf{E}_0$, which is given by:

$$\alpha = 4\pi a^3 \frac{\varepsilon_m - \varepsilon_d}{\varepsilon_m + 2\varepsilon_d} \quad (1.13)$$

As can be clearly seen from Eqn. 1.10 and Eqn. 1.11, the electric fields inside and outside the nanoparticle are enhanced compared to the external electric field \mathbf{E}_0 . Further, it is clearly seen from Eqn. 1.12 that the magnitude of \mathbf{P} can be very large if $\varepsilon_m(\omega) = -2\varepsilon_d$ (called *Fröhlich condition*), implying an enhanced polarizability. Thus, the field enhancement under the Fröhlich condition can be very remarkable. Interestingly, enhancement of EM waves at the interface between metallic nanoparticles and gain mediums has led to emergence of a new class of sub-wavelength nano-lasers called SPASERs (surface plasmon amplification by stimulated emission of radiation), where losses in metal NPs can be overcompensated by gain mediums [278].

Moreover, by incorporating suitable core-shell silver (Ag) or gold (Au) nanoparticles (e.g. silica-coated nanoparticles) into OLED structures, the field enhancement at the surface of metallic nanoparticles provides a great opportunity to improve the efficiency of these devices [262-264].

This is achieved if the surface plasmon resonance of the metallic nanoparticles overlaps with the EL of the device. It is also important to mention that uncoated-nanoparticles can easily quench the radiative excitons by converting the radiative energy into heat on their surfaces, so coating plasmonic nanoparticles with a dielectric material (e.g. silica, SiO_2) is necessary [264].

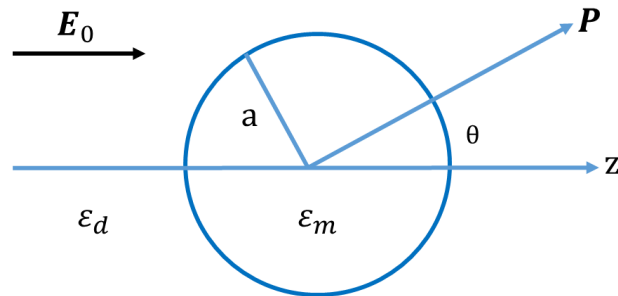


Figure 1.14: Sketch of a spherical metallic nanoparticle in an external electromagnetic field propagating in the z-direction.

Chapter 2: Near Infrared Electroluminescence from Nd(TTA)₃Phen in Solution-Processed Small Molecule OLEDs with very Low Efficiency Roll-Off

In the past, Nd³⁺-based OLEDs have been fabricated by incorporating Nd³⁺-complexes into conventional conjugated polymers by solution processing [279-281], and by the thermal evaporation in non-doped structures [282-285]. As stated in Chapter 1, compared with thermal deposition, solution processing is a more demanding technique for large-area manufacturing purposes. Solution processing is also economically a more attractive method in terms of minimized material usage and its compatibility with some inexpensive manufacturing techniques such as spin-coating, ink-jet printing, and screen-printing processes. More importantly, solution processing seems to be more appropriate for incorporating lanthanide complexes into host materials in terms of thermal and electrical stability. For example, Sano and Hamada reported a poor thermal stability for Eu(TTA)₃ at the temperatures required for evaporation [33].

Even though some solution-processed Nd³⁺-based OLEDs with polymeric hosts have been reported before [279-281], solution-processed Nd³⁺-based NIR OLEDs with small molecule hosts have not been studied up to now. 1,3-bis(9-carbazolyl)benzene (mCP) is a commonly used thermal and solution-processable material which has a triplet excited state energy of 2.9 eV, making it a very suitable host material particularly in phosphorescent OLEDs, due to reduced guest-to-host energy-back transfer [286-289]. In this chapter, we show our results for the NIR OLEDs based on blends containing mCP host doped with different concentrations of NIR-emitting Nd(TTA)₃Phen, (TTA: thenoyltrifluoroacetone, phen : 1,10-phenanthroline). The triplet energy of mCP is high enough to sensitize the Nd³⁺-complex. We show that the device containing 20 wt.% of the NIR emitter yields a maximum EQE as high as 0.022%. This EQE value is higher than the reported values for solution-processed Nd³⁺-based polymer OLEDs [280,281]. No emission from mCP is detected in this device. More importantly, in comparison to the previously reported NIR OLEDs

based on Nd^{3+} -complexes, this device suffers less from the T-T annihilation process at high current densities.

2.1 Experimental Details

2.1.1 Materials and Electrochemical Measurements

The chemical structures of the compounds used in this study are depicted in **Fig. 2.1**. The NIR emitter, $\text{Nd}(\text{TTA})_3\text{Phen}$, was synthesized using a conventional method [290]. The LUMO and HOMO energy levels of $\text{Nd}(\text{TTA})_3\text{Phen}$ were determined by electrochemical measurements. For this purpose, both the cyclic and differential-pulse voltammetry were carried out in dimethylformamide (DMF) containing $n\text{Bu}_4\text{NPF}_6$ (0.1 M) with the three-electrode system using glassy carbon working, Pt wire counter and Ag/Ag^+ reference electrodes. The electrochemical potential was calibrated using the ferrocene/ferrocenium (Fc/Fc^+) couple as an external standard.

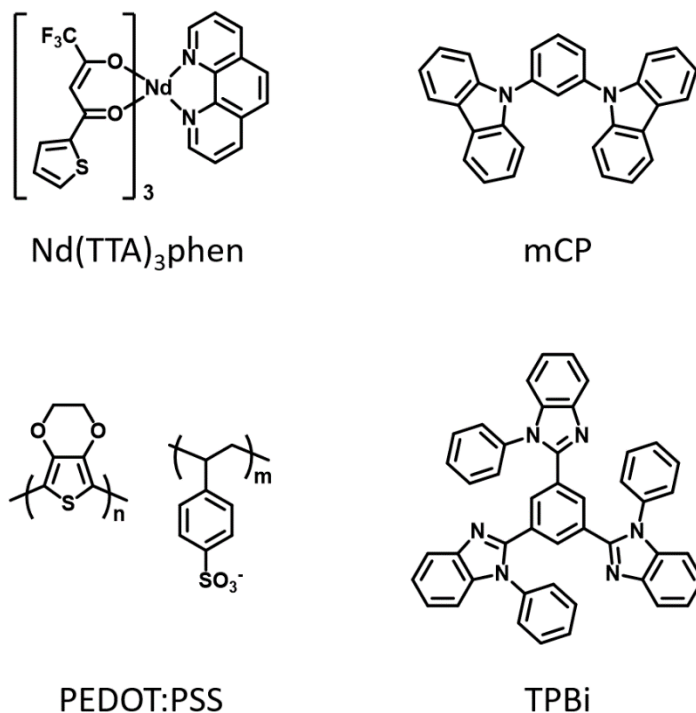


Figure 2.1: Chemical structures of the materials used in the device structures.

2.1.2 Device Fabrication and Characterizations

NIR OLEDs were fabricated on pre-patterned 100 nm thick indium tin oxide (ITO)-coated glass substrates by sequential deposition of organic layers using solution and evaporation techniques. The ITO substrates had a sheet resistance of 25 Ω /sq. The substrates were cleaned by detergent, 2-propanol, acetone, and isopropyl alcohol in an ultrasonic bath for 10 min each and then dried with nitrogen. Next, the substrates were UV-Ozone treated for 15 min. The structures of the devices are as follows: ITO/PEDOT:PSS (35 nm)/mCP:Nd(TTA)₃Phen (x = 7, 13, 16, and 20 wt%) (60 nm)/TPBi (40 nm)/LiF (0.8 nm)/Al (100 nm), where x represents the concentration of Nd(TTA)₃Phen in the mCP host. To fabricate the devices, a 30 nm thick layer of poly(3,4-ethylenedioxythiophene):poly(styrenesulfonate) (PEDOT:PSS) (Clevios Al 4083, Heraeus) was first spin coated onto the pre-cleaned ITO substrates and then baked at 140 °C for 20 min. Next, the active layers containing different concentrations of the NIR emitter doped in mCP (JIDA OPTOELECTRONICS) were spin coated onto the PEDOT:PSS layer from chloroform with a concentration of 10 mg/ml. The measured average thickness of the EML was about 60 nm. Note that the deposition of the active layers was carried out in a nitrogen-filled glove box. After that, a 40 nm thick layer of electron transporting 2,20,2''-(1,3,5-benzinetriyl)-tris(1-phenyl-1-H-benzimidazole), TPBi (JIDA OPTOELECTRONICS), was thermally deposited onto the EMLs at an evaporation rate of 0.1 nm/s under a vacuum of < 10⁴ Pa. The cathode was then fabricated by thermal evaporation of a 0.8 nm thick Lithium Fluoride (LiF) followed by 100 nm thick Al layer with an evaporation rate of 0.01 nm/s for LiF and 0.3 nm/s for Al. The active area of the devices was 4 mm². The devices were finally encapsulated with a commercially available ultraviolet curing epoxy resin and glass coverslips in a glove box. For convenience, we hereafter call the devices containing 7, 13, 16, and 20 wt.% of Nd(TTA)₃Phen as device A, B, C, and D, respectively.

Attempts to prepare devices with higher Nd^{3+} concentrations failed due to the limited solubility of the lanthanide complex in chloroform.

The current density-voltage (J-V) characteristics and EQE measurements were carried out using a semiconductor parameter analyzer (E5273A, Agilent) connected to an optical power meter (1936-C, Newport) and an InGaAs photodetector (918D, Newport, 800-1650 nm) in the ambient atmosphere. Assuming a Lambertian emission profile for the NIR light in the forward direction, the EQEs of the NIR OLEDs were calculated using the procedure employed in Ref. [291]: Assuming a Lambertian emission in the forward direction, the photo-voltage of the InGaAs photodiode created due to the NIR emission from the NIR OLEDs was converted into optical power from which the number of NIR photons was calculated. The number of electrons injected was also calculated from the device. Then, the EQE was computed by dividing the number of photons emitted to the number of electrons injected. Additionally, to make sure we recorded the data correctly, we carried out the EQE measurements very carefully in a very dark room and by subtracting even extremely small noise (the noise created by the NIR InGaAs photodiode or the electronics) from the real photo-voltage data created from the true NIR light emitted from the device. This is the method we used for the EQE measurements in the present chapter and in Chapter 3. The efficiency measurement method described in Chapter 1 works for visible-emitting OLEDs and not for NIR-emitting devices.

The EL spectra of the OLEDs in the visible spectral region were measured using an optical fiber connected to a spectrometer (PMA-12, Hamamatsu Photonics). The EL spectra of the devices in the NIR region were recorded using a NIR spectrometer (C11482GA, Hamamatsu Photonics). The absorption spectrum of $\text{Nd}(\text{TTA})_3\text{Phen}$ was recorded using a UV-Visible spectrophotometer (UV-2550, Shimadzu). The steady-state photoluminescence (PL) spectrum of mCP in the visible

spectral region was recorded by a spectrofluorometer (Fluoromax-4, Horiba Jobin Yvon). The PL quantum yields (PLQYs) of the mCP:Nd(TTA)₃Phen blended films for different doping concentrations were recorded using a UV-NIR PLQY measurement system (C13534, Hamamatsu). The PLQY measurement for the neat mCP film was recorded using an absolute PLQY spectrometer (C11347 Quantaaurus-QY, Hamamatsu). The NIR PL spectrum was measured by exciting the sample with a nitrogen laser ($\lambda = 337$ nm, repetition rate of 8 Hz, pulse width of 800 ps). Atomic Force Microscope (AFM) images of the solution-processed films were recorded by JEOL (JSPM-5400 model) scanning probe microscope. The organic thin films prepared for the photophysical and AFM measurements were spin coated on top of pre-cleaned fused silica substrates.

2.2 Results and Discussions

2.2.1 Electrochemical Measurements

Figure 2.2 shows cyclic and differential-pulse voltammograms of Nd(TTA)₃Phen in DMF solution. Since the cyclic voltammograms (CV) of the complex were observed as irreversible waves, the HOMO and LUMO levels were solely determined employing the differential-pulse voltammograms, yielding the first oxidation and reduction potentials, noted as E_{ox}^0 and E_{red}^0 . The HOMO and LUMO energy values were respectively calculated using the following equations [292, 293]:

$$\text{HOMO (eV)} = -1.4 E_{ox}^0 \text{ (vs. Fc/Fc}^+) - 4.6 \quad (2.1)$$

$$\text{LUMO (eV)} = -1.19 E_{red}^0 \text{ (vs. Fc/Fc}^+) - 4.78 \quad (2.2)$$

The use of these two equations leads to HOMO and LUMO energies of -5.4 eV and -2.5 eV, respectively, as indicated in **Fig. 2.2**. The measurement uncertainties for the HOMO and LUMO

levels are evaluated to be 0.18 and 0.2 eV, respectively [292, 293]. According to these results, the electronic energy gap of the complex is calculated to be 2.9 eV.

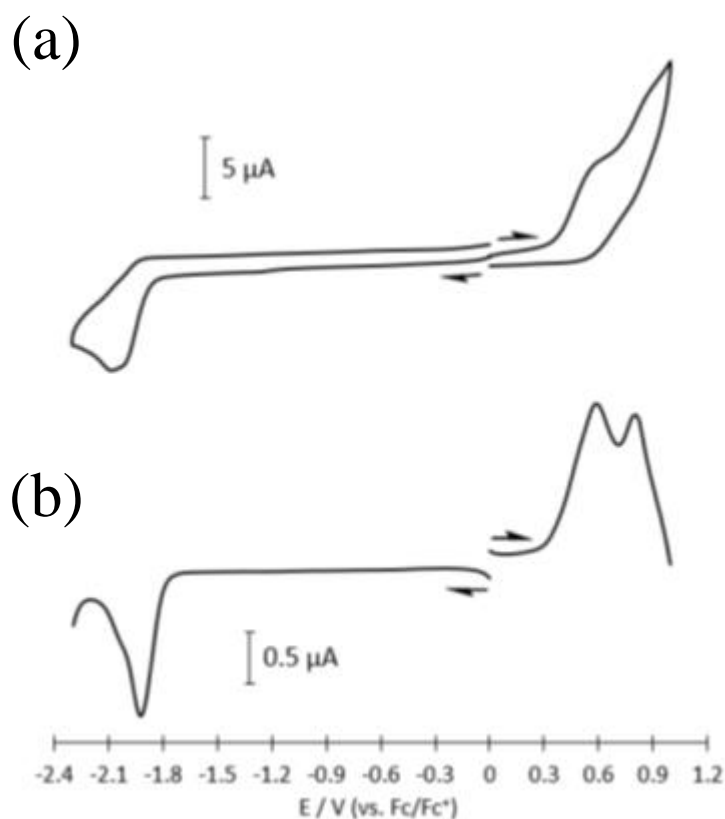


Figure 2.2: (a) Cyclic and (b) differential-pulse voltammograms of $Nd(TTA)_3Phen$ in DMF. The initial potential of all voltammograms is 0 V (vs. Fc/Fc^+). The first oxidation and reduction potentials of $Nd(TTA)_3Phen$ are respectively estimated to be 0.59 and -1.92 V (vs. Fc/Fc^+) from the peak potential in the differential-pulse voltammograms.

2.2.2 Photophysical Characterizations

In NIR OLEDs, the Nd^{3+} ions can be excited via two mechanisms: i) excitons can form on the complex through direct injection of electrons and holes into the ligands, and then the Nd^{3+} ions can be sensitized through *antennae effect* via the triplet excited states of the complex, as described in Chapter 1. ii) Singlet and triplet excitons can also form on the host molecules and then the singlet and triplet energies can be non-radiatively transferred respectively via Förster and Dexter-

type energy transfer mechanisms from the host to the ligands followed by the energy transfer to the Nd^{3+} ions from the ligands. Efficient long-range Förster-type energy transfer mechanism from the host to the guest in a host-guest system requires a considerable overlap between the absorption spectrum of the guest and the emission spectrum of the host. **Figure 2.3(a)** shows the steady-state PL spectrum of a mCP neat film and the absorption spectrum of the $\text{Nd}(\text{TTA})_3\text{Phen}$ in dichloromethane. The mCP film exhibits the expected blue fluorescence with a maximum emission wavelength at 395 nm and a PLQY of 14.5 %. The Nd^{3+} -complex shows some absorption features in the UV region, which are attributed to the absorption of the ligands. In particular, the peak centered at around 345 nm is due to the absorption of the TTA ligands. The optical energy gap of the NIR complex is about 3.2 eV, which is in good agreement with the electronic energy gap measured by electrochemistry. More importantly, a spectral overlap around 350-400 nm can be seen between the absorption and the emission spectra displayed in **Figure 2.3(a)**, indicating that Förster-type energy transfer should take place from the mCP host to the Nd^{3+} -complex. **Table 2.1** shows the singlet and triplet energy levels of mCP and $\text{Nd}(\text{TTA})_3\text{Phen}$, previously reported in the literature [294,295]. **Figure 2.4** displays the various sensitization pathways to the Nd^{3+} ion. Looking at the triplet energy values in this system, sensitization of the dopant molecules through Dexter-type energy transfer from the triplet energy level of the mCP host to the ligands cannot be excluded. It should also be stated that triplet excitons formed on the organic ligands are well confined to the NIR-emitting complex due to the much higher triplet energy of the mCP host. For instance, Steemers et al. [296] showed that when the gap between the organic ligands and the Ln^{3+} is larger than 2000 cm^{-1} (corresponding to a gap of nearly 0.25 eV), no significant energy-back transfer could occur. Based on this previous study and the values of the triplet energies provided in **Table 2.1**, we can exclude any energy-back transfer from the Nd^{3+} -complex to the mCP host.

Figure 2.3(b) shows an example of NIR PL spectrum from a mCP:Nd(TTA)₃Phen (16 wt.%) blend film. This representative sample shows the characteristic emission of Nd³⁺ with three peaks at 890 nm (⁴F_{3/2} → ⁴I_{9/2}), 1060 nm (⁴F_{3/2} → ⁴I_{11/2}), and 1330 nm (⁴F_{3/2} → ⁴I_{13/2}). To gain further insights into the photophysical properties of these mCP:Nd(TTA)₃Phen blends, PLQY of the NIR

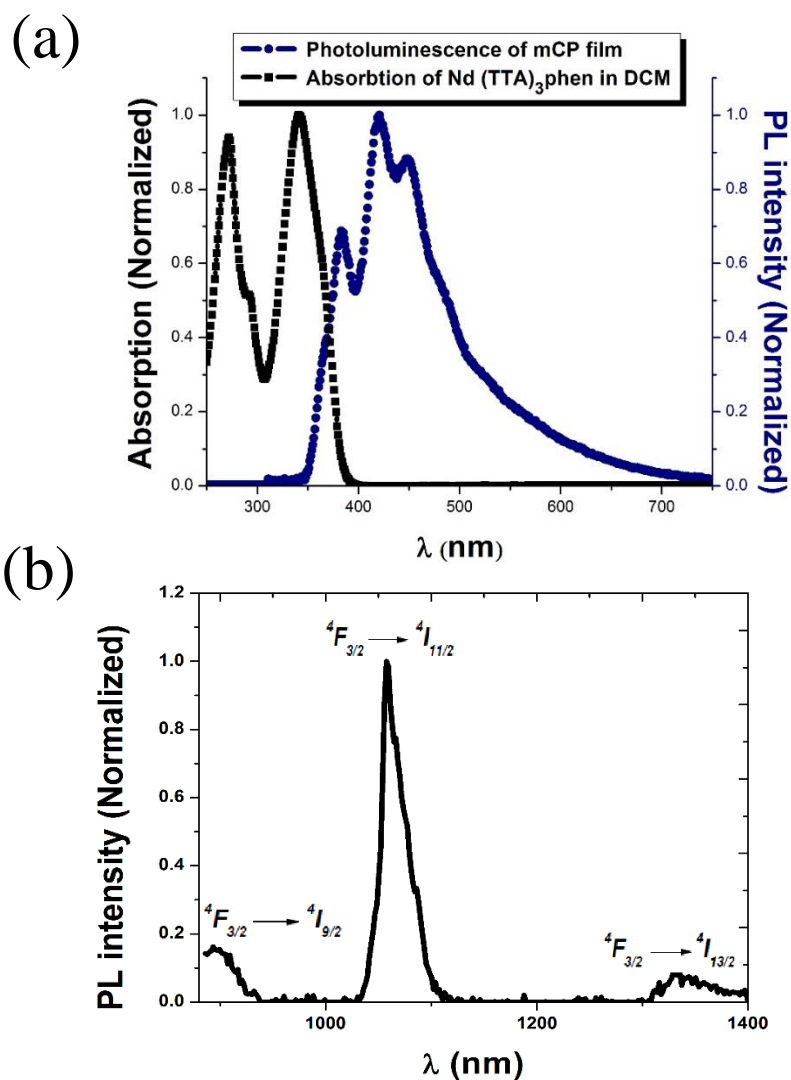


Figure 2.3: (a) Absorption spectrum of Nd(TTA)₃Phen in 1mM dichloromethane (DCM) solution, and steady-state PL spectrum of mCP neat film. (b) PL spectrum from Nd(TTA)₃phen (16 wt.%) in mCP host using an excitation wavelength of 337 nm.

emission from the Nd³⁺-complex and PLQY of the visible emission from the mCP host were measured as a function of the doping concentration. For this purpose, the blends A, B, C and D

(corresponding to concentrations of Nd(TTA)₃Phen equal to 7, 13, 16, and 20 wt.%, respectively) were photo-excited at 345 nm where both mCP host and the ligands strongly absorb light. The PLQY values for the NIR emission were measured to be 0.4% for the blend A and 0.5 % for the three other doped films. These similar values, which agree within the experimental uncertainties, indicate that the effect of doping concentration on the NIR emission efficiency is nearly the same for this range of doping concentration. Noticeably, the doping concentration was found to have a much more significant impact on the PLQY of the mCP blue emission. These PLQY values were measured to be 0.5, 0.3, 0.1 and almost 0 % for the blends A, B, C and D, respectively, which is significantly lower than the aforementioned value obtained in the mCP neat film (14.5%). The results provide clear evidence of an increase of the mCP emission when the concentration of the NIR emitter is decreased. This suggests that the Förster-type energy transfer taking place from mCP to Nd(TTA)₃Phen in these blends is not efficient enough at low doping concentrations. To gain additional insights into the energy transfer process, we also tried to examine the influence of the doping concentration on the PL decays of the mCP host emission in the blends. While the mCP neat film showed a PL lifetime of about 3.1 ns, the PL decays of the blends were too fast to be properly recorded using our experimental setup. This observation is consistent with a quenching of the host emission due to energy transfer to the NIR emitter. To the best of our knowledge, other groups have reported no PLQY value for Nd³⁺-based guest-host systems. Interestingly, according to the PLQY values measured above and assuming that both singlet and triplet excitons are involved in the electrical excitation of the Nd³⁺ ions, the theoretical maximum EQE value for the OLEDs based on these blends is calculated to be about 0.1% with the assumption of both singlet and triplet harvesting under electrical excitation.

Table 2.1: Summary of the singlet and triplet energy of mCP, TTA, and Phen ligands.

Compound	E_{singlet} (eV)	E_{triplet} (eV)	References
mCP	3.56	2.9	[294]
TTA	3.12	2.35	[295]
Phen	3.87	2.09	[295]

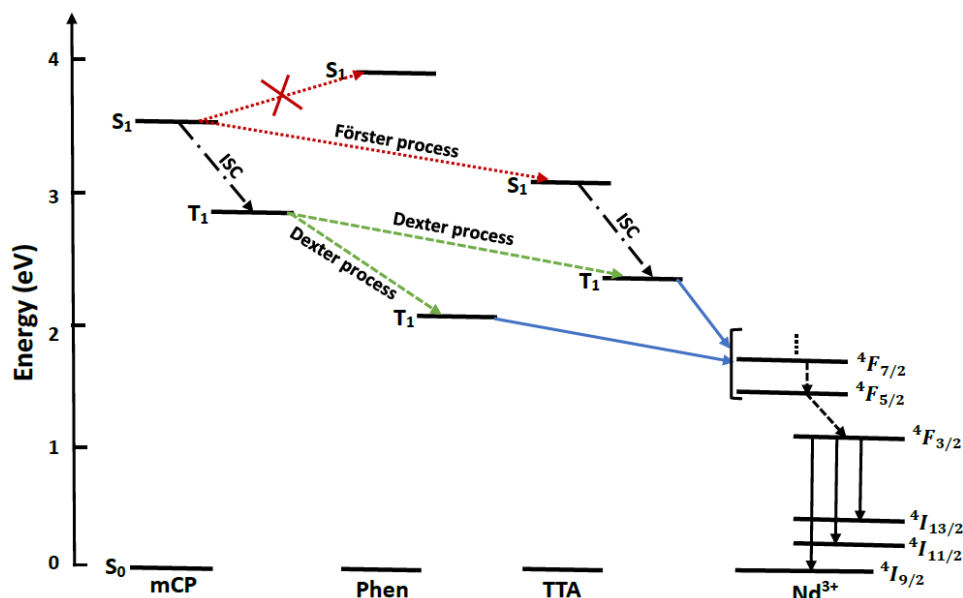


Figure 2.4: Energy diagram of the molecular system used in this work. The first excited singlet (S_1) and triplet (T_1) state energy of mCP and $\text{Nd}(\text{TTA})_3\text{Phen}$ are indicated. ISC corresponds to intersystem crossing. The forbidden f - f transitions of the lanthanide ion are shown with dashed arrows.

2.2.3 Characterization of the Blend Surface Morphology by AFM

Previous works have highlighted the importance of having a low surface roughness on the EML for achieving high EQE values in OLEDs [25,297]. Surface roughness should be minimized to prevent leakage current and guarantee a stable film morphology upon thermal annealing [28]. Selection of suitable host material is also of great importance since it must possess, in addition to good semiconducting properties, a good solubility in common organic solvents and a high thermal stability under thermal annealing to prevent recrystallization [27,28].

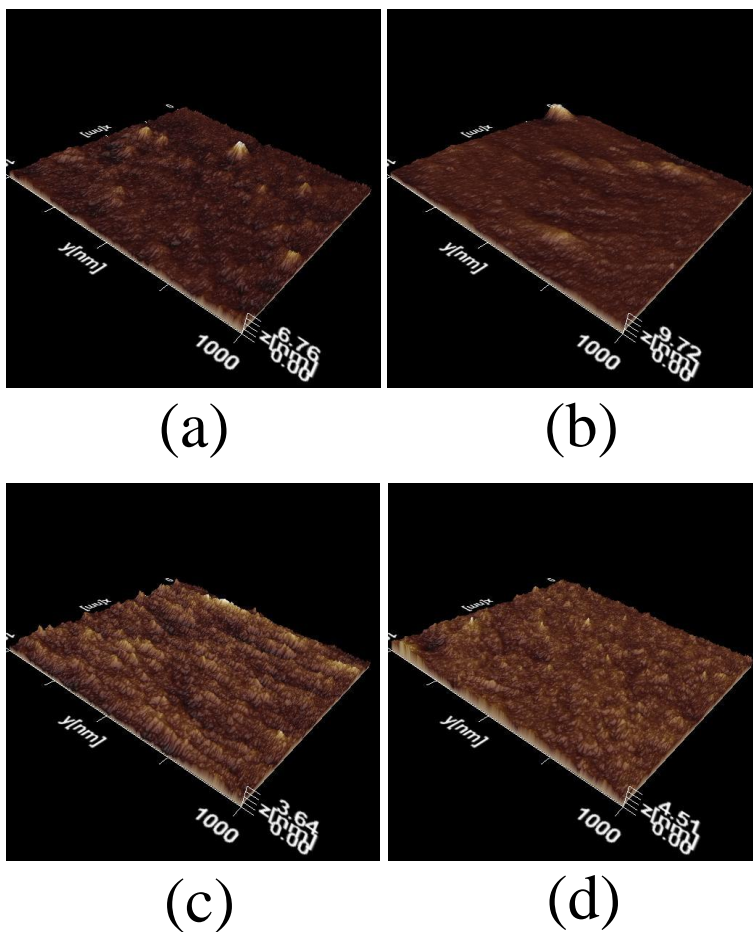


Figure 2.5: AFM images of the spin-coated mCP:Nd(TTA)₃Phen blend films for different doping concentrations: (a) 7 wt.%, (b) 13 wt.%, (c) 16 wt.% and (d) 20 wt.%. The root-mean-square (RMS) roughness values for a, b, c and d are 0.57, 0.54, 0.45 and 0.34 nm, respectively.

Even though mCP is highly soluble in chloroform, it tends to crystallize easily upon thermal annealing, exhibiting a hill-like surface morphology [27]. In that context, we characterized the surface morphologies of the blends A, B, C and D using AFM. As shown in **Fig. 2.5**, the root-mean-square (RMS) roughness values of the blend films were measured to be lower than 1 nm, indicating that the surface roughness should not affect significantly the OLED performances. These AFM images do not show any clear signs of phase separation between the host and guest molecules, suggesting a good and homogeneous dispersion of the Nd³⁺ complex in the mCP host.

2.2.4 Electroluminescence Spectra of the NIR OLEDs

The EL spectra of mCP and Nd(TTA)₃Phen complex for device A at different driving voltages are shown in **Fig. 2.6**. This device emits light in the visible and NIR regions through injection of electrons and holes into the EML followed by the formation and recombination of excitons on both the mCP and Nd(TTA)₃Phen molecules. Observation of the visible emission from mCP indicates that the Förster-type energy transfer mechanism from the host molecules to the dopant molecules is not efficient enough to quench the emission of the host material at the doping concentration of 7 wt.%. This statement is fully supported by the PLQY measurements described earlier, which indicate a partial energy transfer for such a low dye concentration.

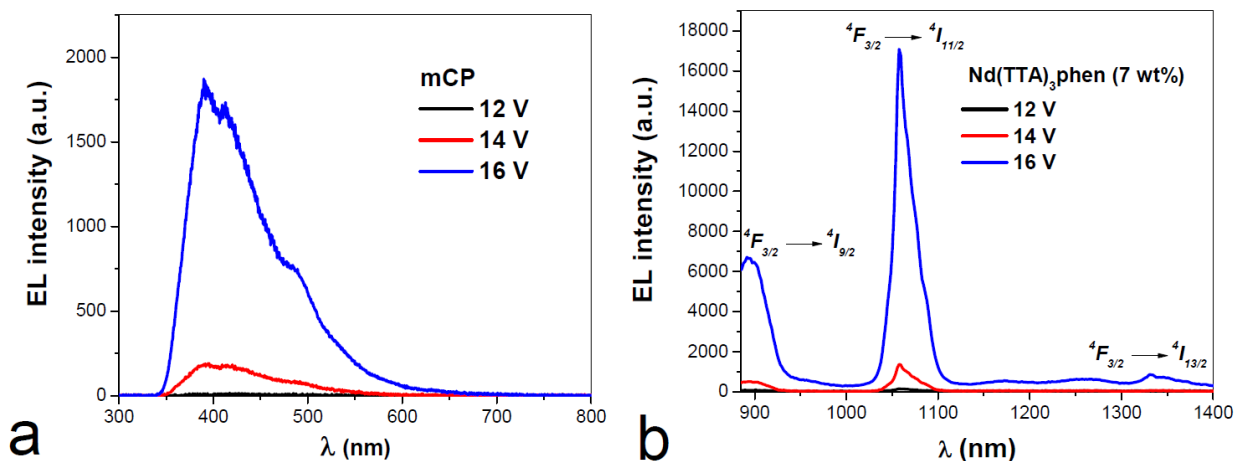


Figure 2.6: EL spectra of mCP (in the visible region) and Nd(TTA)₃Phen (7 wt.%) (in the NIR region) at different driving voltages in device A.

As a consequence, we attribute most of the emission from this device to the direct exciton formation on the Nd(TTA)₃Phen molecules. This interpretation is in good consistency with the low energy barriers for electron and hole injection respectively from TPBi and PEDOT:PSS to the LUMO and HOMO levels of the Nd(TTA)₃Phen molecules, as shown in **Fig. 2.7**.

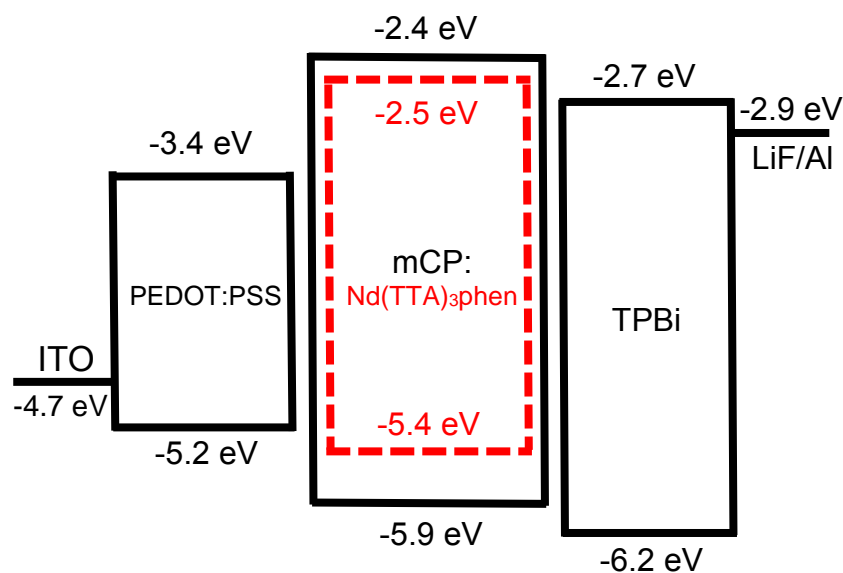


Figure 2.7: The energy level alignments of the materials.

Figures 2.8, 2.9 and **2.10** show the EL spectra measured in device B, C, and D, respectively. Similar to device A, these devices are found to strongly emit in the NIR region with the characteristic emission spectrum from Nd^{3+} . More importantly, these EL spectra show a gradual decrease of the mCP host emission intensity as the concentration of $\text{Nd}(\text{TTA})_3\text{Phen}$ molecules is increased. This is consistent with the PLQY results and can be explained by the improvement of the Förster-type energy transfer from the host to the guest molecules when increasing the density of the NIR emitter. When looking at the energy levels of the different materials used in the devices in **Fig. 2.7**, it can be seen that the HOMO and LUMO of $\text{Nd}(\text{TTA})_3\text{Phen}$ are located within the HOMO and LUMO levels of mCP and that the LUMO of TPBi is close to that of $\text{Nd}(\text{TTA})_3\text{Phen}$. This suggests that holes and electrons can be directly trapped on the emitter molecules. In that case, by increasing the concentration of the emitter in the blend, most of the charge carriers can be directly injected into the organic ligands, thus favoring direct exciton formation on the Nd^{3+} -

complex. For instance, in the case of device D, the EL from the mCP host is completely quenched, which is presumably due to the improved direct exciton formation on Nd(TTA)₃Phen and a more efficient host-to-guest energy transfer.

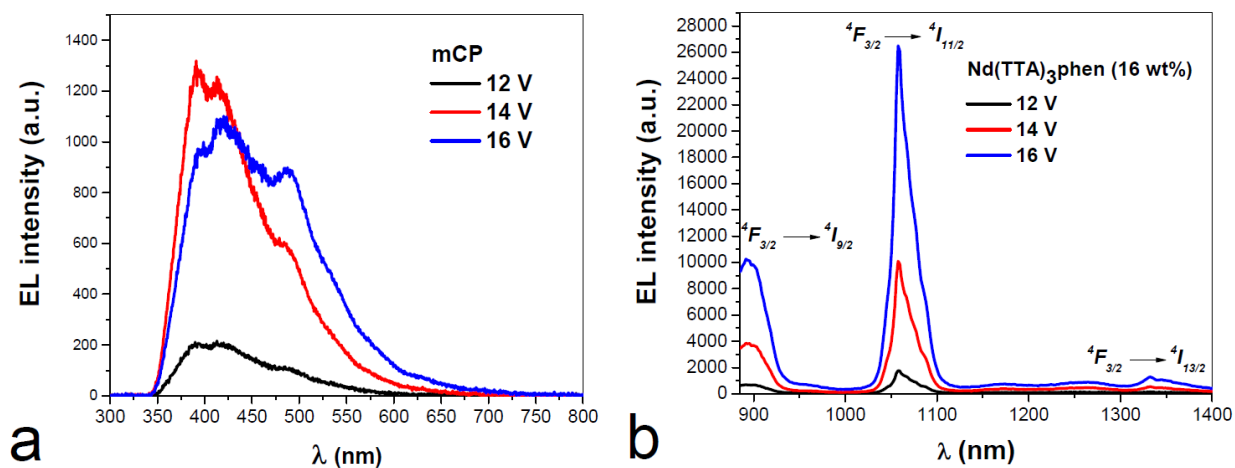


Figure 2.8: EL spectra of mCP (in the visible region) and Nd(TTA)₃Phen (16 wt.%) (in the NIR region) at different driving voltages in device B.

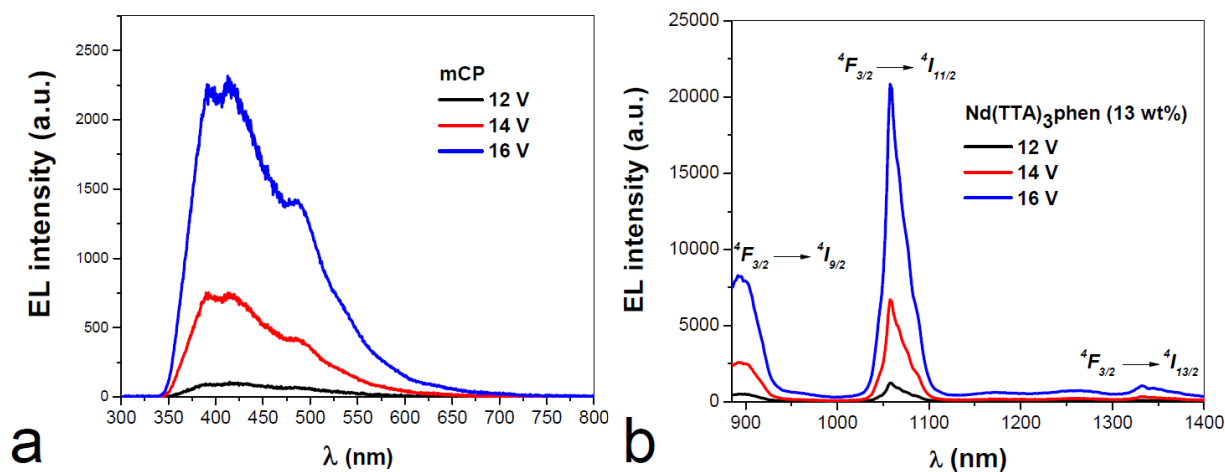


Figure 2.9: EL spectra of mCP (in the visible region) and Nd(TTA)₃Phen (16 wt.%) (in the NIR region) at different driving voltages in device C.

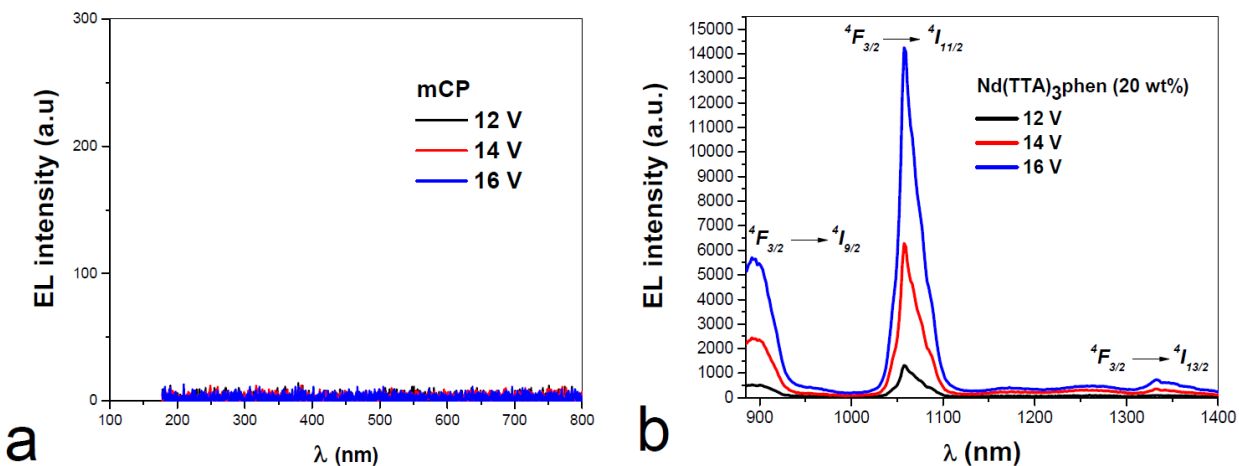


Figure 2.10: EL spectra of mCP (in the visible region) and Nd(TTA)₃Phen (20 wt.%) (in the NIR region) at different driving voltages in device D.

The NIR emission from Nd(TTA)₃Phen for all the devices was very stable under electrical excitation but the blue emission from mCP was very unstable even under low and moderate driving voltages, making recording the EL spectra of mCP difficult. For example, this can be seen for the decreased mCP EL emission at the driving voltage of 16 V in **Fig. 2.9(a)**. Since the devices were carefully encapsulated before device characterization, the emission instability of the host is presumably due to intrinsic chemical degradation mechanisms [298]. Such an effect would adversely affect the host rather than the Nd³⁺-complex because the Nd³⁺ ions are protected from their surrounding environment by the ligands.

2.2.5 Electrical and Efficiency Characterizations of the NIR OLEDs

The current density-voltage (J-V) plots of device A, B, C and D are displayed in **Fig. 11(a)**. Devices A, B, and C started emitting light at about 9 V but the threshold voltage increased up to 12.6 V in device D. These threshold voltages are lower than the ones reported in the literature for Nd³⁺-based OLEDs, which are in the range of 12 to 30 V [279-282, 284]. The results in **Fig. 11(a)**

show a slight shift of the J-V curves with an increase of the doping concentration from 7 to 20 wt.%, confirming that direct charge trapping on the emitter molecules [299] is indeed a mechanism that could take place in the devices in addition to the energy transfer from the host to the guest molecules. Notably, device A shows the highest current densities while device B shows the worst J-V characteristics. A possible scenario to explain the observed behavior is the following: In device A, charge carriers are mainly transported by the mCP host and there is no significant charge trapping by the guest molecules. In that blend, energy transfer from the host to the guest molecules is presumably the dominant mechanism for exciton formation on the guest molecules. In device B, charge carriers are partly trapped by the guest molecules while dopant molecules in devices C and D may form a channel for carrier transport.

The EQE was measured as a function of the current density in devices A, B, C and D. Because the EL spectra of device A, B and C are composed of both the blue emission from the mCP host and NIR emission from the Nd³⁺-complex, only the data obtained for device D is plotted in **Fig. 11(b)**. As shown above, the EL in device D is indeed only composed of the NIR emission. The result shows that device D exhibits a maximum EQE value of 0.022 % at 14.7 V and for a current density of 50 mA/cm². Even though the maximum EQE values measured in device A, B and C are 0.016 %, 0.020 % and 0.021 %, respectively, they contain certain amount of host emission but device D shows the highest efficiency from Nd³⁺, containing no emission from the host. The EQE measurement uncertainty for several devices was estimated to be ± 0.002%. The maximum EQE value of device D is significantly higher than the best values reported for solution-processed Nd³⁺-based polymer OLEDs (0.001 and 0.007 %) [280,281] and is comparable with the best values reported for thermally-evaporated devices (0.01 and 0.02 %) [291]. In particular, if we compare our results with those previously obtained using poly(N-vinylcarbazole) (PVK) as host [280,281],

the device performance achieved in the present work can be explained by the use of TPBi for the electron transport layer and the better charge transport properties of the mCP host.

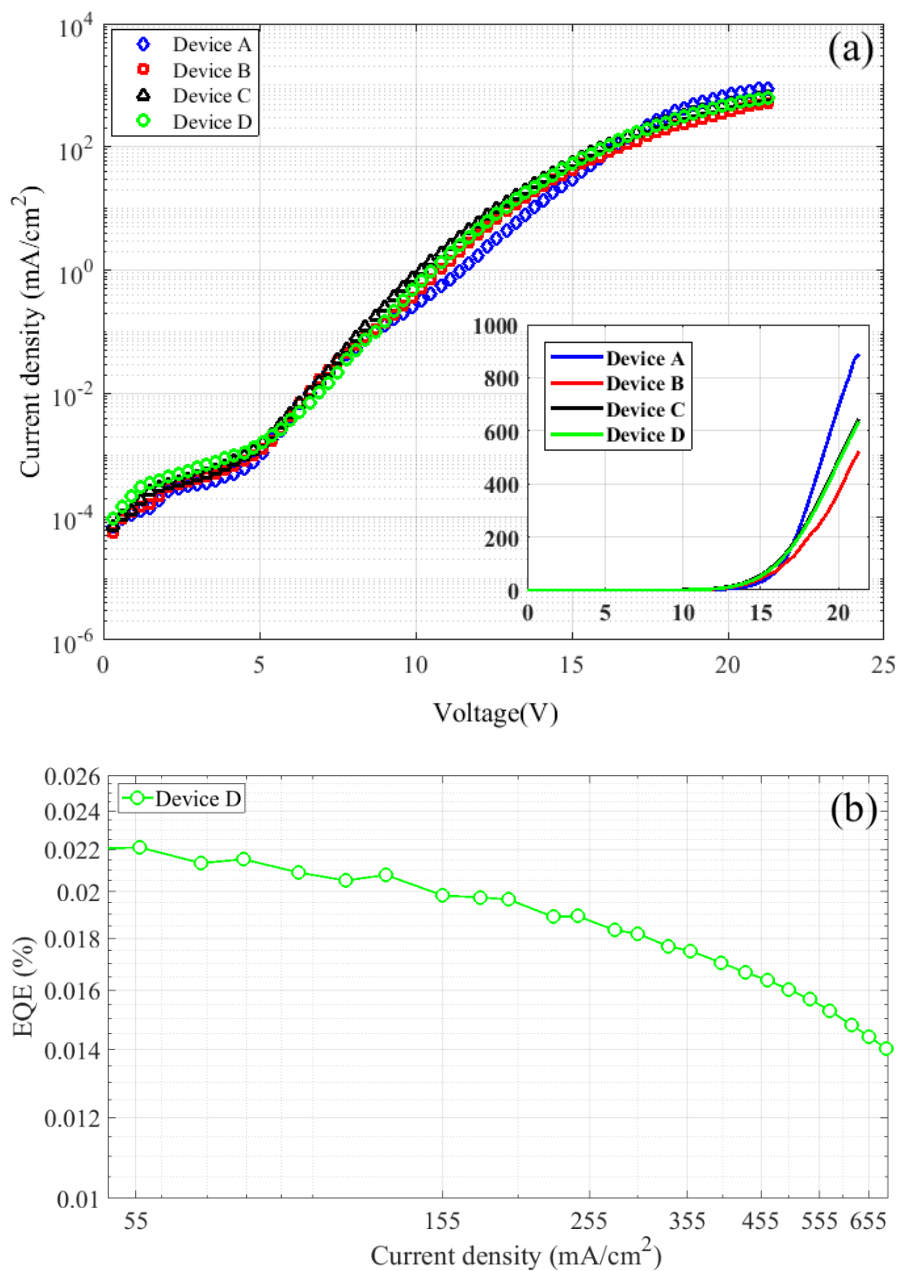


Figure 2.11: (a) Current density vs. voltage and (b) EQE vs. current density plots.

The electron and hole mobility values of mCP have been reported to be 3.4×10^{-5} and 1.2×10^{-4} cm²/Vs, respectively [300] but the hole mobility in PVK is 1×10^{-6} cm²/Vs [301]. Although mCP appears as a more appropriate host material than PVK for Nd(TTA)₃Phen-based OLEDs, the

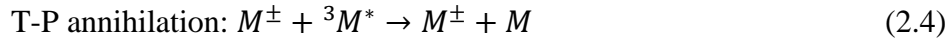
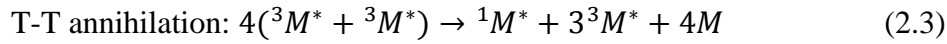
higher EQE value achieved in this work is still lower than the theoretical maximum EQE value of 0.1%, suggesting that an optimization of the device architecture should be possible to improve the charge balance and the overall performance of the Nd(TTA)₃Phen-based devices.

2.3 Efficiency Roll-Off Analysis

As **Fig. 11(b)** shows, device D exhibits a low efficiency roll-off under high current densities. For instance, while the maximum EQE is 0.022% at 50 mA/cm², the EQE drops to 0.014% at 700 mA/cm² i.e. over a current density range of 650 mA/cm², which is still higher than half of the maximum efficiency (i.e. 0.011%). Based on previous studies, efficiency roll-off in lanthanide-based OLEDs is attributed mostly to T-T annihilation [302-304]. As described in Chapter 1, this process can occur between host molecules, between guest molecules, and between host and guest molecules. Adachi et al. stated that the T-T annihilation between the TTA ligands and CBP host in the CBP:Eu(TTA)₃Phen system strongly lowered the efficiency of their devices even under very low current densities [304]. This was mainly due to the low triplet energy difference between CBP and TTA ligands (i.e. 0.13 eV), resulting in a strong energy-back transfer from TTA to CBP. Such a severe efficiency roll-off with CBP host and some other host materials with low triplet energy levels can also be found for lanthanide-based OLEDs in the literature [305-309]. They also showed that the T-T annihilation between two TTA ligands on identical Eu(TTA)₃Phen molecules (after triplet migration from CBP to TTA) is least likely possible due to the low concentration of Eu(TTA)₃Phen (2 wt.%) in their system. In the present study, however, this latter mechanism can presumably occur to some extent because of the much higher concentration of the Nd³⁺-complex (20 wt.%). It is also not possible to fully exclude at the current stage the third T-T annihilation process, which is related to triplet exciton migration between mCP

host molecules. In that context, we attribute the low efficiency roll-off observed in device D at high current densities to a significant reduction of the host-guest T-T annihilation process. As mentioned earlier, the energy differences between the triplet level of mCP and those of TTA and Phen ligands are 0.55 eV and 1 eV, respectively. This implies a reduced energy-back transfer from the ligands to mCP due to the relatively large triplet-triplet energy difference, lowering the probability for the host-guest T-T annihilation process in this system.

To corroborate that the T-T annihilation has little effect on the efficiency roll-off of device D, we apply the T-T and T-P models developed by Adachi et al. [45,304] to our experimental data. These models are described as follows:



where ${}^3M^*$ represents the triplet excited state, ${}^1M^*$ represents the singlet excited state, and M represents the ground state. As discussed earlier, in a host-guest system, T-T and T-P annihilation mechanisms can occur between the guest molecules (guest-guest annihilations), host molecules (host-host annihilations), or between the molecules of the host and guest (host-guest annihilations).

Hence, M represents a host or a guest molecule. The concentration of the triplet states in the T-T and T-P models are also given by:

$$\text{T-T annihilation: } \frac{d[{}^3M^*]}{dt} = -\frac{[{}^3M^*]}{\tau} - \frac{k_{TT}}{2} [{}^3M^*]^2 + \frac{J}{qd} \quad (2.5)$$

$$\text{T-P annihilation: } \frac{d[{}^3M^*]}{dt} = -\frac{[{}^3M^*]}{\tau} - k_{TP} [{}^3M^*]n_t + \frac{J}{qd} \quad (2.6)$$

In these equations, τ is the lifetime of the triplet state, J is the current density, q is the charge density, n_t is the density of trapped charges, and k_{TT} and k_{TP} are the T-T and T-P annihilation

rates. The current dependency of the EQE in the presence of T-T and T-P annihilation mechanisms can be calculated from the steady-state solutions of Eqn. 5 and Eqn. 6, given by:

$$\eta_{TT} = \eta_0 \frac{J_0}{4J} \left[\sqrt{1 + 8 \frac{J}{J_0}} - 1 \right] \quad (2.7)$$

$$\eta_{TP} = \eta_0 \frac{1}{1 + \left(\frac{J}{J_e}\right)^{1/(m+1)}} \quad (2.8)$$

Here, η_{TT} (η_{TP}) and η_0 are respectively the EQE in the presence and absence of the T-T (T-P) annihilation, J is the current density, $J_0 = \frac{4qd}{\tau^2 k_{TT}}$ and $J_e = \left(\frac{1}{\tau k_{TP}}\right)^{m+1}$. We fit Eqn. 7 and Eqn. 8 to the normalized ($\eta_0 = 1$) experimental EQE data. Here, J_0 , J_e , and m are the fitting parameters. As **Fig. 2.12** displays, the T-T model does not fit the experimental data, confirming our initial analysis that, unlike previous studies, the T-T annihilation does not play a significant role in the roll-off. Moreover, despite the reduced T-T annihilation and low roll-off in device D, **Fig. 2.12** shows that the T-P annihilation still decreases the EQE. In the following chapters, since the host materials used in the devices have high triplet energy, we will see that the T-P annihilation is primarily responsible for the efficiency roll-off in our solution-processed lanthanide-based OLEDs. For this reason, the roll-off analyses will be done based on the T-P process.

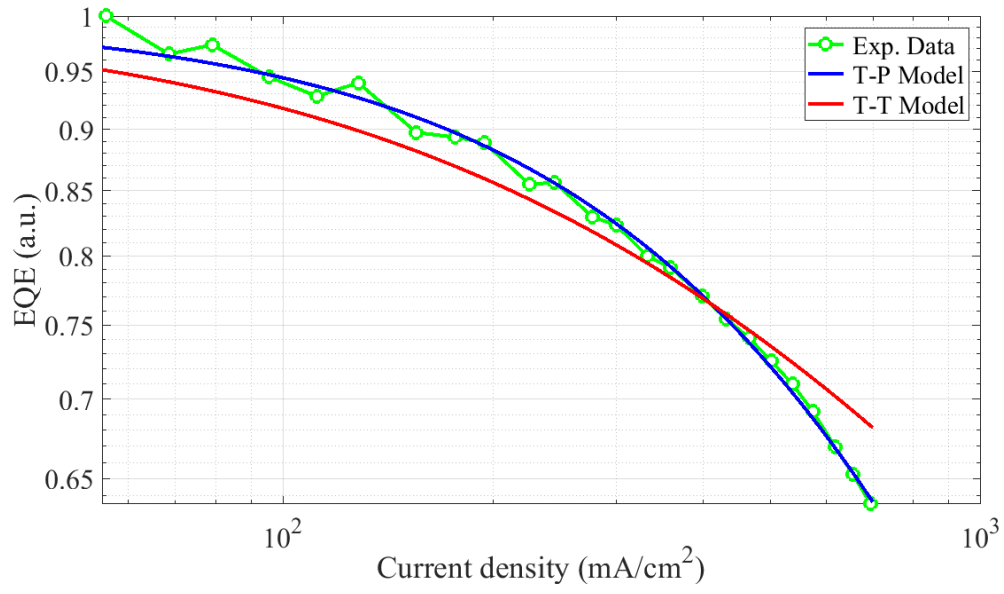


Figure 2.12: T-P (blue) and T-T (red) models fitted to the normalized ($\eta_0 = 1$) experimental EQE data. $J_0 = 109.5 \text{ mA/cm}^2$, $J_e = 1130 \text{ mA/cm}^2$, $m = 0.14$.

Chapter 3: Achieving very Low Efficiency Roll-Off in Lanthanide-based OLEDs with a Solution-Processed Exciplex Host

In this chapter, we report an enhanced NIR EQE from Nd(TTA)₃Phen and investigate that how using a binary host system can lead to a low efficiency roll-off in lanthanide-based devices. The NIR-emitting complex is blended into an *exciplex-forming* co-host system comprising 2,7-bis(diphenylphosphoryl)-9,9'-spirobifluorene (SPPO13) as the electron transporting material and 4,4',4''-tris(carbazol-9-yl)triphenylamine (TCTA) as the hole transporting material, in solution-processed small molecule OLEDs. This binary ambipolar host system favors direct charge trapping and exciton formation on the Nd³⁺-complex molecules. Efficient energy transfer from the singlet and triplet exciplexes formed between the host molecules to the Nd³⁺ ions contributes to the enhanced luminescence efficiency. The PLQY of this blend is 1.2%, and the optimized OLED shows a maximum EQE of 0.034%. Notably, the device exhibits a low efficiency roll-off of only 12% over a current density range of 100 mA/cm², due to the reduced T-P annihilation.

3.1 Experimental Details

The device structure of the fabricated NIR OLED is as follows: ITO/PEDOT:PSS (35 nm)/EML (20 nm)/TPBi (40 nm)/LiF (0.8 nm)/Al (100 nm), where the composition of the EML is SPPO13:TCTA:Nd(TTA)₃Phen (6:3:1 weight ratio). The chemical structures of the materials used in the device are shown in **Fig. 3.1**. Except for the EML, details of the fabrication process and device characterizations are similar to those in Chapter 2. For the fabrication of the EML, a blend of SPPO13:TCTA:Nd(TTA)₃Phen (6:3:1 weight ratio) was prepared at a concentration of 10 mg/ml in chlorobenzene and then spin-coated onto the PEDOT:PSS layer. After that, the samples were baked at 100 °C for 30 min to remove any remaining solvent. SPPO13 and TCTA

are employed for their high charge carrier mobility and solubility in common organic solvents, which enable the fabrication of high-quality films [310-312].

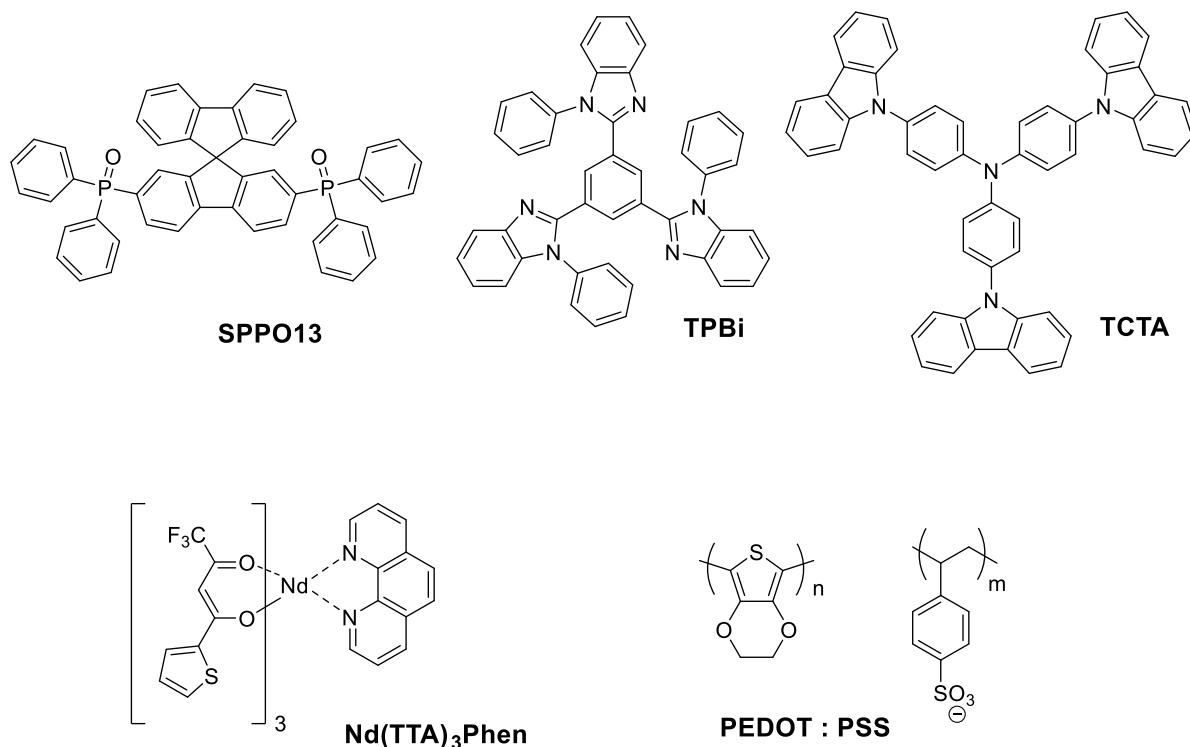
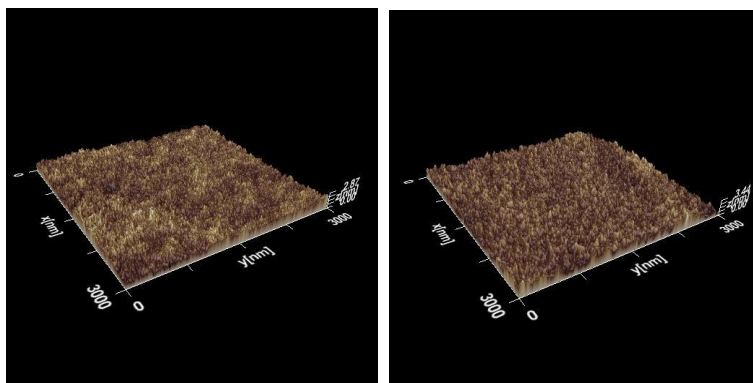


Figure 3.1: Chemical structures of the materials used in the device structure.

3.2 Results and Discussion

3.2.1 Characterization of the Blend Surface Morphology by AFM

AFM images of SPPO13:TCTA and SPPO13:TCTA:Nd(TTA)₃Phen films prepared by spin-coating on quartz substrates are shown in **Fig. 3.2**. These images show very smooth surface morphologies for the doped and undoped solution-processed films, with low root-mean-square (RMS) roughness values (≤ 0.4 nm). This suggests that no recrystallization or host-guest phase segregation occurs during the thermal annealing of the spin-coated films.



(a)

(b)

Figure 3.2: AFM images of the spin-coated (a) SPPO13:TCTA (6:3) and (b) SPPO13:TCTA: Nd(TTA)₃Phen (6:3:1) blend films. The RMS roughness values for (a) and (b) are 0.33 nm and 0.40 nm, respectively.

3.2.2 Electroluminescence Spectrum of the NIR OLED and PL Spectra of the Materials

The EL spectrum of the device is displayed in **Fig. 3.3**. The EL spectrum contains only the three characteristic NIR emission peaks from Nd³⁺ at 890 nm (${}^4F_{3/2} \rightarrow {}^4I_{9/2}$), 1060 nm (${}^4F_{3/2} \rightarrow {}^4I_{11/2}$), and 1330 nm (${}^4F_{3/2} \rightarrow {}^4I_{13/2}$). We did not observe any visible emission, implying that the NIR OLED does not exhibit any emission in the visible region.

Steady-state PL spectra of SPPO13, TCTA, SPPO13:TCTA, and SPPO13:TCTA: Nd(TTA)₃Phen blend systems are shown in **Fig. 3.4**. The PL spectra of SPPO13 and TCTA significantly overlap with the absorption spectrum of the TTA ligands in Nd(TTA)₃Phen. This suggests that the singlet excited state energies of the host materials can be efficiently transferred to the complex via Förster-type energy transfer process. The efficient Dexter-type energy transfer from the triplet excited-states of the host materials to those of the Phen and TTA ligands is also expected to occur. However, the PL spectrum of the SPPO13:TCTA blend is completely different from those of individual SPPO13 and TCTA. The SPPO13:TCTA blend, which has been previously found to be

an *exciplex-forming* electron donor-acceptor system [313,314], exhibits a broad red-shifted emission peak centered at 479 nm. The PL spectrum of the SPPO13:TCTA:Nd(TTA)₃Phen blend shows a maximum at 467 nm. We attribute this small 12-nm blue-shift to perturbation of the exciplex interaction between TCTA and SPPO13 by Nd(TTA)₃Phen. The energy gap between the LUMO of SPPO13 and the HOMO of Nd(TTA)₃Phen is smaller than the HOMO–LUMO gap of SPPO13 and Nd(TTA)₃Phen (see **Fig. 3.5**). As stated in Chapter 1, this is an important requirement for exciplex formation. Despite this, we did not observe any exciplex emission from the (donor-acceptor) SPPO13:Nd(TTA)₃Phen blend. This may be because the molecular structure of the Nd³⁺-complex is spherical, thus hindering exciplex formation in the SPPO13:Nd(TTA)₃Phen system.

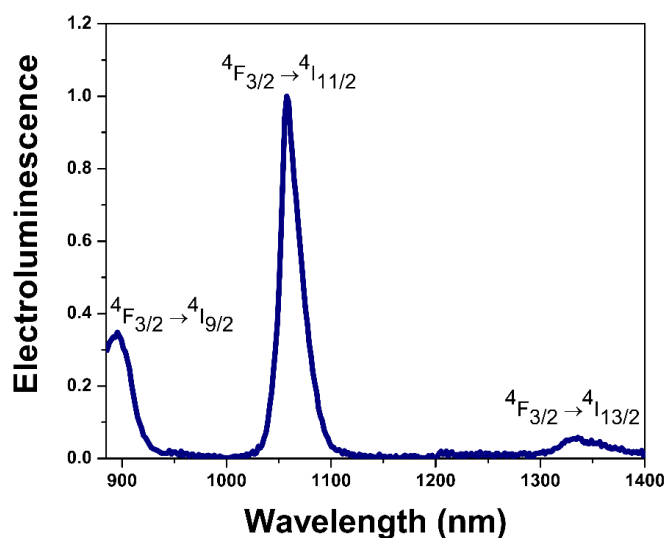


Figure 3.3: Normalized NIR EL spectrum of the device recorded at 15 V.

Consequently, because no signature of the PL spectra of the individual SPPO13 and TCTA is seen in the PL spectrum of the SPPO13:TCTA blend, they cannot contribute to the excitation process of Nd(TTA)₃Phen in the SPPO13:TCTA:Nd(TTA)₃Phen blend system. For this reason, we expect that only SPPO13:TCTA singlet and triplet exciplexes contribute to the sensitization of the Nd³⁺

ion in the complex. We previously stated that in such a case, the singlet and triplet exciplex energy levels are very close to each other. **Figure 3.6** shows that the singlet and triplet exciplex energies can be transferred to the triplet energy levels of the ligands and subsequently to the Nd^{3+} ion via *antenna effect*. Direct energy transfer from the singlet and triplet exciplexes to the Nd^{3+} ions can also occur. The SPPO13:TCTA exciplexes are also expected to form under electrical excitation in the device, contributing to the sensitization of the Nd^{3+} ions. We did not detect any visible EL emission from the individual host materials or the SPPO13:TCTA exciplexes. This indicates that energy transfer from the exciplexes to the NIR-emitting complex is efficient, and that direct formation of excitons on the $\text{Nd}(\text{TTA})_3\text{Phen}$ molecules occurs efficiently in the device. The latter process can be understood when considering the energy level alignments between the ETL and HTL and EML in the device structure, as shown in **Fig. 3.5**.

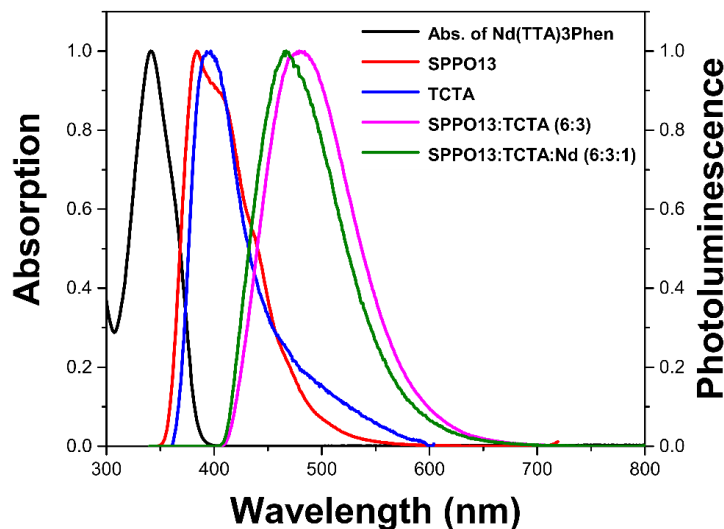


Figure 3.4: Normalized absorption spectrum of $\text{Nd}(\text{TTA})_3\text{Phen}$ recorded from dichloromethane solution, and steady-state PL spectra of SPPO13, TCTA, SPPO13:TCTA (6:3 weight ratio), and SPPO13:TCTA: $\text{Nd}(\text{TTA})_3\text{Phen}$ (6:3:1 weight ratio).

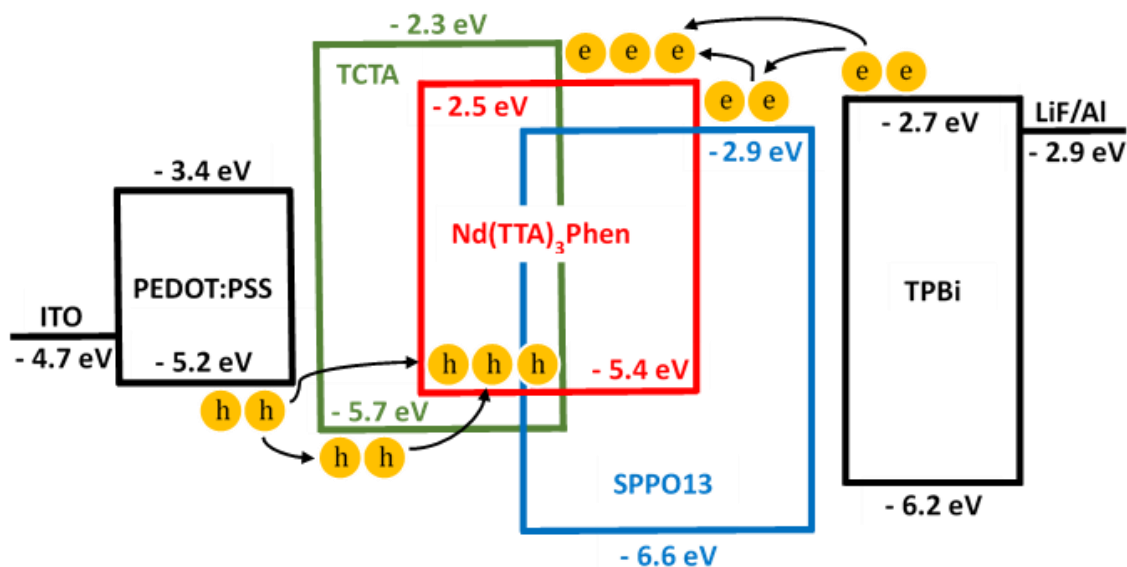


Figure 3.5: Energy level alignments of the materials in the device structure. Charge transport pathways and the excitation of $\text{Nd}(\text{TTA})_3\text{Phen}$ through the ETL and HTL and direct charge trapping process by the NIR complex are also shown.

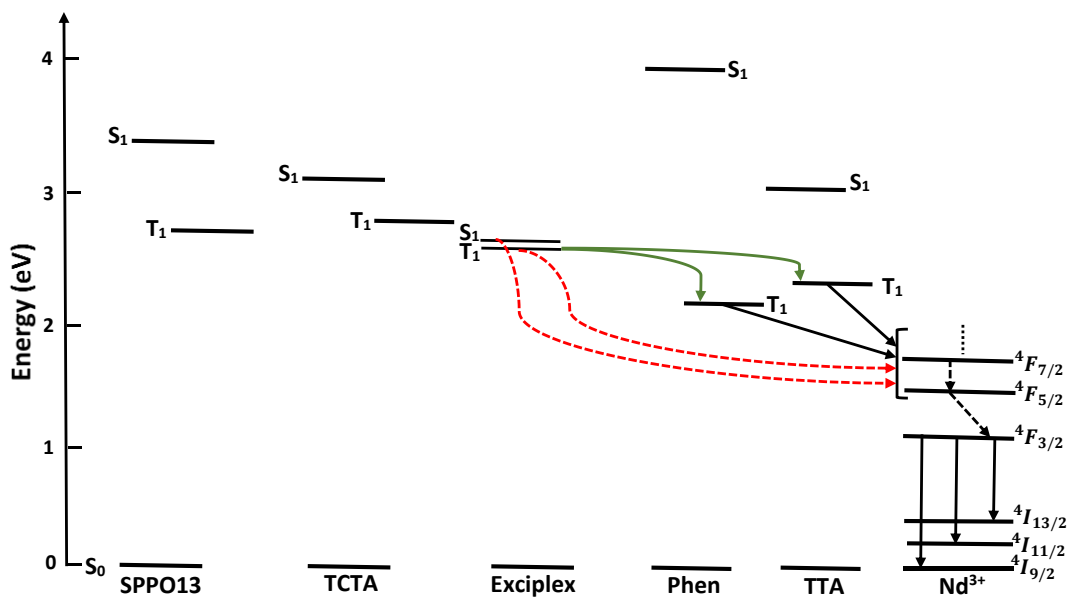


Figure 3.6: Energy diagram of the molecular system. The first excited singlet (S_1) and triplet (T_1) state energy levels of SPPO13, TCTA, $\text{Nd}(\text{TTA})_3\text{Phen}$, and SPPO13:TCTA exciplexes are indicated. Forbidden $4f-4f$ transitions in Nd^{3+} are shown with black dashed arrows. The direct sensitization pathways of Nd^{3+} through the singlet and triplet exciplex energy levels (dashed red), and sensitization through the ligands (solid green) are also shown.

3.2.3 Transient Photoluminescence Measurements

To elucidate the formation of exciplexes and to better understand the sensitization mechanism of the Nd^{3+} ion in the complex, we performed transient PL measurements in the visible spectral region for SPPO13, TCTA, SPPO13:TCTA, and SPPO13:TCTA: $\text{Nd}(\text{TTA})_3\text{Phen}$. The measurements were carried out using time-correlated single-photon counting (TCSPC) technique, and time-resolved fluorescence plots are shown in **Fig. 3.7**. A pulsed diode laser with a wavelength of 405 nm and pulse width of ~ 45 ps was used to optically excite the films of SPPO13, TCTA, SPPO13:TCTA, and SPPO13: $\text{Nd}(\text{TTA})_3\text{Phen}$. A bandpass filter (450–760 nm) was used to measure the exciplex fluorescence from the blend samples, while blocking out the NIR emission from Nd^{3+} . All photons from the exciplex emission within the 450–760 nm spectral range were counted during the measurements. The full width at half maximum of the instrument response function (IRF) was measured to be ~ 250 ps. The TCSPC profile of SPPO13 shows three exponential components with decay times of 0.3 ns, 1 ns, and 3.5 ns. We attribute these lifetimes to the emission from SPPO13 molecules that are subject to different environments in the neat film. Similarly, the TCSPC profile of TCTA exhibits exponential components with decay times of 0.4 ns, 2.6 ns, and 10.3 ns, which we similarly attribute to emission from the dye subjected to different environments in the neat film. The two very short lifetime components (0.3 ns and 0.4 ns) are approaching the IRF limit, and thus these components could potentially be faster than the stated values. In the SPPO13:TCTA system, prompt (short) and delayed (long) exciplex fluorescence decays are observed with lifetimes of 53 ns and 297 ns, respectively. These emission lifetimes are much longer than those of SPPO13 and TCTA. In the SPPO13:TCTA: $\text{Nd}(\text{TTA})_3\text{Phen}$ system, the short and long decay exciplex fluorescence lifetimes are 7.7 ns and 88.4 ns, respectively, which are noticeably shorter than those in the SPPO13:TCTA system. This is indeed consistent with the

SPPO13:TCTA exciplex energies being effectively transferred to the Nd^{3+} ions in the SPPO13:TCTA: $\text{Nd}(\text{TTA})_3\text{Phen}$ blend. A NIR PLQY as high as 1.2% is measured in the SPPO13:TCTA: $\text{Nd}(\text{TTA})_3\text{Phen}$ system. This PLQY is higher than the reported values (0.4% and 0.5%) using the same complex dispersed in the mCP host presented in Chapter 1. The higher PLQY obtained in this chapter is attributed to the more efficient sensitization of the Nd^{3+} ions by the singlet and triplet exciplexes.

The efficient energy transfer from the exciplexes to the complex is well supported by the PL spectra of SPPO13:TCTA and SPPO13:TCTA: $\text{Nd}(\text{TTA})_3\text{Phen}$, which are displayed in **Fig. 3.8**. These spectra provide clear evidence for the exciplex emission quenching due to the energy transfer to $\text{Nd}(\text{TTA})_3\text{Phen}$.

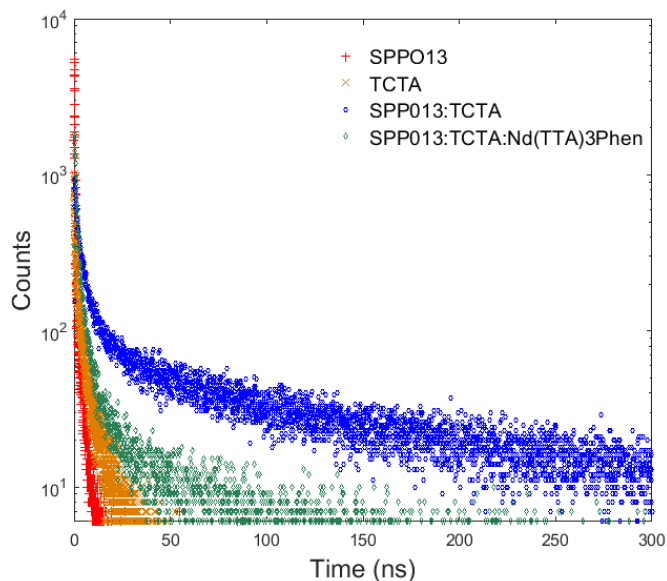


Figure 3.7: Transient PL measurements of the host materials and blend systems.

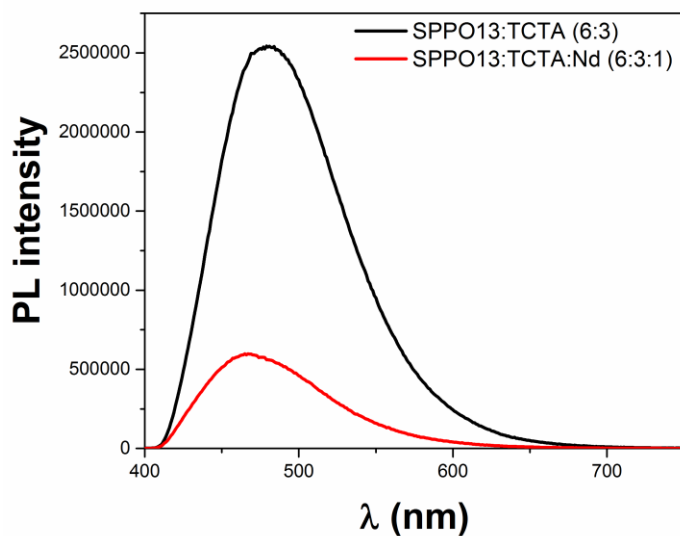


Figure 3.8: Steady-state PL spectra of SPPO13:TCTA and SPPO13:TCTA:Nd(TTA)₃Phen thin films. The excitation wavelength is 350 nm.

3.2.4 Electrical and Efficiency Characterizations of the NIR OLED

Current density vs. voltage and EQE vs. current density plots of the device are shown in **Fig. 3.9**. The device starts emitting NIR light at about 11 V. This turn-on voltage is very close to the values presented in the previous chapter and is lower than the other reported values for Nd³⁺-based OLEDs, which range from 12 to 30 V [279-284]. A maximum EQE as high as 0.034 ± 0.002% is obtained at 130 mA/cm², which is 50% higher than the the EQE with the mCP host. Except for the thermally-processed Nd³⁺-based OLEDs reported by Chen et al. [291], the EQE in the present chapter is higher than any other reported EQE for solution-processed or thermally-processed NIR OLEDs based on Nd³⁺-complexes [279-284,315-317]. This EQE is also comparable to or higher than the EQE values recently reported for NIR OLEDs with EL in the telecommunication wavelength range (900–1600 nm), which were fabricated from TADF materials (0.037%) [318] or carbon nanotube emitters (0.014%) [319]. As discussed in Chapter 1, the low efficiency and relatively high working voltages in lanthanide-based NIR OLEDs are

mainly caused by the low electroactivity of lanthanide complexes and coupling of the NIR emission to the highly vibrating C-H and O-H bonds present in the ligands and organic materials used in the device structures. Additionally, in the case of the device reported in the present chapter, considering the rather large difference in the HOMO levels, the observation of the EL onset at about 11 V is presumably due to the strong charge carrier trapping by the Nd^{3+} -complex in the SPPO13:TCTA host.

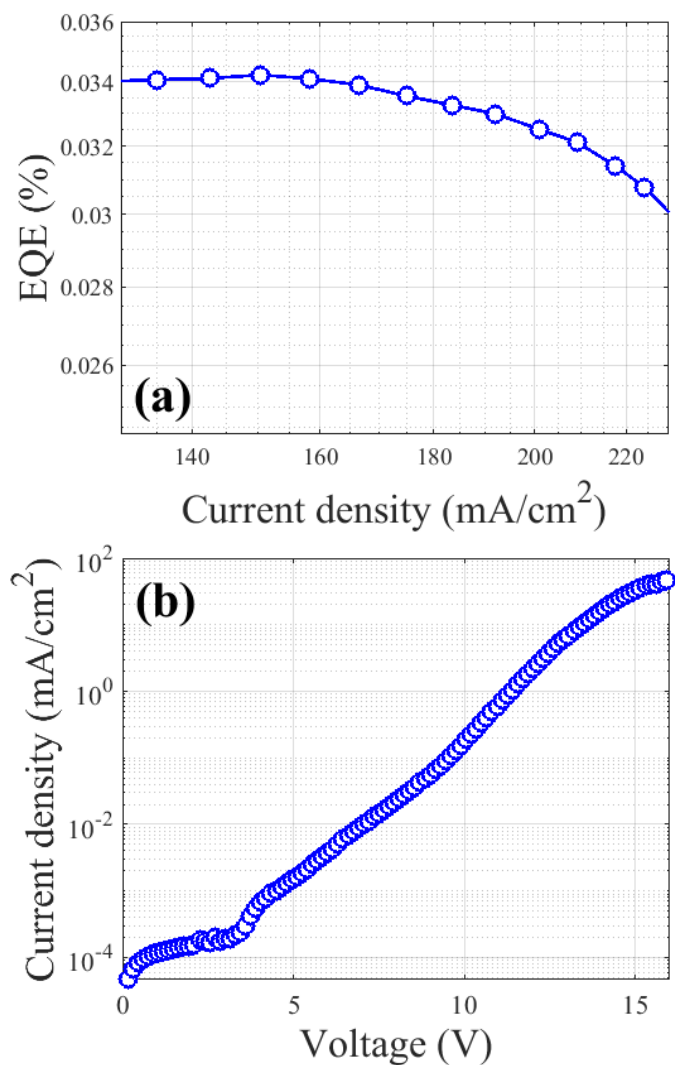


Figure 3.9: (a) EQE vs. current density and (b) current density vs. voltage plots.

3.3 Efficiency Roll-Off Analysis

Importantly, the EQE decreases from 0.034% at 130 mA/cm² to 0.030% at 230 mA/cm². This indicates that the device exhibits a very low efficiency roll-off of only 12% over a current density range of 100 mA/cm². As mentioned in the previous chapters, lanthanide-based OLEDs suffer from T-T and T-P annihilation processes [302-309].

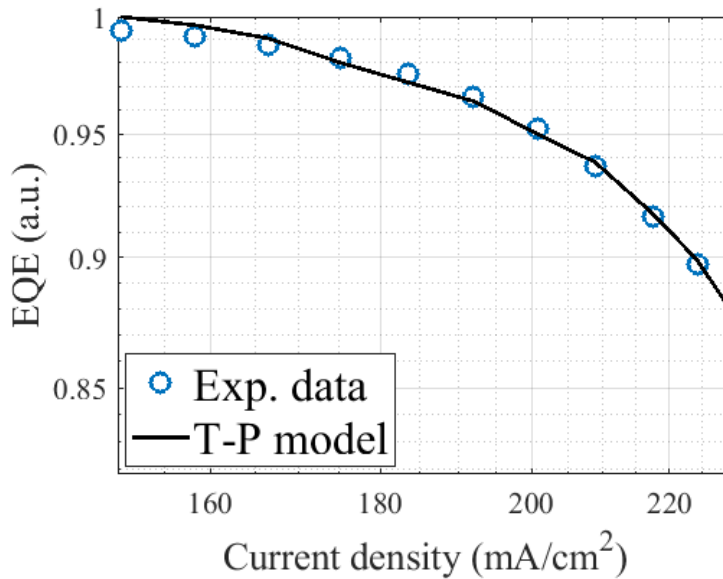


Figure 3.10: Normalized EQE vs. current density plot fitted to the T-P model ($J_e = 299.5$ mA/cm², $m = 0.8$).

To elucidate the role of T-T and T-P annihilation mechanisms, we fit Eqn. 2.7 and Eqn. 2.8 to the normalized experimental EQE data. As **Fig. 3.10** shows, we obtain a good agreement between the experimental data and the T-P model. However, the T-T model does not fit for any reasonable value of J_0 (plot not shown). This indicates that the T-P model is primarily responsible for the EQE roll-off in the device. We previously pointed out that in an OLED with a single host, electron and hole polarons are accumulated at the HTL/EML and ETL/EML interfaces because of the large energy barriers between the organic layers. As a result, accumulation of charge polarons at the interfaces limits the emission (exciton recombination) zone to very narrow regions close to the

interfaces, which subsequently causes severe efficiency roll-off due to quenching of the radiative excitons by polarons. Such an effect is particularly observed under large current densities. However, since exciplex emission is a barrier-free process occurring at the donor/acceptor interface and that exciplex energy can be transferred to the emitter in a host-guest system, the emission zone is extended to the entire EML, reducing the T-P annihilation. Further, balanced charge transport provided by the mixed host in an *exciplex-forming* system extends the emission zone in the EML as well [320-322]. In this context, we attribute the low efficiency roll-off to a reduction of quenching by the T-P annihilation. This is due to the small energy barriers at the HTL/EML and ETL/EML interfaces, as well as the extension of emission zone to the entire EML by balanced charge transport provided by the SPPO13:TCTA co-host system, and barrier-free energy transfer from the exciplexes to the NIR emitter.

Chapter 4: Reducing the Triplet-Polaron Annihilation Mechanism in lanthanide-based OLEDs under External Magnetic Fields

In the previous chapters, we stated that T-P annihilation mechanism is the most detrimental exciton quenching process that decreases the efficiency of OLEDs at high current densities, causing a severe efficiency roll-off in these devices. This mechanism is also the most critical obstacle towards the realization of electrically pumped organic semiconductor lasers, which require very high current densities to reach threshold. In this chapter, under a relatively large applied magnetic field of $B = 235$ mT, we demonstrate efficient suppression of the efficiency roll-off at high current densities in solution-processed OLEDs based on red-emitting $\text{Eu}(\text{DBM})_3\text{Phen}$ (DBM: 1,3-diphenylpropane-1,3-dione and Phen: 1,10-phenanthroline) complex doped into a co-host system. We achieve this by reducing the Förster-type host-host T-P annihilation, without and with the influence of magnetite (Fe_3O_4) nanoparticles. Under the applied magnetic field, we show that manipulation of polaron-spins and radiative exciton dynamics lead to quantitative roll-off suppression.

4.1 Experimental Details and Materials

The structure of the devices and fabrication details is as follows: ITO/PEDOT:PSS (30 nm)/PVK (15 nm)/SimCP2:PBD: $\text{Eu}(\text{DBM})_3\text{Phen}$ (30:70:5 wt.%) (64 nm)/BCP (10 nm)/Alq₃(40 nm)/LiF(0.8 nm)/Al (100 nm). First, a 30 nm thick layer of PEDOT:PSS (Clevios Al 4083, Heraeus), as the hole injection layer, was spin-coated onto the pre-cleaned ITO substrates and then baked at 140 °C for 20 min. Next, a 15 nm thick layer of the hole transporting/electron blocking Poly (n-vinyl carbazole) (PVK) with a high molecular weight (1,100,000 g/mol, Sigma Aldrich) was spin coated from a 7.5 mg/ml chlorobenzene solution and then baked at 150 °C for 15 min. The PVK layer prevents quenching of excitons on the PEDOT:PSS layer and ensures exciton

confinement into the EML. It should be mentioned that we did not deposit any PVK layer onto the PEDOT:PSS in the devices reported in the previous chapters because, like the other organic layers, it absorbs the NIR light, decreasing the maximum achievable EQE. After that, a 20 mg/ml solution of the co-host system consisting of Bis[3,5,-di(9H-carbazol-9-yl) phenyl]diphenylsilane (SimCP2, Lumtec. Corp.) (30 wt.%), 2-(4-biphenyl)-5-(4-tert-butylphenyl-1,3,4-oxadiazole) (PBD, Sigma Aldrich) (70 wt.%), and Eu(DBM)₃Phen complex (Lumtec. Corp.) (5 wt.%) was prepared in dichloromethane to fabricate the EMLs of the devices. This solution was further diluted either with pure dichloromethane (1:1 vol.%) or with the dichloromethane-dispersed Fe₃O₄ nanoparticles (15-20 nm, Nanomaterials Inc.) (0.1 mg/ml) to fabricate the EML of the undoped and NP-doped OLEDs, respectively. The solutions were spin coated onto the PVK layer. The average thickness of the EML was measured to be 64 nm using DEKTAK profilometer. Then, a 10 nm thick layer of the electron transporting/hole blocking 2,9-dimethyl-4,7-diphenyl-1,10-phenanthroline (BCP, Sigma Aldrich) and a 40 nm thick layer of the electron transporting tris(8-quinolinolato) aluminum(III) (Alq₃, Sigma Aldrich) were thermally deposited onto the EML. The fabrication process was completed by depositing a 0.8 nm of LiF and a 100 nm thick layer Al as the cathode. For the magnetic field effect measurements, a lightweight magnet (B = 235 mT) was directly placed on the devices. The area of the magnet was wide enough to provide a uniform magnetic field over the devices. For the efficiency measurements, the devices were placed directly on a silicon photodiode (HAMAMATSU Co.) connected to a SCS-4200 Keithley semiconductor analyzer and then the photocurrent of the photodiode was recorded by sweeping the bias voltage. Moreover, to eliminate any probable emission from the host or charge transporting materials, a 590 nm long-pass filter (THORLABS) was placed in between the photodiode and the device under test. The efficiency calculations were done using the procedure described in Chapter 1 (see section

1.3). The current-voltage characteristics of the devices were also recorded at the same time. The efficiency measurements were carried out without encapsulation in a nitrogen-filled glove-box. The PL of the materials and EL spectra of the devices were recorded by an Ocean Optics spectrometer in ambient condition. **Figure 4.1** shows the chemical structures of the materials used in the OLEDs.

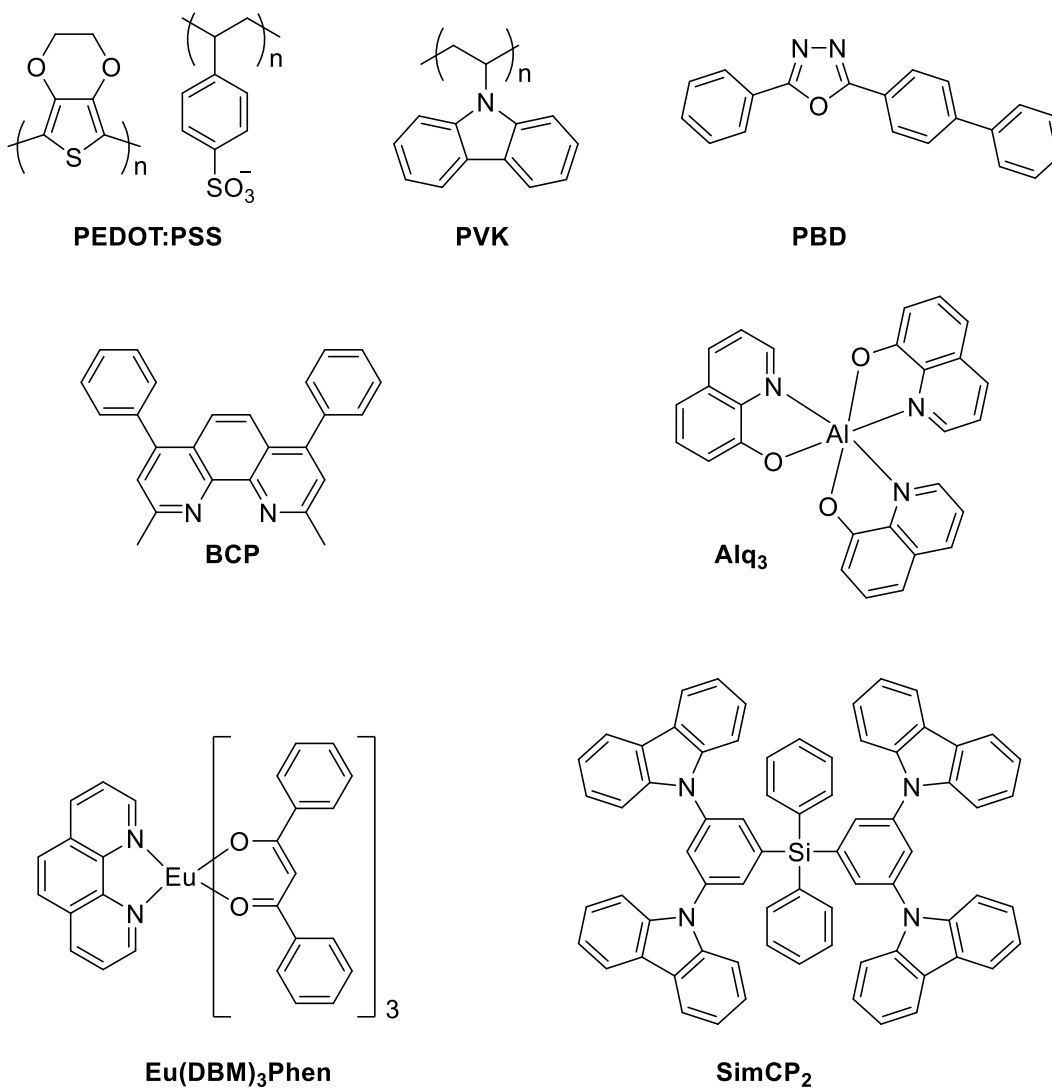


Figure 4.1: Chemical structures of the materials used in the devices.

4.2 Charge Transport Process in the Devices

As **Fig. 4.2** shows, charge transport process in the devices can proceed via two pathways: i) PBD and SimCP2 can capture electrons and holes injected from the corresponding electrodes, giving rise to exciton formation on the host molecules. Then charge carriers can be captured by the $\text{Eu}(\text{DBM})_3\text{Phen}$ molecules. ii) Electrons and holes can also be trapped directly by the $\text{Eu}(\text{DBM})_3\text{Phen}$ molecules, forming the excitons directly on the ligands. SimCP2 is a bipolar material that can transport electrons and holes with the same charge carrier mobility but PBD is an electron transporting material. Such a composition can enhance the charge balance efficiency of the devices. However, there is a large energy barrier for injecting electrons between BCP and host materials and between BCP and the lanthanide complex. Since this leads to an electron accumulation at the ETL/EML, we will see in the following that this issue causes a severe efficiency roll-off mainly due to the T-P annihilation.

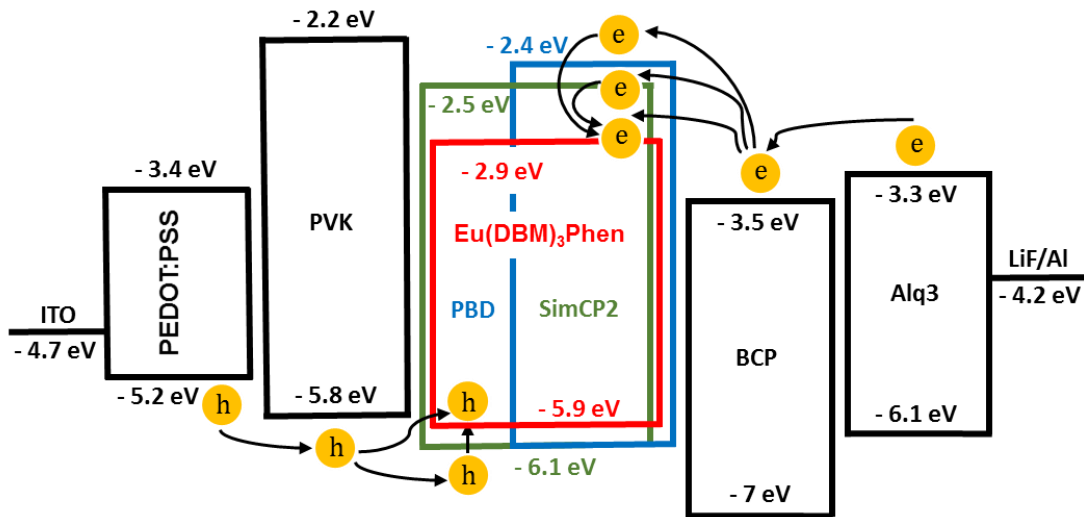


Figure 4.2: Energy level alignments of the materials used in the device structure. The charge transport pathways and the excitation of $\text{Eu}(\text{DBM})_3\text{Phen}$ through the ETL and HTL into the EML are also shown.

4.3 Sensitization Mechanism of the Eu^{3+} Ion in the Lanthanide Complex

As **Fig. 4.3 (a)** shows, Förster-type energy transfer from SimCP2 and PBD to $\text{Eu}(\text{DBM})_3\text{Phen}$ is very efficient because there is a significant overlap between the absorption spectrum of the DBM ligand and the PL spectra of SimCP2 and PBD. Further, in addition to the emission from the Eu^{3+} ions centered at 612 nm (${}^5D_0 \rightarrow {}^7F_2$ transition in Eu^{3+}), a small EL emission in the 470-550 nm spectral region is observed (see **Fig. 4.3 (b)**), which is likely due to the exciplexes formed at the interfaces between the host materials and charge transporting layers. Specifically, previous studies have shown that exciplex formation between PVK and PBD is highly probable [323]. No exciplex emission from the PL spectrum of the SimCP2:PBD blend is observed. The PL spectrum of the blend looks very similar to that of PBD because of the higher weight ratio of PBD in the SimCP2:PBD blend (30:70 wt.%). Consequently, the co-host system does not contribute to the above-mentioned EL in the 470-550 nm spectral region. This is because the excited singlet energy of the host materials is fully transferred to the Eu^{3+} -complex via Förster process. The singlet and triplet energies of the host materials and the ligands are summarized in Table 4.1. **Figure 4.4** also displays all the possible energy transfer pathways from the host materials to the complex. To eliminate the 470-550 nm emission, we employed a 590 nm long-pass filter when measuring the efficiency of the devices, so the measurements were carried out only for the emission from the Eu^{3+} ion.

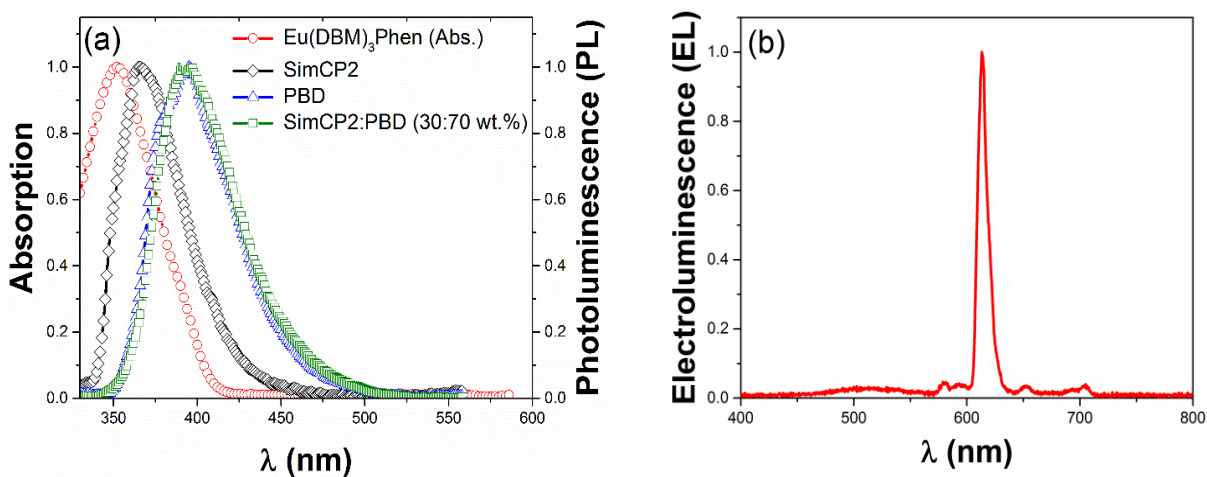


Figure. 4.3: (a) Normalized PL spectra of SimCP2, PBD, SimCP2:PBD blend, and the absorption spectrum of $\text{Eu}(\text{DBM})_3\text{Phen}$, and (b) EL spectrum recorded at 10 V.

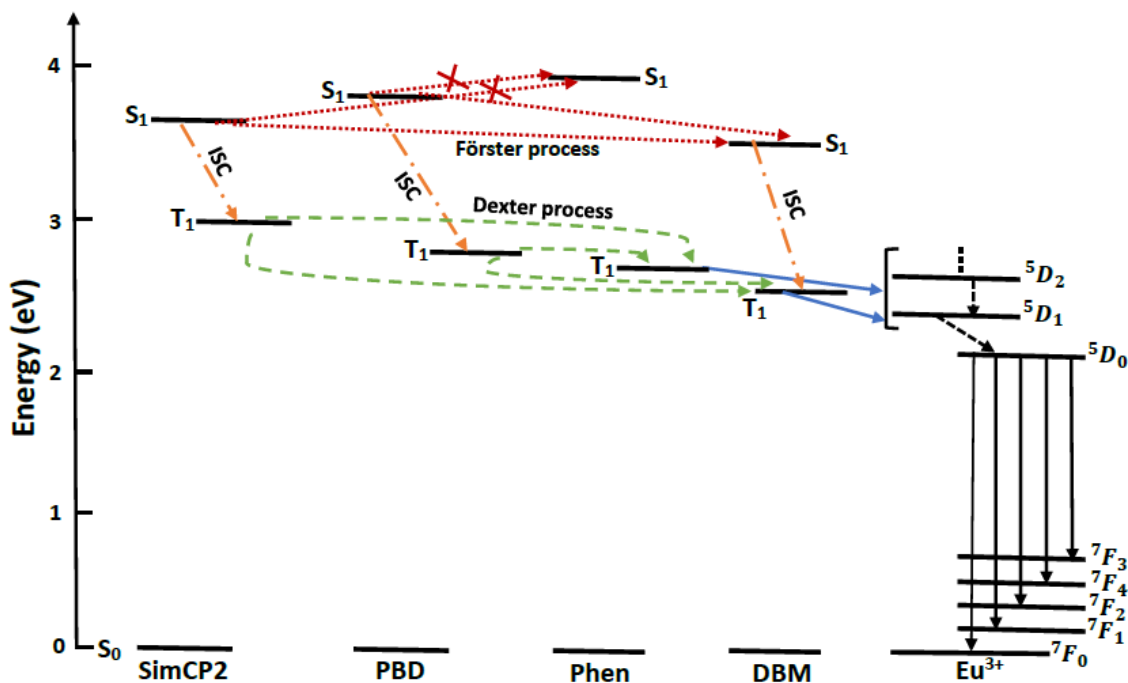


Figure. 4.4: Energy diagram of SimCP2 and PBD host materials, DBM and Phen ligands, and the transition energy levels of the Eu^{3+} ion. ISC represents intersystem crossing, shown with a yellow dashed-dotted line. Dexter-type triplet-triplet energy transfer between the triplet levels is shown with green dashed lines. Förster-type energy transfer between the singlet levels is shown with red dotted lines. The blue solid lines show the energy transfer from the triplet energy levels of DBM and Phen ligands to the Eu^{3+} ion.

Table 4.1: Summary of the singlet and triplet energies of SimCP2, PBD, DBM and Phen ligands.

Compound	E _{singlet} (eV)	E _{triplet} (eV)	References
SimCP2	3.60	3.01	[324]
PBD	3.70	2.67	[325]
DBM	3.51	2.53	[326]
Phen	3.87	2.66	[327,328]

4.4 Results and Discussion

4.4.1 Effects of the External Magnetic Field on the External Quantum Efficiency and Luminance of the Devices

The EQE vs. current density and luminance vs. voltage plots of the device containing no Fe₃O₄ nanoparticles (hereafter the undoped device) without and with the external magnetic field are shown in **Fig. 4.5**. Without any magnetic field, the undoped device exhibits a maximum EQE as high as 0.42% at 0.9 mA/cm² and 10.4 V. This EQE could be improved by optimizing the device structure because previous reports have demonstrated that Eu³⁺-based OLEDs can exhibit much higher EQE values by device engineering [25-28]. Under the magnetic field, the maximum EQE drops to 0.32% at 5.8 mA/cm² and 12 V. The slight decrease in the EQE under the magnetic field may be related to a reduced Dexter-type host-to-ligand energy transfer required for the sensitization of the Eu³⁺ ions, which will be explained in the following. As shown in **Fig. 4.5(b)**, the maximum luminance in the undoped device increases from 202 cd/cm² without any magnetic field up to 228 cd/cm² under B =235 mT at 17 V, corresponding to a 13%-luminance enhancement. We attribute the higher luminance in the presence of the magnetic field to the increased singlet-to-triplet exciton ratio in the SimCP2:PBD co-host system, enhancing the host-to-guest energy

transfer via Förster process. Detailed reasoning accounting for the luminance enhancement is presented in the following.

In Chapter 1, we pointed out that the efficiency of OLEDs can be enhanced under external magnetic fields. This is in fact due to the magnetic field-perturbation of the quantum-statistical 1:3 spin distribution between singlet (S_0 : $|\uparrow\downarrow\rangle - |\downarrow\uparrow\rangle$) and triplet (T_{+1} : $|\uparrow\uparrow\rangle$, T_0 : $|\uparrow\downarrow\rangle + |\downarrow\uparrow\rangle$, T_{-1} : $|\downarrow\downarrow\rangle$) excitonic and electron-hole (e-h) polaron pair manifolds, mostly due to the hydrogen hyperfine interaction. Indeed, a magnetic field can effectively reduce the rate of ISC between the singlet and triplet states, thus increasing the theoretical 25%-singlet density limit. Triplet excited-state energy in fluorescent materials -where there is no heavy metal to favor a spin-orbit coupling- is lost because the transition from T_1 to S_0 is forbidden in such materials.

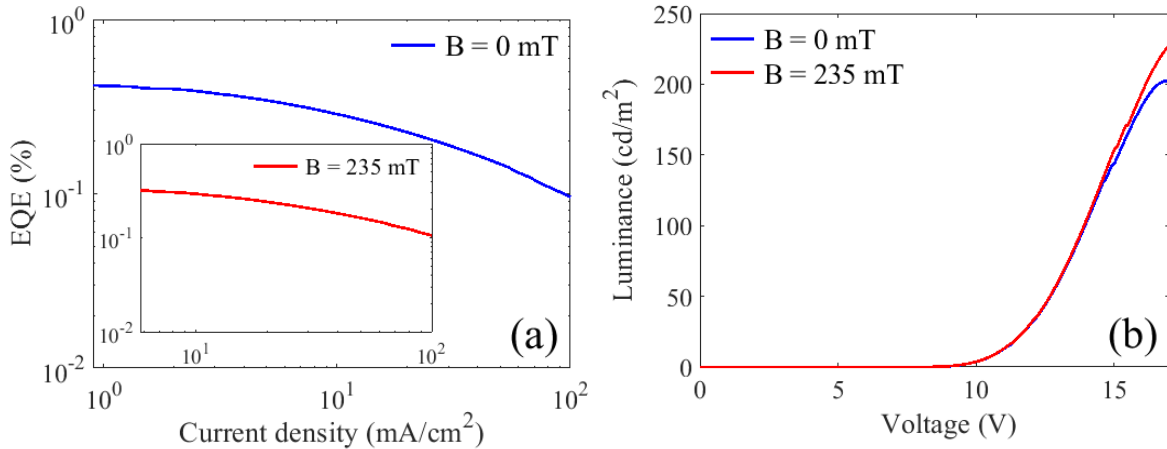


Figure 4.5: (a) External quantum efficiency (EQE) vs. current density, and (b) luminance vs. voltage characteristics of the undoped device.

Nevertheless, the triplet energy -that is lost in the absence of a magnetic field- can be partially converted into the singlet energy in the presence of an applied magnetic field, resulting in an enhanced luminance. In that context, as the singlet-to-triplet exciton ratio in the fluorescent SimCP2 and PBD host materials increases under $B = 235$ mT, the increased singlet energy can be

effectively transferred from the singlet energy levels of the host materials to the singlet energy levels of the ligands via the long-range and fast Förster process. This energy then cascades into the triplet levels of the ligands through ISC, which subsequently excites the Eu^{3+} ions, leading to a higher luminance. As shown in **Fig. 4.3(a)**, there is a significant overlap between the PL spectra of the host materials and the absorption spectrum of $\text{Eu}(\text{DBM})_3\text{Phen}$. This indicates that, under the magnetic field, as the singlet-to-triplet exciton ratio in the host materials increases, the singlet excitation energy of the co-host system is efficiently absorbed by the Eu^{3+} -complex via Förster-type energy transfer process, enhancing the luminance of the devices. However, since the relatively large external magnetic field of $B = 235$ mT can effectively lift the degeneracy of the triplet (T_{+1} : $|\uparrow\uparrow\rangle$, T_0 : $|\uparrow\downarrow\rangle + |\downarrow\uparrow\rangle$, T_{-1} : $|\downarrow\downarrow\rangle$) sub-states (due to the Zeeman splitting [222,237]) on the host and the lanthanide complex molecules, it can reduce the Dexter-type host-to-ligand energy transfer rate between the triplet states of the host materials and the ligands (*antenna effect*). Under the magnetic field, this may explain the slight decrease in the maximum EQE and the observed shift in the voltage at which the EQE has its maximum value. Nevertheless, such a mechanism may lead to a reduced roll-off by suppressing the T-T annihilation in OLEDs.

The EQE vs. current density and luminance vs. voltage plots of the device containing the Fe_3O_4 nanoparticles (hereafter the NP-doped device) without and with the external magnetic field are shown in **Fig. 4.6**. As **Fig. 4.6(a)** displays, without any magnetic field, this device shows an EQE of 0.36 % at 1.1 mA/cm² and 11.3 V, which is slightly lower than that of the undoped device. Indeed, this could be explained by the fact that the Fe_3O_4 nanoparticles are absorptive in a very broad spectral range overlapping with the emission in the device (see **Fig. 4.7**). The voltage (11.3 V) at which the maximum EQE has its maximum value is also shifted because the magnetic nanoparticles can trap charge carriers in OLEDs [329]. Under $B = 235$ mT, the EQE drops to 0.21

% at 10 mA/cm² and 13 V. Further, as shown in **Fig. 4.6(b)**, the maximum luminance of this device increases from 185 cd/cm² without any magnetic field up to 216 cd/cm² under B = 235 mT, showing a 17%-enhancement.

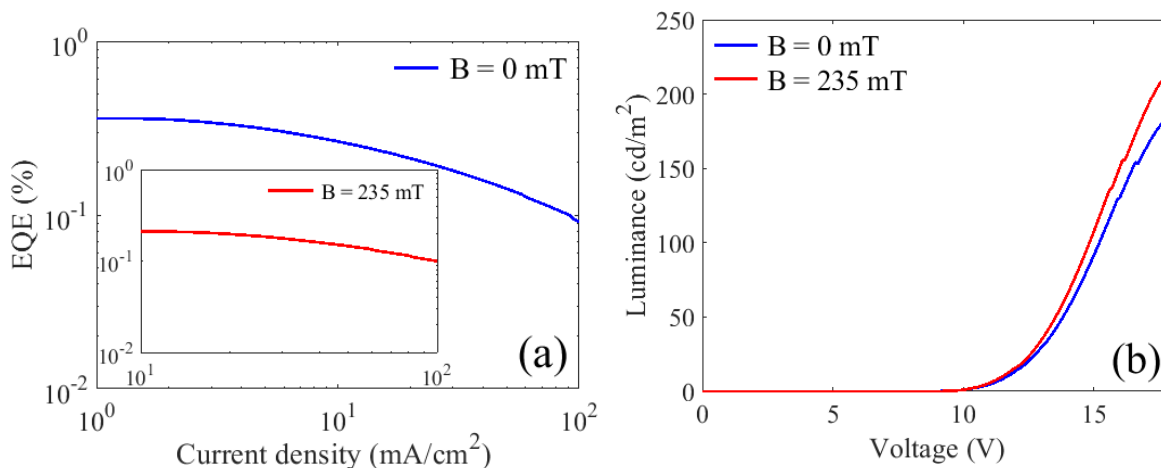


Figure 4.6: (a) External quantum efficiency (EQE) vs. current density and (b) luminance vs. voltage characteristics of the NP-doped device.

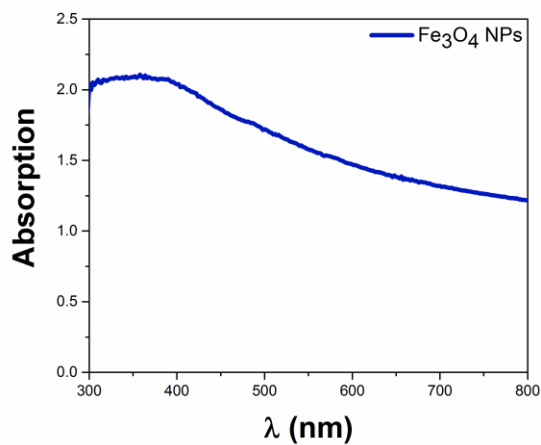


Figure 4.7: Absorption spectrum of magnetite (Fe₃O₄) nanoparticles dispersed in dichloromethane.

4.4.2 Efficiency Roll-Off Analysis

Notably, the EQE roll-off characteristics of the devices improve under the applied magnetic field. In the undoped device, without any magnetic field, the roll-off ratio that by definition is taken from the difference between the maximum EQE and the EQE at the luminance of 100 cd/m² ($\text{EQE}_{\text{max}} - \text{EQE}_{100}$) is found to be 54%. Such a severe EQE roll-off is typically attributed to the T-T and T-P annihilation mechanisms occurring in host materials (host-host annihilation) and in lanthanide complexes (guest-guest annihilation) in lanthanide-based OLEDs [303-309]. However, under $B = 235$ mT, the roll-off ratio decreases to $34 \pm 3\%$, showing a 37%-improved roll-off. By applying the magnetic field, the EQE roll-off characteristic in the NP-doped OLED improves even more. In this device, while the roll-off ratio is 56% without any magnetic field, it decreases to only $19 \pm 3\%$ under $B = 235$ mT, showing a 66%-improved roll-off. This roll-off ratio is comparable with the lowest roll-off ratios (12-19%) previously reported for Eu^{3+} -based OLEDs [302,305]. We also anticipate that application of our approach to the devices reported in Ref. [302,305] should lead to even lower roll-off ratios.

Another important parameter that quantifies the EQE roll-off in OLEDs is the critical current density ($J_{1/2}$) at which the EQE drops to half of its maximum value [46]. Devices with low $J_{1/2}$ exhibit severe roll-off behaviors. In the undoped device without any magnetic field, the $J_{1/2}$ is 23.9 mA/cm². However, under $B = 235$ mT, the $J_{1/2}$ increases up to 50.7 mA/cm². In the NP-doped device, while the $J_{1/2}$ is 29.8 mA/cm² in the absence of the magnetic field, it increases up to 89 mA/cm² under $B = 235$ mT. These $J_{1/2}$ values are the highest ever reported for the Eu^{3+} -based OLEDs (for example, see Ref. [303,304]). These results clearly confirm the efficient suppression of the EQE roll-off behavior in terms of $J_{1/2}$.

To elucidate the role of exciton annihilation mechanisms in the EQE roll-off characteristics, we apply the T-T and T-P models described in Chapter 2 to our experimental EQE plots. As **Fig. 4.8** and **Fig. 4.9** display, we obtain a good agreement between the experimental data and the T-P model in the presence and absence of the applied magnetic field for both the undoped and NP-doped devices (see the fitting parameters in the captions of **Fig. 4.8** and **Fig. 4.9**). In both the undoped and NP-doped devices without and with the magnetic field, the T-T model results in a poor fit (plots not shown). Similar to the results presented in Chapters 2 and 3, this indicates that the T-P model is primarily responsible for the severe EQE roll-off in both the undoped and NP-doped devices without the magnetic field. However, our analysis confirms that the magnetic field suppresses the T-P annihilation process. For example, compare the EQE at the current density of 100 mA/cm^2 for the undoped and NP-doped devices without and with the magnetic field.

In the T-P annihilation process, the energy of a triplet exciton is transferred to an electron or a hole polaron via Förster-type energy transfer mechanism, which quenches the triplet exciton and subsequently creates a singlet exciton and a polaron (see right part in **Fig. 4.10**) [69-73]. In the present work, the T-P annihilation is reduced because the external magnetic field decreases the exciton triplet density in the co-host system, lowering the probability for T-P interactions on the host molecules. This in turn may simultaneously suppress the S-P annihilation on the host molecules (see left part in **Fig. 4.10**), due to the increased singlet-to-triplet population that seems to be large at high current densities. This is indeed in accord with the enhanced luminance of the devices, which is due to the increased singlet population and subsequently improved host-to-guest energy transfer. This observation suggests that our approach for the suppression of efficiency roll-off may even work better for fluorescent OLEDs. As a result, the net effect of the magnetic field

is reducing the host-host exciton-polaron annihilation mechanisms while enhancing the luminance of the devices.

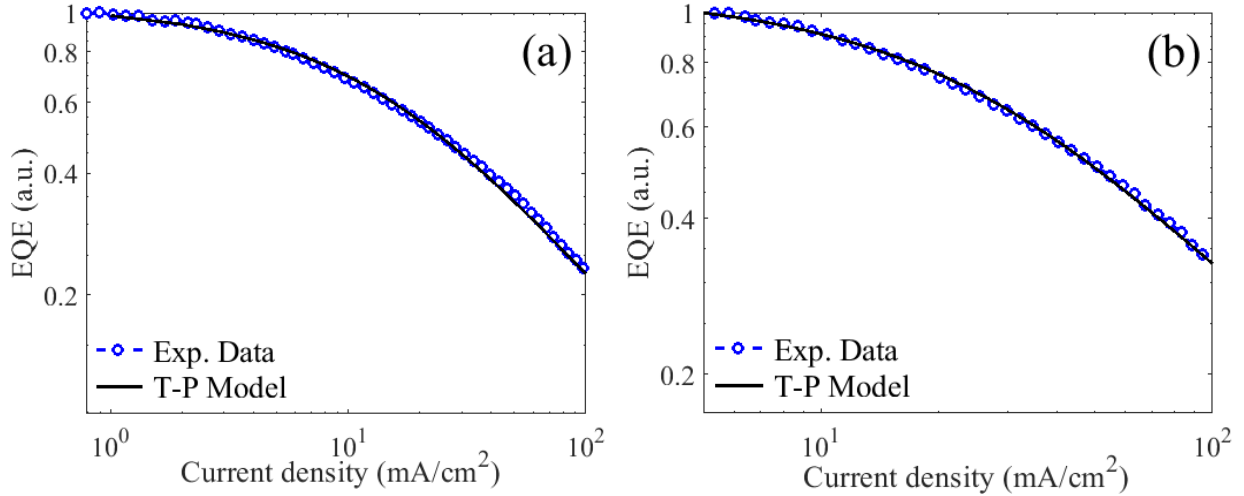


Figure 4.8: Normalized external quantum efficiency (EQE) vs. current density plots of the undoped device under (a) $B = 0$ ($J_e = 19.63 \text{ mA/cm}^2$, $m = 0.08$), and (c) $B = 235 \text{ mT}$ ($J_e = 37.05 \text{ mA/cm}^2$, $m = 0.14$) fitted to the T-P model.

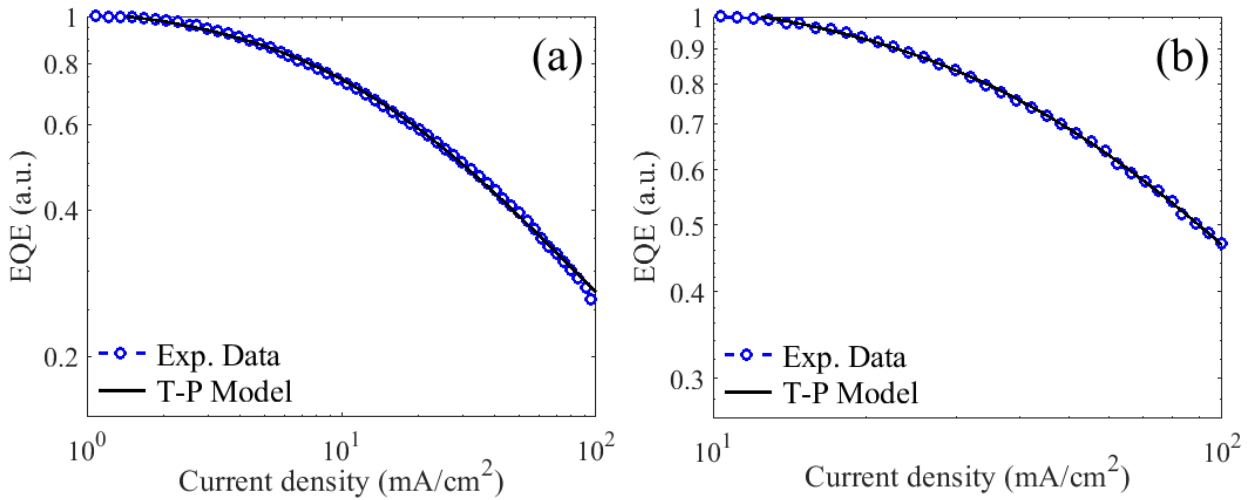


Figure 4.9: Normalized external quantum efficiency (EQE) vs. current plots of the Fe_3O_4 -doped device under (a) $B = 0$ ($J_e = 20.54 \text{ mA/cm}^2$, $m = 0.08$), and (c) $B = 235 \text{ mT}$ ($J_e = 64.86 \text{ mA/cm}^2$, $m = 0.23$) fitted to the T-P model.

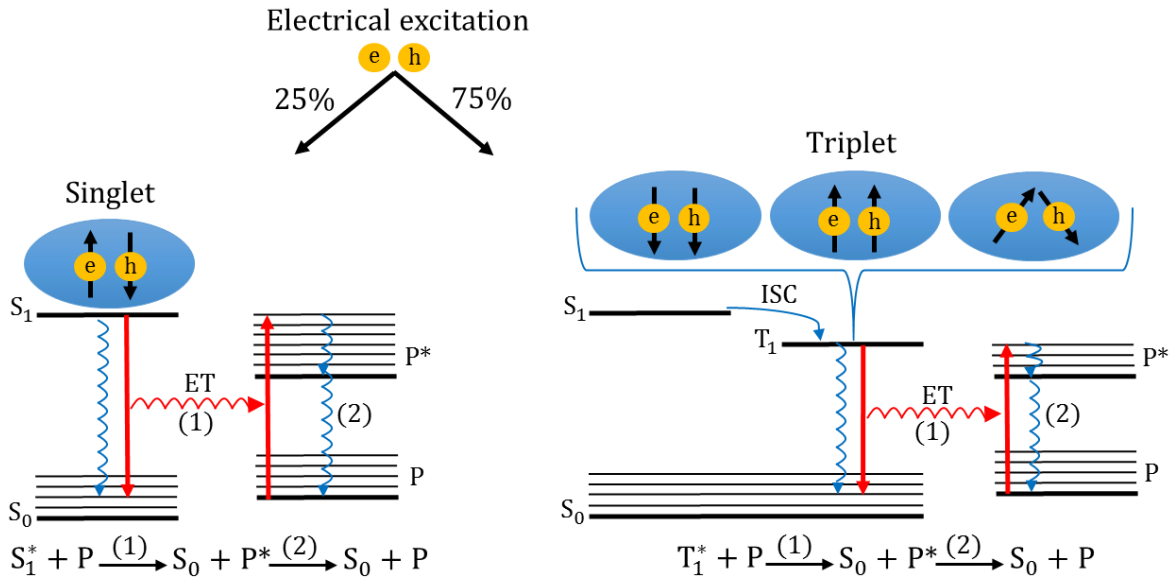


Figure 4.10: Schematic of singlet-polaron and triplet-polaron annihilation. Upon electrical excitation, singlet (S_1) and triplet (T_1) excitons form based on the relative spins of electron and hole polarons. The singlet and triplet excitons then relax either radiatively (red) or non-radiatively (blue), returning to the singlet ground state S_0 . The radiative energies of the singlet and triplet excitons are transferred via long-range Förster process to the electron and hole polarons in the ground state (P) accumulated at the organic/organic layers. This promotes the polarons to the upper excited states (P^*), which then relax non-radiatively back to the ground state. ISC: $S_1 \rightarrow T_1$ intersystem crossing. ET: energy transfer.

Chapter 5: Possibility of Light Extraction Enhancement by Incorporating Azobenzene Photo-Induced Plasmonic Gratings into Lanthanide-based OLEDs

In the previous chapters, we used some approaches to reduce the efficiency roll-off mechanisms in our lanthanide-based OLEDs through optimizing the excitonic and charge transport processes in the devices. Besides, it is important to enhance the maximum achievable EQE and luminance of OLEDs for their practical applications in display and lighting technologies. In Chapter 1, we pointed out that waveguiding effects occurring in the organic layers and in the glass substrate together with coupling of the light to the SPPs at the organic/cathode interface limit the light outcoupling efficiency of OLEDs to ca. 20-30%. We also stated that the light outcoupling efficiency can be enhanced by incorporating SPP gratings into OLED structures. Gratings can be fabricated using various nanolithography techniques [330]. However, most of these techniques are expensive and require several fabrication steps. In this chapter, we study the possibility of using a simple and all-optical lithography method that can be used to enhance the light outcoupling efficiency of red-emitting Eu^{3+} -based OLEDs. The technique is based on inscribing diffraction gratings on a photo-responsive Azo-functionalized small molecule material by one-step two-beam laser lithography method. We show that even though the preliminary attempts for enhancing the light outcoupling efficiency of the grating-incorporated devices were not successful, further optimization of the fabrication parameters may lead to efficient light extraction using the fabricated surface plasmon gratings in the future.

5.1 Surface Relief Gratings based on Photo-Responsive Materials

Azobenzene photo-responsive polymers (Azo-functionalized polymers) are known for their mechanical behavior under illumination of light or temperature change [331-335]. The photomechanical behavior of this class of photo-responsive polymers is based on the reversible

isomerization between the *cis* and *trans* geometric isomers, as shown in **Fig. 5.1**. This class of polymers has attracted a lot of interest in many applications such as solar cells [336], light emitting devices [337], biological sensors [338], organic lasers [339], nonlinear optics and data storage [340,341] etc. In addition, in contrast to polymers, photo-responsive Azo-functionalized small molecules have the advantage of being monodispersed, which provides an easier sensitization and purification process together with a more uniform behavior [342].

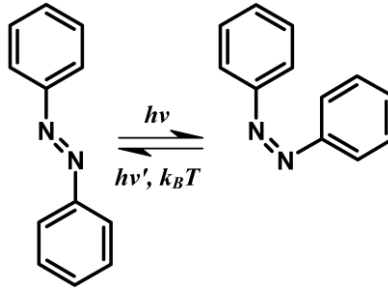


Figure 5.1: Molecular structures of Azobenzene-based chromophores can change in response to light and temperature. Adapted with permission from Ref. [331].

5.2 Design of Plasmonic Gratings and Grating-Assisted Light Outcoupling Structures

We stated earlier in Chapter 1 that SPPs cannot be excited by illuminating an EM wave directly on a planar interface between a metal and a dielectric because of the momentum mismatch of the light in the dielectric and the metal. A surface plasmon grating can be utilized as a powerful phase-matching tool to resolve the momentum mismatch issue if the incident light on a corrugated metal/dielectric interface has its polarization along the grating vector. This situation is schematically shown in **Fig. 5.2**. Phase matching takes place when the below condition is fulfilled:

$$k_{SPP} = k_{x,in} + \Delta k_x \quad (5.1)$$

where $k_{x,in}$ and Δk_x are the x-component of the wavevector (or momentum) of the TM-polarized incident light and m^{th} order of the refracted light (see **Fig. 5.2**). Eqn. 5.1 implies that SPPs can be

excited when the incident light is diffracted into them. The role of the grating here is to provide a quasi-wavevector of Δk_x (called *grating wavevector*) to $k_{x,in}$, which is given by [274]:

$$k_{x,in} = (\omega/c) \sin \theta_i \sqrt{\epsilon_d} \quad (5.2)$$

$$\Delta k_x = m \left(\frac{2\pi}{\Lambda} \right), \quad m = \pm 1, \pm 2, \dots \quad (5.3)$$

where ω is the frequency of the incident light, c is the speed of light in vacuum, θ_i is the angle of incidence, ϵ_d is the dielectric function of the dielectric medium, Λ is the period (spacing) of the one-dimensional (1D) diffraction grating, and m is the order of diffraction.

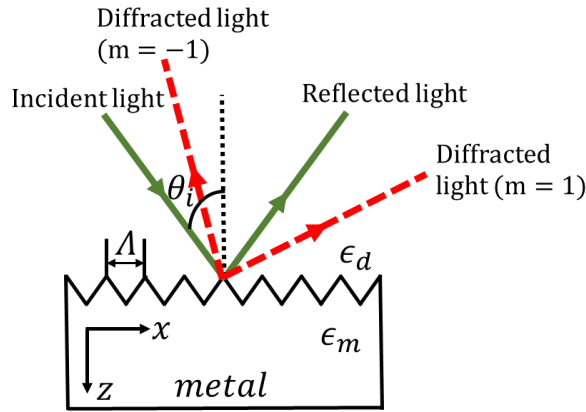


Figure 5.2: Light incident on a 1D metallic diffraction grating.

Having said that, if the metal shown in **Fig. 5.2** is thin enough, the light can diffract to the backside of the metal. Therefore, by depositing a very thin layer of cathode or anode in a bottom-emitting or top-emitting OLED, a large portion of the light trapped inside the device can couple out. To do so, however, it is sometimes required to replicate the corrugation throughout the device structure from the bottom to the top [43,343]. Assuming only the first-order diffraction ($m = 1$) for a single 1D plasmonic grating, the surface plasmon excitation wavelength λ_{SP} can be calculated by the following equation [336]:

$$\lambda_{sp} = n_d \left(\sqrt{\frac{\epsilon_{r,m}}{n_d^2 + \epsilon_{r,m}}} + \sin\theta_i \right) \Lambda \quad (5.4)$$

where λ_{sp} is the surface plasmon wavelength, n_d is the refractive index of the dielectric, $\epsilon_{r,m}$ is the real part of the dielectric function of the metal, θ_i is the angle of incidence, and Λ is the period (spacing) of the grating. Thus, according to Eqn. 5.4, by changing any of these parameters, the surface plasmon excitation wavelength can be tuned. This provides us with a great opportunity to match the surface plasmon excitation wavelength with the emission wavelength of emissive materials in OLEDs so that the emission loss associated with SPPs can be overcome and even turned to an advantage [344].

5.3 Experimental Details on the Fabrication of Plasmonic Gratings

In the present thesis, as shown in **Fig. 5.3**, a small molecule consisting of Disperse Red 1 functionalized with a methylaminotriazine group was employed for the fabrication of plasmonic gratings [342]. This material exhibits very stable glassy phases and uniform film processing properties, enabling fabrication of high-quality surface relief gratings. **Figure 5.4** shows the experimental setup used for the surface relief grating inscription on the photo-responsive glassy small molecule. The procedure for writing surface relief gratings is as follows: First, a thin layer of the photo-responsive material (~200-300 nm) is spin coated from a dichloromethane solution on a glass substrate with the spinning speed and time of 1100 rpm and 20 s, respectively. The spin-coated film is then annealed in an oven at 95 °C for 15 min to remove any remaining solvent. In the configuration shown in **Fig. 5.4**, the substrate has a 90° angle with a Lloyd's mirror placed on a rotating mount. For inscribing the surface relief gratings, half of the inscribing laser beam (532 nm-diode laser) is incident on the sample and the other half is incident on the mirror so that the reflected light from the mirror can interfere with the light incident directly on the sample. The

surface relief gratings on the photo-responsive material are then created through interference of these two beams in a simple, one-step, and all-optical process. For the gratings shown in the following, the optimized exposure time for the one-dimensional (1D) gratings was found to be 60 s. This exposure time results in a good surface plasmon resonance (SPR) by creating relatively deep grooves. The first and second exposure times for the two-dimensional (2D) so-called *crossed-gratings* are also found to be 60 and 30 s, respectively.

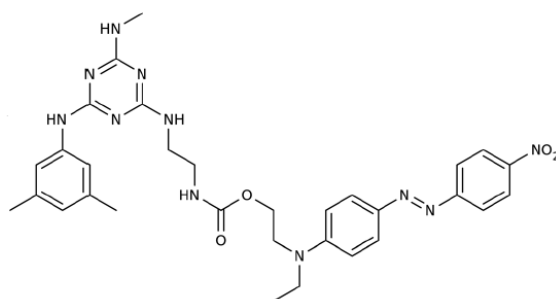


Figure 5.3: Chemical structure of the material used for the fabrication of plasmonic gratings [342].

By changing the wavelength of the laser beam and angle of incidence, the period Λ (or spacing) of the grating can be easily tuned [331]. In addition, the depth of the grating can be controlled by adjusting the irradiance of the laser beam and exposure time [336]. A wide variety of different 1D and 2D diffraction gratings with different grating periods and depths can be fabricated using the procedure described above.

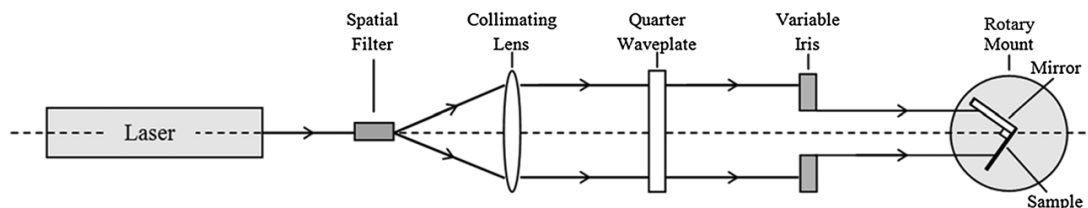


Figure 5.4: Optical setup for surface relief grating inscription. Adapted with permission from [336].

5.4 Results and Discussion

Here, we explore the possibility of using surface plasmon gratings fabricated from the small molecule material described earlier to enhance the light extraction from Eu^{3+} -based OLEDs. Since the peak emission from Eu^{3+} is centered at 612 nm ($\lambda_{\text{SP}} = \lambda_{\text{em}} = 612$ nm) the periods of the surface plasmon gratings were calculated to be about 350 nm by using Eqn. 5.4. This was done by taking into calculation the refractive index of PEDOT:PSS ($n_d = 1.5$ [345]) -that is in the immediate contact with the gratings in the devices- and the real part of the dielectric function of Au ($\epsilon_m = -9.08$ [346]), both at the emission wavelength of Eu^{3+} . After inscribing the gratings, a 100 nm thick layer of Au was deposited onto the gratings to make the gratings reflective enough for the SPR measurements, as described in the following. After that, a layer of water-soluble polyvinyl alcohol (PVA) (1 wt.%) ($n_d = 1.5$) was spin coated onto the surface relief gratings. PVA was used, prior to the fabrication of actual OLEDs, to find the optimized grating spacing because the refractive index of PVA is as the same as for PEDOT:PSS. A variety of gratings with different exposure times and periods were fabricated but only the best results are shown herein. **Figure 5.5** shows the SPR reflectance spectra for the PVA-coated 1D and 2D surface relief gratings with different periods. In this figure, the reflectance spectrum for each grating shows a dip at the SPR wavelength, due to coupling to the SPPs at the Au/PVA interface. **Figures 5.5 (b-d)** also indicate that 1D and 2D gratings with a period of 350-355 nm should provide good diffraction for the emission of Eu^{3+} because the PL spectrum of Eu^{3+} is located at the edge of these SPR spectra. The grating with the period of 340 nm is not suitable because its SPR spectrum occurs almost at the peak emission of Eu^{3+} , which may lead to total loss of emission. In this situation, Au can completely absorb the emission, so no diffraction (i.e. light extraction from OLEDs) will be obtained. As shown in **Fig. 5.5(c)**, the biggest advantage of 2D over 1D gratings is that both TM

and TE modes can excite the SPPs in 2D gratings, giving rise to more effective light extraction [347]. However, the SPR spectrum for the TE-polarized light is shallower than that for the TM-polarized light. **Figure 5.6** displays the AFM images of the gratings shown in **Fig. 5.5**. The grating periods obtained from AFM image analysis are in good agreement with the calculated periods. The grating depths were also found to be in the 40-60 nm range on different spots on the samples.

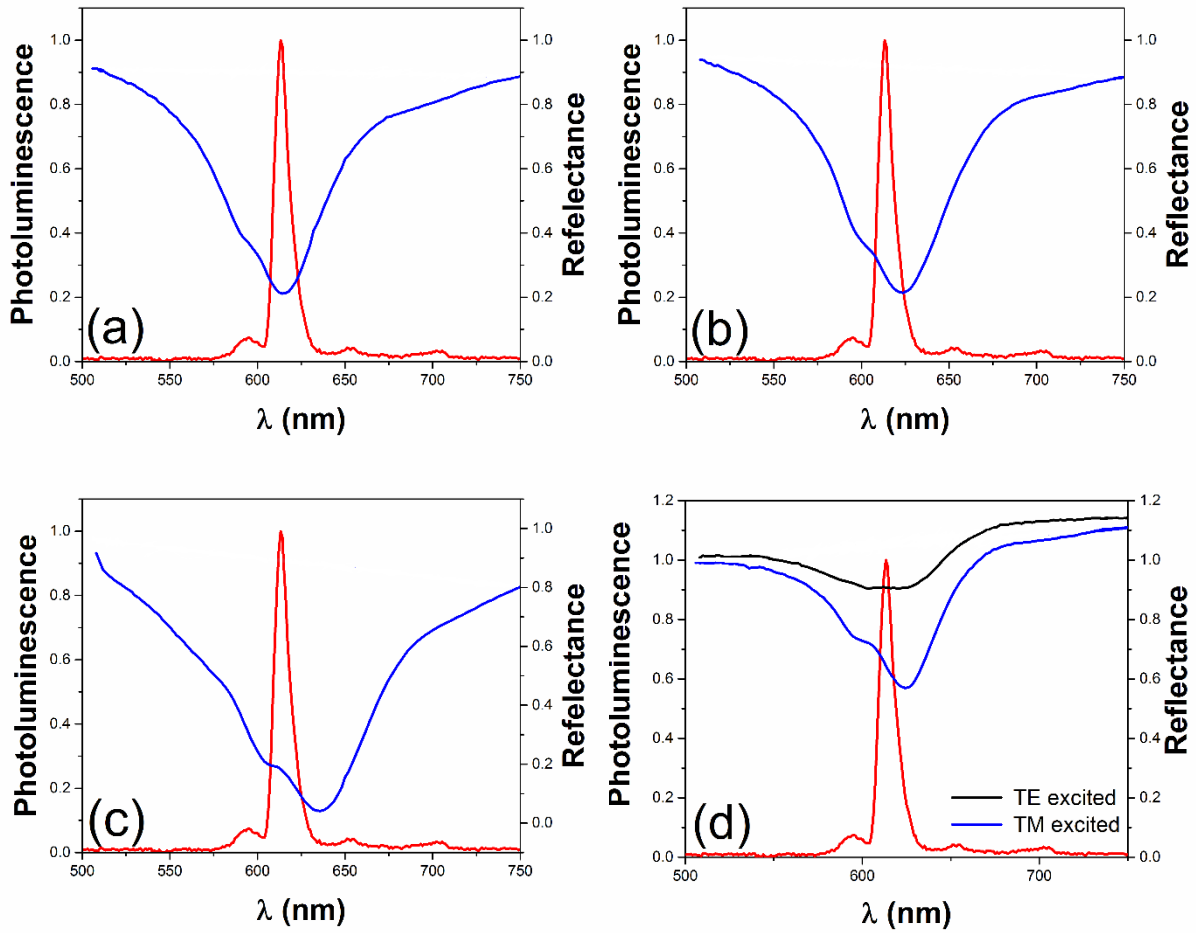
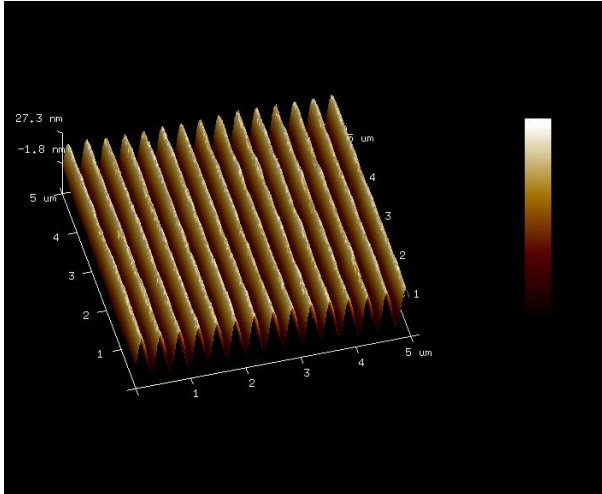
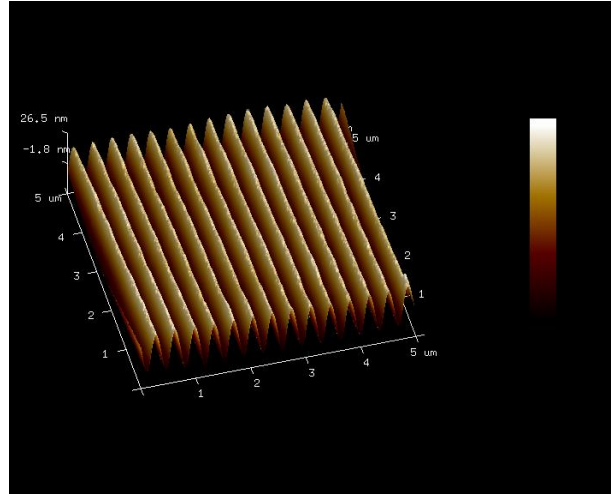


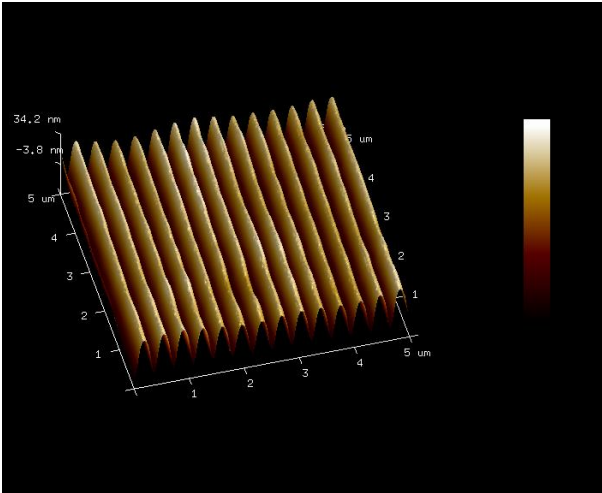
Figure 5.5: Reflectance SPR spectra of Au-coated 1D surface plasmon gratings with different periods: (a) $\Lambda=340$ nm, SPR=616 nm; (b) $\Lambda=350$ nm, SPR=624 nm; (c) $\Lambda=355$ nm, SPR=636 nm; (d) $\Lambda_1=\Lambda_2=350$ nm, SPR=626 nm.



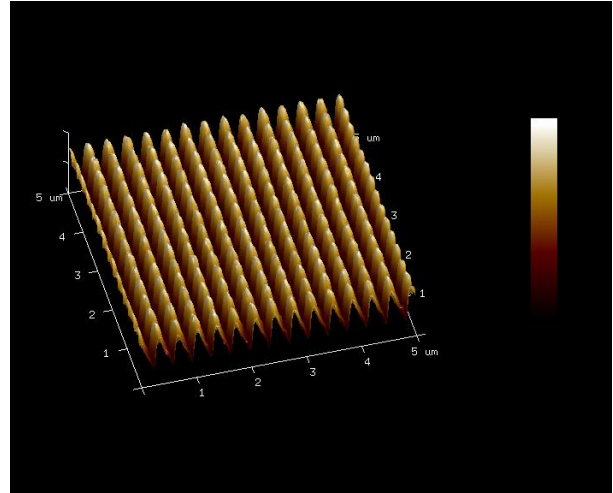
(a)



(b)



(c)



(d)

Figure 5.6: AFM images of 1D and 2D gratings. (a) $\Lambda=340$ nm, (b) $\Lambda=350$ nm, (c) $\Lambda=355$ nm, (d) (Au-coated) $\Lambda_1= \Lambda_2=350$ nm.

In the next step, some gratings were designed for the OLED structure reported in Chapter 4 but without the transparent ITO electrode. After inscribing the gratings, the following structure was fabricated on the gratings: Au(100 nm)/PEDOT:PSS(35 nm)/SimCP2:PBD:Eu(DBM)₃Phen (30:70:5 wt.%) (64 nm)/BCP(10 nm):Alq3(40 nm). The Au layer was deposited by magnetron sputtering technique. **Figure 5.7** shows the SPR spectra for different grating periods. Apparently,

the gratings shown in **Fig. 5.7(a-c)** are not suitable for light extraction enhancement because of the aforementioned reason for the PVA-coated grating with the period of 340 nm. Nevertheless, the grating with the period of 370 nm shown in **Fig. 5.7(d)** seems to be the best structure for light extraction enhancement. This is because the peak emission of Eu^{3+} is located perfectly at the edge of the SPR spectrum of the grating with the spacing of 370 nm. **Figure 5.8** displays the 1D and 2D AFM images for this grating.

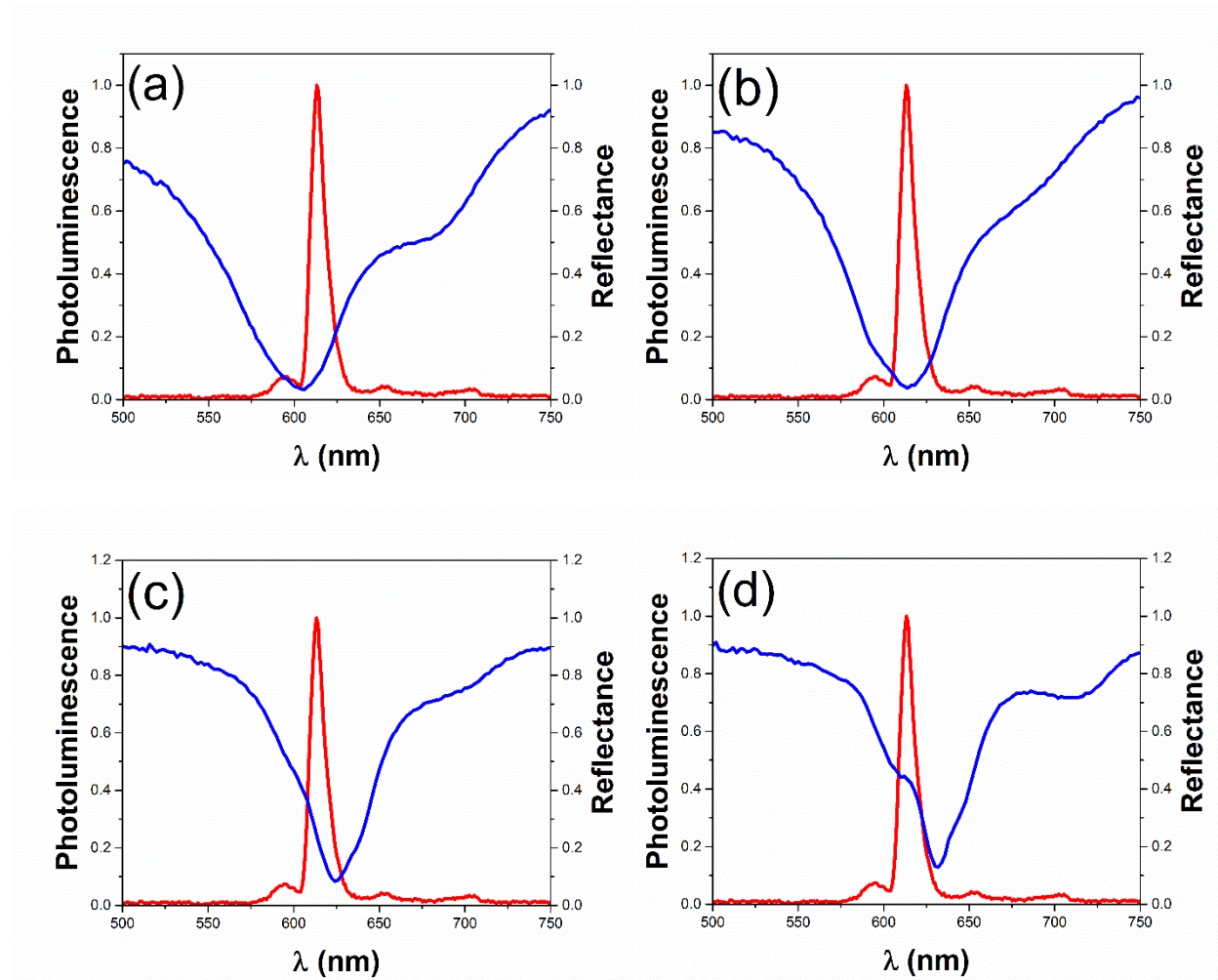


Figure 5.7: Reflectance SPR spectra of Au-coated 1D surface plasmon gratings with different periods for OLEDs: (a) $\Lambda=340$ nm, SPR=606 nm; (b) $\Lambda=350$ nm, SPR=614 nm; (c) $\Lambda=360$ nm, SPR=624 nm; (d) $\Lambda=370$ nm, SPR=632 nm.

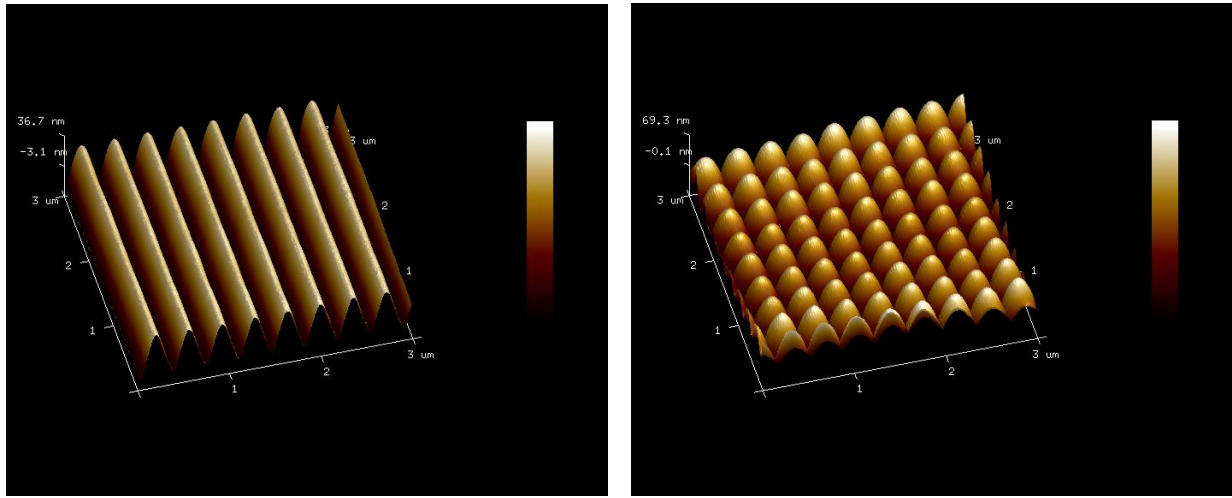


Figure 5.8: 1D and 2D AFM images of the gratings with $\Lambda=370$ nm and SPR=632 nm.

Knowing the optimized grating structure, some 1D and 2D grating-incorporated OLEDs were fabricated with the following structure: Au(15 nm)/PEDOT:PSS(35 nm)/SimCP2:PBD:Eu(DBM)₃Phen (30:70:5 wt.%) (64 nm)/BCP(10 nm):Alq3(40 nm)/LiF(0.8 nm)/Al (100 nm). The bottom Au contact was 15 nm thick to provide a transparent anode [347]. Au was used as the anode because it has a workfunction of -4.8 eV (with respect to the vacuum level), enabling injection of holes. One reference device was also fabricated on an Au (15 nm)-coated photo-responsive material without any grating. However, in the case of the reference device, due to the low conductivity of the Au contact, the EQE was one order of magnitude lower than what was reported in Chapter 4. The conductivity of the grating-incorporated devices were even worse on different OLEDs fabricated on the same substrate, which made the results not to be reliable in terms of light extraction enhancement. The main reason accounting for the bad conductivity of the devices is likely that Au does not form a good contact with the photo-responsive material. Particularly, since the turn-on voltages of the Eu³⁺-based OLEDs fabricated on highly-

conductive ITO substrates are already high (~ 10 V, see Chapter 4), a very thin layer of Au layer - that is not as much conductive as ITO- results in a much higher driving voltage, which lowers the efficiency dramatically. This situation causes a degradation in the case of the grating-incorporated devices because the 15-nm Au layer is not a smooth film and the grooves are deep, adding another issue to the low conductivity.

Chapter 6: Conclusions and Future Work

The NIR-emitting OLEDs presented in Chapter 2 showed the highest maximum EQE values ever reported for solution-processed Nd³⁺-based devices, which also exhibited very low efficiency roll-off characteristics particularly at high current densities. This was achieved due to the direct formation of excitons on the NIR emitter, improvement of the host-to-guest energy transfer, selection of a host material with high T₁ energy that prevents energy-back transfer from the guest to host molecules and strongly reduces the quenching by T-T annihilation. However, as stated in the previous chapters, the NIR light in a NIR OLED is strongly absorbed by the organic materials and also by the ITO substrate. As **Fig. 6.1** displays, a large portion of the NIR light at a wavelength of 1060 nm is absorbed by the ITO substrate. The reabsorption issue should be resolved to fabricate highly efficient NIR devices suitable for practical applications. The device efficiency presented in Chapter 1 can be further improved by employing single host materials having higher PLQY, which would provide more efficient host-to-guest energy transfer via Förster process if the PL of the host material overlaps significantly with the absorption of the ligands. Additionally, host materials with better charge transport characteristics can enhance the efficiency of the NIR devices. Thus, future work should focus on the following: i) Improvement of the host-to-ligand energy transfer while keeping an appropriate energy level alignment between the HOMO and LUMO energy levels of the ligands and those of the host material for an efficient charge injection into the ligands. Deep-blue-emitting bipolar materials with high T₁ energy level can be considered as suitable host systems to improve the efficiency of single-host NIR devices, which can also reduce exciton-exciton and exciton-polaron annihilation mechanisms. ii) The use of fluorinated/deuterated host molecules and organic ligands to reduce the absorption of the NIR emission by high-energy C-H

and O-H group vibrations. iii) Replacement of ITO by other metal oxide electrodes that are more transparent in the NIR region [348,349].

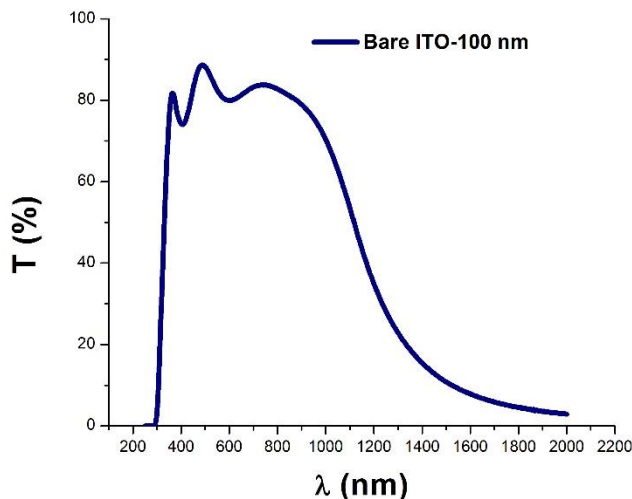


Figure 6.1: Transmittance spectrum of a 100 nm thick ITO-coated glass substrate.

In Chapter 3, we demonstrated that employing an *exciplex-forming* co-host system can improve the EQE of the complex in the NIR OLED by more than 50%. Direct charge trapping by the complex as well as host-to-guest energy transfer from the singlet and triplet exciplexes formed between the host materials contributed simultaneously to the enhanced EQE. Further, the binary host system provided a balanced charge transport in the device. The device also exhibited a very low efficiency roll-off, due to the reduced T-P annihilation. While exciplex systems comprising donor and acceptor materials typically exhibit TADF behavior, they are not as efficient as TADF compounds where donor and acceptor groups are chemically bound to each other. On the other hand, as stated earlier, the host-to-guest energy transfer in an OLED is efficient when the emission from the host (or co-host) overlaps substantially with the absorption of the ligands. However, in Chapter 3, the exciplex emission does not overlap with the absorption of the NIR complex, which limits the host-to-guest energy transfer mainly to the short-range Dexter process that is less

efficient than the long-range Förster process. Therefore, future work should focus on the following: Employing blue-emitting exciplex co-host systems that can transfer their singlet and triplet excitation energies to the NIR complex more efficiently via both Förster and Dexter mechanisms. Since achieving efficient host-to-guest energy transfer via Förster process may be difficult in exciplex co-host systems, due to the fact that the exciplex PL spectrum is typically red-shifted with respect to the PL spectra of the constituent materials, employing efficient deep-blue-emitting TADF compounds as host materials should result in some efficiency enhancement.

The straightforward, easy-to-implement, and effective approach presented in Chapter 4 for the suppression of triplet-polaron annihilation mechanism and the improvement of the Eu^{3+} -based OLED luminance may establish a path towards the fabrication of lanthanide-based roll-off-less devices with enhanced luminance. This is particularly important for the realization of electrically pumped organic semiconductor lasers based on lanthanide complexes. In that context, future work should focus on further optimization of the device structure, applying magnetic fields with different magnitudes, and using different concentrations of the Fe_3O_4 nanoparticles, which should lead to improved luminance enhancement and roll-off reduction. Even though previous studies have proven that an external magnetic field can effectively increase the singlet-to-triplet density in OLEDs, more experiments are required to estimate the singlet and triplet population in the co-host system under the applied magnetic field. This can be done, for example, by the time-resolved magneto-electroluminescence technique under pulsed electric field (at different voltages).

Overall, the results presented in this thesis demonstrate that by careful control of the charge transport and excitonic processes, visible and NIR-emitting lanthanide-based OLEDs may be promising devices for the fabrication of highly efficient light sources for OLED applications and the realization of electrically driven OSLs. However, many parameters should be optimized in

terms of minimizing the exciton-exciton and exciton-polaron annihilation mechanisms at high current densities, enhancing the host-to-guest energy transfer mechanism, optimizing the device architecture to achieve high efficiency, and improving the charge transport processes to be able to inject a large amount of current to achieve lasing. Particularly, in the latter case, future work should focus on using highly conductive metal oxides as ETL and HTL in the device structure [350-352]. In addition to the high conductivity, unlike organic materials, metal oxides can sustain the high temperatures (Joule heating) created under large current densities. Metal oxides are also more transparent in the NIR spectral region, which would reduce the losses due to the NIR light reabsorption in the NIR-emitting lanthanide-based devices. Furthermore, to inject a large amount of current, p-i-n structures can be used to make barrier-less (Ohmic) contacts at the organic interfaces [353].

Finally, considering the possibility of light extraction enhancement using the surface plasmon gratings reported in Chapter 5, future work should focus on the following: i) The Au layer thickness should be optimized. ii) Silver (Ag) is less lossy compared with Au, so it may be possible to use a relatively thicker layer of Ag as the bottom transparent contact to resolve the low conductivity issue. iii) Since the photo-responsive material presented in Chapter 5 is strongly absorptive for wavelengths below 600 nm, unfortunately, it is unusable for blue and green-emitting materials. However, previous studies have shown that by bleaching the Azo-functionalized photo-responsive materials, they become transparent in the visible spectral range [354]. Thus, taking advantage of this possibility, it would be possible to bleach and optimize the grating structures to enhance the light outcoupling efficiency of blue and green-emitting lanthanide complex-based OLEDs as well as phosphorescent and fluorescent devices.

Bibliography

- [1] C. W. Tang and S. A. VanSlyke, *Appl. Phys. Lett.* **51**, 913 (1987).
- [2] R. H. Friend, R. W. Gymer, A. B. Holmes, J. H. Burroughes, R. N. Marks, C. Taliani, D. D. C. Bradley, D. A. Dos Santos, J. L. Brédas, M. Lögdlund & W. R. Salaneck, *Nature* **397**, 121 (1999).
- [3] Y.-S. Tyan, *J. Photon. Energy, SPIE* **1**, 011009 (2011).
- [4] S. Hameed, P. Predeep, and M. R. Baiju, *Rev. Adv. Mater. Sci.* **26**, 30 (2010).
- [5] W. Brütting and C. Adachi (Ed.), *Physics of Organic Semiconductors*, WILEY-VCH Verlag, Weinheim, (2012).
- [6] R.-P. Xu, Y.-Q. Li, and J.-X. Tang, *J. Mater. Chem. C* **4**, 9116 (2016).
- [7] H.-W. Chen, J.-H. Lee, B.-Y. Lin, S. Chen and S.-T. Wu, *Light: Science & Applications* **7**, 17168 (2018).
- [8] <https://www.oled-info.com>.
- [9] S. Reineke, M. Thomschke, B. Lüssem, and K. Leo, *Rev. Mod. Phys.* **85**, 1245 (2013).
- [10] B. Geffroy, P. le Roy, and C. Prat, *Polym. Int.* **55**, 572 (2006).
- [11] W. Brütting, J. Frischeisen, T. D. Schmidt, B. J. Scholz, and C. Mayr, *Phys. Status Solidi A* **210**, 44 (2013).
- [12] K. Mullen, U. Scherf, *Organic Light-Emitting Devices*, WILEY-VCH Verlag, Weinheim, (2006).
- [13] H. Yersin, A. F. Rausch, R. Czerwieniec, T. Hofbeck, T. Fischer, *Coord. Chem. Rev.* **255**, 2622 (2011).
- [14] A. Köhler, H. Bässler, *Mat. Sci. Eng. R* **66**, 71 (2009).
- [15] C. Adachi, M. A. Baldo, M. E. Thompson, and S. R. Forrest, *J. Appl. Phys.* **90**, 5048 (2001).
- [16] C. Adachi, *Jpn. J. Appl. Phys.* **53**, 060101 (2014).
- [17] H. Uoyama, K. Goushi, K. Shizu, K. Nomura, and C. Adachi, *Nature* **492**, 234 (2012).
- [18] Q. Zhang, B. Li, S. Huang, H. Nomura, H. Tanaka, and C. Adachi, *Nat. Photon.* **8**, 326 (2014).
- [19] S. Hirata, Y. Sakai, K. Masui, H. Tanaka, S. Y. Lee, H. Nomura, N. Nakamura, M. Yasumatsu, H. Nakanotani, Q. Zhang, K. Shizu, H. Miyazaki, and C. Adachi, *Nat. Mater.* **14**, 330 (2015).
- [20] H. Nakanotani, T. Higuchi, T. Furukawa, K. Masui, K. Morimoto, M. Numata, H. Tanaka, Y. Sagara, T. Yasuda, and C. Adachi, *Nat. Common.* **5**, 4016 (2014).
- [21] H. Nakanotani, K. Masui, J. Nishide, T. Shibata, C. Adachi, *Sci. Rep.* **3**, 2127 (2013).
- [22] Q. Zhang, D. Tsang, H. Kuwabara, Y. Hatae, B. Li, T. Takahashi, S. Y. Lee, T. Yasuda, and C. Adachi, *Adv. Mater.* **27**, 2096 (2015).
- [23] S. R. Forrest, D. D. C. Bradley, and M. E. Thompson, *Adv. Mater.* **15**, 1043 (2003).

- [24] Z. Li, H. Meng (Ed.), *Organic Light-Emitting Materials and Devices*, Taylor & Francis Group, Boca Raton (2007).
- [25] Y. Tao, C. Yang, J. Qin, *Chem. Soc. Rev.* **40**, (2011) 2943.
- [26] D. M. Mattox, *Handbook of Physical Vapor Deposition (PVD) Processing*, Elsevier Inc., 2nd Edition, Oxford, (2010).
- [27] L. Duan, L. Hou, T.-W. Lee, J. Qiao, D. Zhang, G. Dong, L. Wang, and Y. Qiu, *J. Mater. Chem.* **20**, 6392 (2010).
- [28] K. S. Yook and J. Y. Lee, *Adv. Mater.* **26**, 4218 (2014).
- [29] T.-H. Han, M.-R. Choi, C.-W. Jeon, Y.-H. Kim, S.-K. Kwon, and T.-W. Lee, *Sci. Adv.* **2**, 1 (2016).
- [30] E. Ahmed, T. Earmme, S. A. Jenekhe, *Adv. Funct. Mater.* **21**, 3889 (2011).
- [31] L. Derue, S. Olivier, D. Tondelier, T. Maindron, B. Geffroy, *ACS Appl. Mater. Interfaces* **8**, 16207 (2016).
- [32] M. Zhang, S. Höfle, J. Czolk, A. Mertens, and A. Colsmann, *Nanoscale* **7**, 20009 (2015).
- [33] T. Sano, M. Fujita, T. Fujii, and Y. Hamada, *Jpn. J. Appl. Phys.* **34**, (1995) 1883.
- [34] K. Saxena, V.K. Jain, and D. S. Mehta, *Opt. Mat.* **32**, 221 (2009).
- [35] S. Nowy, B. C. Krummacher, J. Frischeisen, N. A. Reinke, and W. Brütting, *J. Appl. Phys.* **104**, 123109 (2008).
- [36] R. Meerheim, M. Furno, S. Hofmann, B. Lüssem, and K. Leo, *Appl. Phys. Lett.* **97**, 253305 (2010).
- [37] K. Meerholz and D. C. Müller, *Adv. Funct. Mater.* **11**, 251 (2001).
- [38] Y. Qu, C. Coburn, D. Fan, and S. R. Forrest, *ACS Photonics* **4**, 363 (2017).
- [39] S. Möller and S. R. Forrest, *Appl. Phys. Lett.* **91**, 3324 (2002).
- [40] J.-B. Kim, J.-H. Lee, C.-K. Moon, S.-Y. Kim, and J.-J. Kim, *Adv. Mater.* **25**, 3571 (2013).
- [41] J. Feng, T. Okamoto, S. Kawata, *Opt. Lett.* **30**, 2302 (2005).
- [42] S. Wedge, J. A. E. Wasey, and W. L. Barnes, *Appl. Phys. Lett.* **85**, 182 (2004).
- [43] S. Wedge, A. Giannattasio, and W.L. Barnes, *Org. Electron.* **8**, 136 (2007).
- [44] B. J. Scholz, J. Frischeisen, A. Jaeger, D. S. Setz, T. C. G. Reusch, and W. Brütting, *Opt. Exp.* **20**, A205 (2012).
- [45] M. A. Baldo, C. Adachi, and S. R. Forrest, *Phys. Rev. B* **62**, 10967 (2000).
- [46] C. Murawski, K. Leo, and M. C. Gather, *Adv. Mater.* **25**, 6801 (2013).
- [47] Y. Luo and H. Aziz, *Adv. Funct. Mater.* **20**, 1285 (2010).
- [48] Z. D. Popovica and H. Aziz, *J. Appl. Phys.* **98**, 013510 (2005).
- [49] S. Reineke, G. Schwartz, K. Walzer, M. Falke, and K. Leo, *Appl. Phys. Lett.* **94**, 163305 (2009).

- [50] D. Kasemann, R. Brückner, H. Fröb, and K. Leo, *Phys. Rev. B* **84**, 115208 (2011).
- [51] S. Reineke, G. Schwartz, K. Walzer, and K. Leo, *Appl. Phys. Lett.* **91**, 123508 (2007).
- [52] B. H. Wallikewitz, D. Kabra, S. Gélinas, and R. H. Friend, *Phys. Rev. B* **85**, 045209 (2012).
- [53] S. Reineke, K. Walzer, and K. Leo, *Phys. Rev. B* **75**, 125328 (2007).
- [54] D. Y. Kondakov, T. D. Pawlik, T. K. Hatwar, and J. P. Spindler, *J. Appl. Phys.* **106**, 124510 (2009).
- [55] C. Ganzorig and M. Fujihira, *Appl. Phys. Lett.* **81**, 3137 (2002).
- [56] D. Y. Kondakov, *J. Appl. Phys.* **102**, 114504 (2007).
- [57] S. M. King, M. Cass, M. Pintani, C. Coward, F. B. Dias, A. P. Monkman, and M. Roberts, *J. Appl. Phys.* **109**, 074502 (2011).
- [58] Y. Zhang and S. R. Forrest, *Phys. Rev. Lett.* **108**, 267404 (2012).
- [59] D. L. Dexter, *J. Chem. Phys.* **21**, 836 (1953).
- [60] A. Ruseckas, J. C. Ribierre, P. E. Shaw, S. V. Staton, P. L. Burn, and I. D. W. Samuel, *Appl. Phys. Lett.* **95**, 183305 (2009).
- [61] S. M. King, D. Dai, C. Rothe, and A. P. Monkman, *Phys. Rev. B* **76**, 085204 (2007).
- [62] H. Nakanotani, H. Sasabe, and C. Adachi, *Appl. Phys. Lett.* **86**, 213506 (2005).
- [63] T. Förster, *Annalen der Physik (in German)* **437**, 55 (1948).
- [64] Y. Zaushitsyn, K. G. Jespersen, L. Valkunas, V. Sundström, and A. Yartsev, *Phys. Rev. B* **75**, 195201 (2007).
- [65] J. Fourny and G. Delacôte, *Phys. Rev. Lett.* **15**, 1085 (1968).
- [66] Y. Zhang, M. Whited, M. E. Thompson, S. R. Forrest, *Chem. Phys. Lett.* **495**, 161 (2010).
- [67] N. C. Giebink and S. R. Forrest, *Phys. Rev. B* **79**, 073302 (2009).
- [68] J. Yu, R. Lammi, A. J. Gesquiere, and P. F. Barbara, *J. Phys. Chem. B* **109**, 10025 (2005).
- [69] Q. Wang, B. Sun, and H. Aziz, *Adv. Funct. Mater.* **24**, 2975 (2014).
- [70] Q. Wang and H. Aziz, *ACS Appl. Mater. Interfaces* **5**, 8733 (2013).
- [71] Y. J. Cho, Y. Zhang, H. Yu, and H. Aziz, *Adv. Funct. Mater.* **26**, 8662 (2016).
- [72] D. Hertel and K. Meerholz, *J. Phys. Chem. B* **111**, 12075 (2007).
- [73] A. S. D. Sandanayaka, K. Yoshida, T. Matsushima, and C. Adachi, *J. Phys. Chem. C* **119**, 7631 (2015).
- [74] E. J. W. List, C.-H. Kim, A. K. Naik, U. Scherf, G. Leising, W. Graupner, and J. Shinar, *Phys. Rev. B* **64**, 155204 (2001).
- [75] W. Stampor, J. Kalinowski, P. Di Marco, and V. Fattori, *Appl. Phys. Lett.* **70**, 1935 (1997).
- [76] J. Kalinowski, and J. Mężyk, F. Meinardi, R. Tubino, M. Cocchi, and D. Virgili, *J. Appl. Phys.* **98**, 063532 (2005).

- [77] J. Szmytkowski, W. Stampor, J. Kalinowski, and Z. H. Kafafi, *Appl. Phys. Lett.* **80**, 1465 (2002).
- [78] Z. D. Popovic and H. Aziz, *J. Appl. Phys.* **98**, 013510 (2005).
- [79] Y. Luo, H. Aziz, Z. D. Popovic, and G. Xu, *Appl. Phys. Lett.* **89**, 103505 (2006).
- [80] K. Yoshida, H. Nakanotani, and C. Adachi, *Org. Electron.* **31**, 287 (2016).
- [81] P. Tyagi, L. I. Giri, S. Tuli, and R. Srivastava, *J. Appl. Phys.* **115**, 034518 (2014).
- [82] K. Yoshida, T. Matsushima, H. Nakanotani, and C. Adachi, *Org. Electron.* **31**, 191 (2016).
- [83] Y. Divayana, B. J. Chen, and X. W. Sun, *Appl. Phys. Lett.* **88**, 096101 (2006).
- [84] H. Yamamoto, H. Kasajima, W. Yokoyama, H. Sasabe, and C. Adachi, *Appl. Phys. Lett.* **86**, 083502 (2005).
- [85] V. Jankus, C.-J. Chiang, F. Dias, and A. P. Monkman, *Adv. Mater.* **25**, 1455 (2013).
- [86] D. Graves, V. Jankus, F. B. Dias, and A. Monkman, *Adv. Mater.* **24**, 2343 (2014).
- [87] W.-Y. Hung, G.-C. Fang, Y.-C. Chang, T.-Y. Kuo, P.-T. Chou, S.-W. Lin, and K.-T. Wong, *ACS Appl. Mater. Interfaces* **5**, 6826 (2013).
- [88] K. Goushi, K. Yoshida, K. Sato, and C. Adachi, *Nat. Photon.* **6**, 253 (2012).
- [89] M. Sarma and K.-T. Wong, *ACS Appl. Mater. Interfaces* **10**, 19279 (2018).
- [90] P. Pander, S. Gogoc, M. Colella, P. Data, and F. B. Dias, *ACS Appl. Mater. Interfaces* **10**, 28796 (2018).
- [91] X.-K. Liu, Z. Chen, C.-Jun Zheng, C.-L. Liu, C.-S. Lee, F. Li, X.-M. Ou, and X.-H. Zhang, *Adv. Mater.* **27**, 2378 (2015).
- [92] J. Kalinowski, *Mat. Sci.-Pol.* **27**, 735 (2009).
- [93] G. Giro, M. Cocchi, J. Kalinowski, P. Di Marco, and V. Fattori, *Chem. Phys. Lett.* **318**, 137 (2000).
- [94] J. Kalinowski, M. Cocchi, D. Virgili, V. Fattori, J.A.G. Williams, *Chem. Phys. Lett.* **432**, 110 (2006).
- [95] M. Cocchi, D. Virgili, G. Giro, V. Fattori, and P. Di Marco, J. Kalinowski, Y. Shirota, *Appl. Phys. Lett.* **80**, 2401 (2002).
- [96] J. Kalinowski, M. Cocchi, D. Virgili, V. Fattori, and J. A. G. Williams, *Adv. Mater.* **19**, 4000 (2007).
- [97] M. Chapran et al., *ACS Appl. Mater. Interfaces* **9**, 4750 (2017).
- [98] G. Grybauskaite-Kaminskiene et al. *J. Mater. Chem. C* **6**, 1543 (2018).
- [99] X. Tang, X.-Y. Liu, Y. Yuan, Y.-J. Wang, H.-C. Li, Z.-Q. Jiang, and L.-S. Liao, *ACS Appl. Mater. Interfaces* **10**, 29840 (2018).
- [100] T. Zhang et al., *ACS Appl. Mater. Interfaces* **6**, 11907 (2014).
- [101] V. Jankus, P. Data, D. Graves, C. McGuinness, J. Santos, M. R. Bryce, F. B. Dias, and A. P. Monkman, *Adv. Funct. Mater.* **24**, 6178 (2014).

- [102] T. Zhang, B. Zhao, B. Chu, W. Li, Z. Su, X. Yan, C. Liu, H. Wu, F. Jin, and Y. Gao, *Org. Electron.* **25**, 6 (2015).
- [103] T. Zhang, B. Zhao, B. Chu, W. Li, Z. Su, X. Yan, C. Liu, H. Wu, Y. Gao, F. Jin, and F. Hou, *Sci. Rep.* **5**, 10234 (2015).
- [104] L. Duan, J. Qiao, Y. Sun, and Y. Qiu, *Adv. Mater.* **23**, 1137 (2011).
- [105] Y.-X. Zhang, B. Wang, Y. Yuan, Y. Hu, Z.-Q. Jiang, and L.-S. Liao, *Adv. Optical Mater.* **5**, 1700012 (2017).
- [106] C.-J. Shih, C.-C. Lee, T.-H. Yeh, S. Biring, K. K. Kesavan, N. R. Al Amin, M.-H. Chen, W.-C. Tang, S.-W. Liu, and K.-T. Wong, *ACS Appl. Mater. Interfaces* **10**, 24090 (2018).
- [107] J. Zhao, S. Yuan, X. Du, W. Li, C. Zheng, S. Tao, and X. Zhang, *Adv. Optical Mater.* **6**, 1800825 (2018).
- [108] J. Penga, X. Xua, X. J. Feng, and L. Lia, *J. Lumin.* **198**, 19 (2018).
- [109] Y.-T. Hung, Z.-Y. Chen, W.-Y. Hung, D.-G. Chen, and K.-T. Wong, *ACS Appl. Mater. Interfaces* **10**, 34435 (2018).
- [110] S. Ying, D. Yang, X. Qiao, Y. Dai, Q. Sun, J. Chen, T. Ahamad, S. M. Alshehri, and D. Ma, *J. Mater. Chem. C* **6**, 10793 (2018).
- [111] B. Zhao, H. Zhang, Y. Miao, Z. Wang, L. Gao, H. Wang, Y. Hao, B. Xu, and W. Li, *J. Mater. Chem. C* **5**, 12182 (2017).
- [112] Y.-S. Park, S. Lee, K.-H. Kim, S.-Y. Kim, J.-H. Lee, and J.-J. Kim, *Adv. Funct. Mater.* **23**, 4914 (2013).
- [113] S. Lee, K.-H. Kim, D. Limbach, Y.-S. Park, and J.-J. Kim, *Adv. Funct. Mater.* **23**, 4105 (2013).
- [114] I. Gozhyk, M. Boudreau, H. R. Haghghi, N. Djellali, S. Forget, S. Chénais, C. Ulysse, A. Brosseau, R. Pansu, J.-F. Audibert, S. Gauvin, J. Zyss, and M. Lebental, *Phys. Rev. B* **92**, 214202 (2015).
- [115] Y. Yang, G. A. Turnbull, and I. D. W. Samuel, *Appl. Phys. Lett.* **92**, 163306 (2008).
- [116] M. Morales-Vidal, P. G. Boj, J. M. Villalvilla, J. A. Quintana, Q. Yan, N.-T. Lin, X. Zhu, N. Ruangsapapichat, J. Casado, H. Tsuji, E. Nakamura, and M. A. Diaz-Garcia, *Nat. Commun.* **6**, 8458 (2015).
- [117] S.-J. Chang, X. Liu, T.-T. Lu, Y.-Y. Liu, J.-Q. Pan, Y. Jiang, S.-Q. Chu, W.-Y. Lai, and W. Huang, *J. Mater. Chem. C* **5**, 6629 (2017).
- [118] Q. Wei, Y. Li, J. Liu, Q. Fang, J. Li, X. Yan, L. Xie, Y. Qian, R. Xia, and W. Huang, *Adv. Optical Mater.* **5**, 1601003 (2017).
- [119] J.-H. Kim, M. Inoue, L. Zhao, T. Komino, S. Seo, J.-C. Ribierre, and C. Adachi, *Appl. Phys. Lett.* **106**, 053302 (2015).
- [120] K. Kuriki and Y. Koike, *Chem. Rev.* **102**, 2347 (2002).
- [121] J. Arrue, F. Jiménez, I. Ayesta, M. A. Illarramendi, and J. Zubia, *Polymers* **3**, 1162 (2011).

- [122] T. Kobayashi, J.-B. Savatier, G. Jordan, W. J. Blau, Y. Suzuki, and T. Kaino, *Appl. Phys. Lett.* **85**, 185 (2004).
- [123] T. Kobayashi and R. Hogan, *Appl. Phys. Lett.* **97**, 143303 (2010).
- [124] M. D. McGehee and A. J. Heeger, *Adv. Mater.* **12**, 1655 (2000).
- [125] I. D. W. Samuel and G. A. Turnbull, *Chem. Rev.* **107**, 1272 (2007).
- [126] C. Grivas and M. Pollnau, *Laser Photon. Rev.* **6**, 419 (2012).
- [127] S. Chénais and S. Forget, *Polym. Int.* **61**, 390 (2012).
- [128] O. Svelto and D. C. Hanna, *Principles of Lasers*, 5th edition, Springer New York Dordrecht Heidelberg London, 2010.
- [129] C. Karnutsch, C. Gyrtner, V. Haug, U. Lemmer, T. Farrell, B. S. Nehls, U. Scherf, J. Wang, T. Weimann, G. Heliotis, C. Pflumm, J. C. deMello, and D. D. C. Bradley, *Appl. Phys. Lett.* **89**, 201108 (2006).
- [130] C. Karnutsch, C. Pflumm, G. Heliotis, J. C. deMello, D. D. C. Bradley, J. Wang, T. Weimann, V. Haug, C. Gärtner, and U. Lemmer, *Appl. Phys. Lett.* **90**, 131104 (2007).
- [131] E. B. Namdas, M. Tong, P. Ledochowitsch, S. R. Mednick, J. D. Yuen, D. Moses, and A. J. Heeger, *Adv. Mater.* **21**, 799 (2009).
- [132] Y. Wang, G. Tsiminis, A. L. Kanibolotsky, P. J. Skabara, I. D.W. Samuel, and G. A. Turnbull, *Opt. Exp.* **21**, 14362 (2013).
- [133] J. C. Ribierre, G. Tsiminis, S. Richardson, G. A. Turnbull, H. S. Barcena, and P. L. Burn, *Appl. Phys. Lett.* **91**, 081108 (2007).
- [134] D.-H. Kim, A. D'Aléo, X.-K. Chen, A. D. S. Sandanayaka, D. Yao, L. Zhao, T. Komino, E. Zaborova, G. Canard, Y. Tsuchiya, E. Choi, J. W. Wu, F. Fages, J.-L. Brédas, J.-C. Ribierre, and C. Adachi, *Nat. Photon.* **12**, 98 (2018).
- [135] H. Nakanotani, T. Furukawa, T. Hosokai, T. Hatakeyama, and C. Adachi, *Adv. Optical Mater.* **5**, 1700051 (2017).
- [136] <https://www.ksop.kit.edu/visolas.php>.
- [137] I. D.W. Samuel, E. B. Namdas, and G. A. Turnbull, *Nat. Photon.* **3**, 546 (2009).
- [138] S. Z. Bisri, T. Takenobu, and Y. Iwasa, *J. Mater. Chem. C* **2**, 2827 (2014).
- [139] M. A. Baldo, R. J. Holmes, and S. R. Forrest, *Phys. Rev. B* **66**, 035321 (2002).
- [140] K. Yoshida, T. Matsushima, Y. Shiihara, H. Kuwae, J. Mizuno, and C. Adachi, *Appl. Phys. Lett.* **121**, 195503 (2017).
- [141] V. Coropcean, J. Cornil, D. A. da Silva Filho, Y. Olivier, R. Silbey, and J.-L. Brédas, *Chem. Rev.* **107**, 926 (2007).
- [142] C. Gärtner, C. Karnutsch, U. Lemmer, C. Pflumm, and Appl. Phys. Lett. **101**, 023107 (2007).
- [143] Y. Zhang and S. R. Forrest, *Phys. Rev. B* **84**, 241301 (2011).

- [144] A. S. D. Sandanayaka, L. Zhao, D. Pitrat, J.-C. Mulatier, T. Matsushima, C. Andraud, J.-H. Kim, J.-C. Ribierre, and C. Adachi, *Appl. Phys. Lett.* **108**, 223301 (2016).
- [145] A. S. D. Sandanayaka, K. Yoshida, M. Inoue, C. Qin, K. Goushi, J.-C. Ribierre, T. Matsushima, and C. Adachi, *Adv. Optical. Mater.* **4**, 834 (2016).
- [146] A. S. D. Sandanayaka, T. Matsushima, F. Bencheikh, K. Yoshida, M. Inoue, T. Fujihara, K. Goushi, J.-C. Ribierre, C. Adachi, *Sci. Adv.* **3**, 1602570 (2017).
- [147] J. Herrnsdorf, Y. Wang, J. J. D. McKendry, Z. Gong, D. Massoubre, B. Guilhabert, G. Tsiminis, G. A. Turnbull, I. D. W. Samuel, N. Laurand, E. Gu, and M. D. Dawson, *Laser Photon. Rev.* **7**, 1065 (2013).
- [148] Y. Yang, G. A. Turnbull, and I. D. W. Samuel, *Appl. Phys. Lett.* **92**, 163306 (2008).
- [149] Y. Liu, Y. Lu, X. Yang, X. Zheng, S. Wen, X. F. Wang, X. Vidal, J. Zhao, D. Liu, Z. Zhou, C. Ma, J. Zhou, J. A. Piper, P. Xi, and D. Jin, *Nature* **543**, 229 (2017).
- [150] U. Cho, D. P. Riordan, P. Ciepla, K. S. Kocherlakota, J. K. Chen, and P. B. Harbury, *Nat. Chem. Bio.* **14**, 15 (2018).
- [151] Y. Zhang, B. Chen, S. Xu, X. Li, J. Zhang, J. Sun, H. Zheng, L. Tong, G. Sui, H. Zhong, H. Xia, and R. Hua, *Sci. Rep.* **7**, 11849 (2017).
- [152] J.-N. Hao and B. Yan, *Adv. Funct. Mater.* **27**, 1603856 (2017).
- [153] H. Q. Ye, Z. Li, Y. Peng, C. C. Wang, T. Y. Li, Y. X. Zheng, A. Sapelkin, G. Adamopoulos, I. Hernández, P. B. Wyatt, and W. P. Gillin, *Nat. Mater.* **13**, 382 (2014).
- [154] J. Yang, M. B. J. Diemeer, C. Grivas, G. Sengo, A. Driessen, and M. Pollnau, *Laser Phys. Lett.* **7**, 650 (2010).
- [155] H. Kim, S. Beack, S. Han, M. Shin, T. Lee, Y. Park, K. S. Kim, A. K. Yetisen, S. H. Yun, W. Kwon, and S. K. Hahn, *Adv. Mater.* **30**, 1701460 (2018).
- [156] W. Zhang, Y. Shen, Y. Meng, and M. Gong, *Opt. Comm.* **401**, 29 (2017).
- [157] S. Chénais, F. Druon, S. Forget, F. Balembois, and P. Georges, *Prog. Quant. Electron.* **30**, 89 (2006).
- [158] X. Ding, R. Wanga, H. Zhang, X.-Y. Yu, W.-Q. Wena, P. Wang, and J.-Q. Yao, *Opt. Comm.* **282**, 981 (2009).
- [159] A. M. Rodin, M. Grishin, and A. Michailovas, *Opt. Laser Tech.* **76**, 46 (2016).
- [160] F. Druon, S. Chénais, P. Raybaut, F. Balembois, and P. Georges, *Opt. Lett.* **27**, 197 (2002).
- [161] J.-C. G. Bünzli and C. Piguet, *Chem. Soc. Rev.* **34**, 1048 (2005).
- [162] L. Armelao, S. Quici, F. Barigelletti, G. Accorsi, G. Bottaro, M. Cavazzini, and E. Tondello, *Coord. Chem. Rev.* **254**, 487 (2010).
- [163] A. D'Aléo, F. Pointillart, L. Ouahab, C. Andraud, and O. Maury, *Coord. Chem. Rev.* **256**, 1604 (2012).
- [164] A. D'Aléo, J. Xu, E. G. Moore, C. J. Jocher, and K. N. Raymond, *Inorg. Chem.* **47**, 6109 (2008).

- [165] L. J. Daumann, D. S. Tatum, C. M. Andolina, J. I. Pacold, A. D'Aléo, G.-I. Law, Jide Xu, and K. N. Raymond, *Inorg. Chem.* **55**, 114 (2016).
- [166] A. D'Aléo, A. Picot, A. Beeby, J. A. G. Williams, B. L. Guennic, C. Andraud, and O. Maury, *Inorg. Chem.* **47**, 10258 (2008).
- [167] C. Koeppen, S. Yamada, G. Jiang, and A. F. Garito, *J. Opt. Soc. Am. B* **14**, 155 (1997).
- [168] S. Yanagida, Y. Hasegawa, K. Murakoshi, Y. Wada, N. Nakashima, and T. Yamanaka, *Coord. Chem. Rev.* **171**, 461 (1998).
- [169] J. Yang, M. B. J. Diemeer, C. Grivas, G. Sengo, A. Driessen, and M. Pollnau, *Laser Phys. Lett.* **7**, 650 (2010).
- [170] C. Grivas, J. Yang, M. B. J. Diemeer, A. Driessen, and M. Pollnau, *Opt. Lett.* **35**, 1983 (2010).
- [171] P. B. Glover, A. P. Bassett, P. Nockemann, B. M. Kariuki, R. Van Deun, and Z. Pikramenou, *Chem. Eur. J.* **13**, 6308 (2007).
- [172] J. H. Melman, C. Rohde, T. J. Emge, and J. G. Brennan, *Inorg. Chem.* **41**, 28 (2002).
- [173] Y. Hasegawa, Y. Kimura, K. Murakoshi, Y. Wada, J.-H. Kim, N. Nakashima, T. Yamanaka, and S. Yanagida, *J. Phys. Chem.* **100**, 10201 (1996).
- [174] S. Chen, R.-Q. Fan, S. Gao, X. Wang, Y.-L. Yang, *J. Lumin.* **149**, 75 (2014).
- [175] K. Binnemans, *Chem. Rev.* **109**, 4283 (2009).
- [176] J. Kido and Y. Okamoto, *Chem. Rev.* **102**, 2357 (2002).
- [177] Y. Hasegawa, M. Yamamuro, Y. Wada, N. Kanehisa, Y. Kai, and S. Yanagida, *J. Phys. Chem. A* **107**, 1697 (2003).
- [178] Z. Hong, W. Li, D. Zhao, C. Liang, X. Liu, J. Peng, and D. Zhao, *Syn. Met.* **104**, 165, (2000).
- [179] A. N. Aslandukov, V. V. Utochnikova, D. O. Goriachiy, A. A. Vashchenko, D. M. Tsybarenko, and M. Hoffmann, *Dalton Trans.* **47**, 16350 (2018).
- [180] Z. Ahmed and K. Iftikhar, *Inorg. Chem.* **54**, 11209 (2015).
- [181] S. Zhang, G. A. Turnbull, and I. D. W. Samuel, *Adv. Optical Mater.* **2**, 343 (2014).
- [182] Y. Hasegawa, S. Natori, J. Fukudome, T. Nagase, T. Kobayashi, T. Nakanishi, Y. Kitagawa, K. Fushimi, and H. Naito, *J. Phys. Chem. C* **122**, 9599 (2018).
- [183] G.-L. Law, K.-L. Wong, H.-L. Tam, K.-W. Cheah, and W.-T. Wong, *Inorg. Chem.* **48**, 10492 (2009).
- [184] J. Mezyk, W. Mróz, A. Mech, U. Giovanella, F. Meinardi, C. Botta, B. Vercellic, and R. Tubino, *Phys. Chem. Chem. Phys.* **11**, 10152 (2009).
- [185] P.P. Lima, F.A.A. Paz, C.D.S. Brites, W.G. Quirino, C. Legnani, M. Costa e Silva d, R.A.S. Ferreira, S.A. Júnior, O.L. Malta, M. Cremona, and L.D. Carlos, *Org. Electron.* **15**, 798 (2014).
- [186] H. Xua, Q. Sunb, Z. Anb, Y. Weia, X. Liu, *Coord. Chem. Rev.* **293–294**, 228 (2015).
- [187] J.-C. G. Bünzli and S. V. Eliseeva, *J. Rare Earth* **28**, 824 (2010).

- [188] J.-C. G. Bünzli and J. Lumin. **170**, 866 (2016).
- [189] A. D'Aléo, A. Bourdolle, S. Brustlein, T. Fauquier, A. Grichine, A. Duperray, P. L. Baldeck, C. Andraud, S. Basselet, and O. Maury, *Angew. Chem. Int. Ed.* **51**, 6622 (2012).
- [190] Y. Fan, P. Wang, Y. Lu, R. Wang, L. Zhou, X. Zheng, X. Li, J. A. Piper, and F. Zhang, *Nat. Nanotech.* **13**, 941 (2018).
- [191] J. X. Hu, S. Karamshuk, J. Gorbaciova, H. Q. Ye, H. Lu, Y. P. Zhang, Y. X. Zheng, X. Liang, I. Hernández, P. B. Wyatt, and W. P. Gillin, *Sci. Rep.* **8**, 3226 (2018).
- [192] C. Maurizio, E. Trave, G. Perotto, V. Bello, D. Pasqualini, P. Mazzoldi, G. Battaglin, T. Cesca, C. Scian, and G. Mattei, *Phys. Rev. B* **83**, 195430 (2011).
- [193] S. Haas, A. Hoell, R. Wurth, C. Rüssel, P. Boesecke, and U. Vainio, *Phys. Rev. B* **81**, 184207 (2010).
- [194] B. Zhou and E. Y.-B. Pun, *Opt. Lett.* **36**, 2958 (2011).
- [195] N. Li, E. S. Magden, Z. Su, N. Singh, A. Ruocco, M. Xin, M. Byrd, P. T. Callahan, J. D. B. Bradley, C. Baiocco, D. Vermeulen, and M. R. Watts, *Opt. Exp.* **26**, 2220 (2018).
- [196] X. Liu, B. J. Chen, E. Y. B. Pun, and H. Lin, *J. Appl. Phys. Lett.* **111**, 116101 (2012).
- [197] H. He, L. Si, Y. Zhong, and M. Dubey, *Chem. Commun.* **48**, 1886 (2012).
- [198] C. Doffek and M. Seitz, *Angew. Chem. Int. Ed.* **54**, 9719 (2015).
- [199] X. Li, Y. Yu, P. Luo, W. Zhang, Z. Guo, and X. Guan, *Opt. Mater. Exp.* **7**, 1007 (2017).
- [200] M.A. Lourenço, M. M. Milošević, A. Gorin, R. M. Gwilliam and K. P. Homewood, *Sci. Rep.* **6**, 37501 (2016).
- [201] H. T. Tong, D. Demichi, K. Nagasaka, T. Suzuki, and Y. Ohishi, *Opt. Commun.* **415**, 87 (2018).
- [202] L. A.O. Nunes, A. S. Souza, L. D. Carlos, and O. L. Malta, *Opt. Mater.* **63**, 42 (2017).
- [203] H. P. Santos, E. S. Gomes, M. V. dos Santos, K. A. D'Oliveira, A. Cuin, J. S. Martins, W. G. Quirino, and L. F. Marques, *Inorg. Chim. Acta* **484**, 60 (2019).
- [204] B. Li, G. Fu, J. Guan, Y. He, L. Liu, K. Zhang, J. Guo, W. Feng, and X. Lü, *J. Lumin.* **204**, 30 (2018).
- [205] K. Jinnai, R. Kabe, and C. Adachi, *Chem. Commun.* **53**, 5457 (2017).
- [206] Z. Ahmed, R. E. Aderne, J. Kai, H. I.P. Chavarria, and M. Cremona, *Thin Solid Films* **620**, 34 (2016).
- [207] P. Martín-Ramos, C. Coya, Á. L. Álvarez, M. R. Silva, C. Zaldo J. A. Paixão, P. Chamorro-Posada, and J. Martín-Gil, *J. Phys. Chem. C* **117**, 10020 (2013).
- [208] P. Martín-Ramos, M. D. Miranda, M. R. Silva, M. E. S. Eusebio, V. Lavín, J. Martín-Gil, *Polyhedron* **65**, 187 (2013).
- [209] M. A. Katkova, A. P. Pushkarev, T. V. Balashova, A. N. Konev, G. K. Fukin, S. Yu. Ketkov, and M. N. Bochkarev, *J. Mater. Chem.* **21**, 16611 (2011).
- [210] C. H. Cheng, J. Wang, Z. J. Du, S. H. Shi, Z. Q. Fan, D. F. Geng, R. S. Shen, Y. M. Luo, and G. T. Du, *J. Lumin.* **130**, 2293 (2010).

- [211] N. M. Shavaleev, R. Scopelliti, F. Gumy, and J.-C. G. Bünzli, *Inorg. Chem.* **47**, 9055 (2008).
- [212] T.-S. Kang, B. S. Harrison, T. J. Foley, A. S. Knefely, J. M. Boncella, J. R. Reynolds, and K. S. Schanze, *Adv. Mater.* **15**, 1093 (2003).
- [213] S.W. Magennis, A.J. Ferguson, T. Bryden, T.S. Jones, A. Beeby, I.D.W. Samuel, *Syn. Met.* **138**, 463 (2003).
- [214] B. Hu, L. Yan, and M. Shao, *Adv. Mater.* **21**, 1500 (2009).
- [215] C. Boehme and J. Lupton, *Nat. Nanotech.* **8**, 612 (2013).
- [216] D. P. Waters, G. Joshi, M. Kavand, M. E. Limes, H. Malissa, P. L. Burn, J. M. Lupton, and C. Boehme, *Nat. Phys.* **11**, 910 (2015).
- [217] V. A. Dediu, L. Hueso, I. Bergenti, and C. Taliani, *Nat. Mater.* **8**, 707 (2009).
- [218] M. Wohgenannt, M. E. Flatte, N. J. Harmon, F. Wang, A. D. Kent, and F. Marcia, *Phil. Trans. R. Soc. A* **373**, 201440326 (2015).
- [219] T. D. Nguyen, E. Ehrenfreund, and Z. V. Vardeny, *Science* **337**, 204 (2014).
- [220] D. Wu, Z. H. Xiong, X. G. Li, Z. V. Vardeny, and J. Shi, *Phys. Rev. Lett.* **95**, 016802 (2005).
- [221] T. S. Santos, J. S. Lee, P. Migdal, I. C. Lekshmi, B. Satpati, and J. S. Moodera, *Phys. Rev. Lett.* **95**, 016601 (2007).
- [222] R. Geng, H. M. Luong, T. T. Daugherty, L. Hornak, and T. D. Nguyen, *J. Sci. Adv. Mater. Devices* **1**, 256 (2016).
- [223] R. Geng, T. T. Daugherty, K. Do, H. M. Luong, and T. D. Nguyen, *J. Sci. Adv. Mater. Devices* **1**, 128 (2016).
- [224] J. Kalinowski, M. Cocchi, D. Virgili, V. Fattori, and P. Di Marco, *Phys. Rev. B* **70**, 205303 (2004).
- [225] T. D. Nguyen, B. R. Gautam, E. Ehrenfreund, and Z. V. Vardeny, *Phys. Rev. Lett.* **105**, 166804 (2010).
- [226] R. Geng, R. C. Subedi, H. M. Luong, M. T. Pham, W. Huang, X. Li, K. Hong, M. Shao, K. Xiao, L. A. Hornak, and T. D. Nguyen, *Phys. Rev. Lett.* **120**, 086602 (2018).
- [227] S. van Reenen, S. P. Kersten, S. H. W. Wouters, M. Cox, P. Janssen, B. Koopmans, P. A. Bobbert, and M. Kemerink, *Phys. Rev. B* **2**, 125203 (2013).
- [228] Y. Wang, K. Sahin-Tiras, N. J. Harmon, M. Wohlgenannt, and M. E. Flatté, *Phys. Rev. X* **6**, 011011 (2016).
- [229] H. Kraus, S. Bange, F. Frunder, U. Scherf, C. Boehme, and J. M. Lupton, *Phys. Rev. B* **95**, 241201 (2017).
- [230] S. P. Kresten, A. J. Schellekens, B. Koopmans, and P. A. Bobbert, *Phys. Rev. Lett.* **106**, 197402 (2011).
- [231] B. R. Gautam, T. D. Nguyen, E. Ehrenfreund, and Z. V. Vardeny, *Phys. Rev. B* **85**, 205207 (2012).
- [232] D. Wu, Z. H. Xiong, X. G. Li, Z. V. Vardeny, and J. Shi, *Phys. Rev. Lett.* **95**, 016802 (2005).

- [233] N. Lua, L. Lia, D. Geng, and M. Liu, *Org. Electron.* **61**, 223 (2018).
- [234] V.N. Prigodin, J.D. Bergeson, D.M. Lincoln, and A.J. Epstein, *Syn. Met.* **156**, 757 (2006).
- [235] J. Kalinowski, J. Szmytkowski, and W. Stampor, *Chem. Phys. Lett.* **378**, 380 (2003).
- [236] J. Wilkinson, A. H. Davis, K. Bussmann, and J. P. Long, *Appl. Phys. Lett.* **86**, 111109 (2005).
- [237] B. Hu and Y. Wu, *Nat. Mater.* **6**, 985 (2007).
- [238] J. Szmytkowski, W. Stampor, J. Kalinowski, and Z. H. Kafafi, *Appl. Phys. Lett.* **80**, 1465 (2002).
- [239] P.A. Bobbert, T.D. Nguyen, F.W.A. van Oost, B. Koopmans, and M. Wohlgenannt, *Phys. Rev. Lett.* **99**, 216801 (2007).
- [240] N. J. Harmon and M. E. Flatté, *Phys. Rev. Lett.* **108**, 186602 (2012).
- [241] V. Ern and R. E. Merrifield, *Phys. Rev. Lett.* **21**, 609 (1968).
- [242] J. Y. Song, N. Stingelin, A. J. Drew, T. Kreouzis, and W. P. Gillin, *Phys. Rev. B* **82**, 085205 (2010).
- [243] P. Desai, P. Shakya, T. Kreouzis, and W. P. Gillin, *Phys. Rev. B* **75**, 094423 (2007).
- [244] P. Desai, P. Shakya, T. Kreouzis, and W. P. Gillin, *Phys. Rev. B* **76**, 235202 (2007).
- [245] A. H. Devir-Wolfman, B. Khachatryan, B. R. Gautam, L. Tzabary, A. Keren, N. Tessler, Z. V. Vardeny, and E. Ehrenfreund, *Nat. Commun.* **5**, 4529 (2014).
- [246] F. J. Wang, H. Bäessler, and Z. V. Vardeny, *Phys. Rev. Lett.* **101**, 236805 (2008).
- [247] P. Berini and I. De Leon, *Nat. Photon.* **6**, 16 (2012).
- [248] Rupert F. Oulton, *Mater. Today* **15**, 592 (2012).
- [249] R.-M. Ma, R. F. Oulton, V. J. Sorger, and X. Zhang, *Laser Photon. Rev.* **7**, 1 (2013).
- [250] T. P. H. Sidiropoulos, R. Röder, S. Geburt, O. Hess, S. A. Maier, C. Ronning, and R. F. Oulton, *Nat. Phys.* **10**, 870 (2014).
- [251] J. B. Khurgin and G. Sun, *Nat. Photon.* **8**, 468 (2014).
- [252] M. Ambati, S. H. Nam, E. Ulin-Avila, D. A. Genov, G. Bartal, and X. Zhang, *Nano. Lett.* **8**, 3998 (2008).
- [253] S. Nair, C. Escobedo, and R. G. Sabat, *ACS Sens.* **2**, 379 (2017).
- [254] S. Nair, J. Gomez-Cruz, Á. Manjarrez-Hernandez, G. Ascanio, R. G. Sabat, and C. Escobedo, *Sensors* **18**, 3634 (2018).
- [255] O. Tokel, F. Inchi, and U. Demirchi, *Chem. Rev.* **114**, 5728 (2014).
- [256] M. Bauch, K. Toma, M. Toma, Q. Zhang, and J. Dostalek, *Plasmonics* **9**, 781 (2014).
- [257] K. Ueno, T. Oshikiri, Q. Sun, X. Shi, and H. Misawa, *Chem. Rev.* **118**, 2955 (2018).
- [258] P. Yu, Yisen Yao, J. Wu, X. Niu, A. L. Rogach, and Z. Wang, *Sci. Rep.* **7**, 7696 (2017).

- [259] K. N'Konou, V. Many, C. M. Ruiz, M. Treguer-Delapierre, and P. Torchio, *J. Appl. Phys.* **123**, 063102 (2018)
- [260] K. Chan, M. Wright, N. Elumalai, A. Uddin, and S. Pillai, *Adv. Optical Mater.* **5**, 1600698 (2017).
- [261] T. Kim, S. Kang, J. Heo, S. Cho, J. Won Kim, A. Choe, B. Walker, R. Shanker, H. Ko, and J. Young Kim, *Adv. Mater.* **30**, 1800659 (2018).
- [262] B. Munkhbat, H. Pöh, P. Denk, T. A. Klar, M. Clark, and S. C. Hrelescu, *Adv. Optical Mater.* **4**, 772 (2016).
- [263] Y. Xu, H. Zhou, R. Zhang, Y. Liu, Q. Zhang, S. Zhang, L. Zhang, S. Chen, L. Deng, Y. Qian, L. Wang, and W. Huang, *AIP Advances* **5**, 067121 (2015).
- [264] F. Liu and J.-M. Nunzi, *Appl. Phys. Lett.* **99**, 123302 (2011).
- [265] M. Kauranen and A. V. Zayats, *Nat. Photon.* **6**, 737 (2012).
- [266] W. Cai, A. P. Vasudev, M. L. Brongersma, *Science* **333**, 1720 (2011).
- [267] J. D. Cox and F. J. G. de Abajo, *Nat. Commun.* **5**, 5725 (2014).
- [268] C.-Y. Wang, H.-Y. Chen, L. Sun, W.-L. Chen, Y.-M. Chang, H. Ahn, X. Li, and S. Gwo, *Nat. Commun.* **6**, 7734 (2015).
- [269] K. Thyagarajan, C. Santschi, P. Langlet, and O. J. F. Martin, *Adv. Optical Mater.* **4**, 871 (2016).
- [270] K. Rong, F. Gan, K. Shi, S. Chu, and J. Chen, *Adv. Mater.* **30**, 1706546 (2018).
- [271] D. Yu. Fedyanin, D. I. Yakubovsky, R. V. Kirtaev, and V. S. Volkov, *Nano Lett.* **16**, 362 (2016).
- [272] T. J. Duffin, M. P. Nielsen, F. Diaz, S. Palomba, S. A. Maier, and R. F. Oulton, *Opt. Lett.* **41**, 155 (2016).
- [273] D. Ansell, I. P. Radko, Z. Han, F. J. Rodriguez, S. I. Bozhevolnyi, and A. N. Grigorenko, *Nat. Commun.* **6**, 8846 (2015).
- [274] S. Hayashi and T. Okamoto, *J. Phys. D: Appl. Phys.* **45**, 433001 (2012).
- [275] S. A. Maier, *Plasmonics: Fundamentals and Applications*, Springer, 2007.
- [276] N. J. Halas, S. Lal, W.s. Chang, S. Link, and P. Nordlander, *Chem. Rev.* **111**, 3913 (2011).
- [277] X. Huang, S. Neretina, and M. El-Sayed, *Adv. Meter.* **21**, 1 (2009).
- [278] M. A. Noginov, G. Zhu, A. M. Belgrave, R. Bakker, V. M. Shalaev, E. E. Narimanov, S. Stout, E. Herz, T. Suteewong, and U. Wiesner, *Nature* **460**, 1110 (2009).
- [279] L. H. Slooff, A. Polman, F. Cacialli, R. H. Friend, G. A. Hebbink, F. C. J. M. van Veggel, and D. N. Reinhoudt, *Appl. Phys. Lett.* **78**, 2122 (2001).
- [280] A. O'Riordan, R. Van Deun, E. Mairiaux, S. Moynihan, P. Fias, P. Nockemann, K. Binnemans, G. Redmond, *Thin Solid Films* **516**, 5098 (2008).
- [281] A. O'Riordan, E. O'Connor, S. Moynihan, P. Nockemann, P. Fias, R. Van Deun, D. Cupertino, P. Mackie, G. Redmond, *Thin Solid Films* **497**, 299 (2006).

- [282] Y. Kawamura, Y. Wada, Y. Hasegawa, M. Iwamuro, T. Kitamura, S. Yanagida, *Appl. Phys. Lett.* **74**, 3245 (1999).
- [283] Y. Kawamura, Y. Wada, and S. Yanagida, *Jpn. J. Appl. Phys.* **40**, 350 (2001).
- [284] O.M. Kheris, R. J. Curry, M. Somerton, and W. P. Gillin, *J. Appl. Phys.* **88**, 777 (2000).
- [285] Z. Li, J. Yu, L. Zhou, R. Deng, and H. Zhang, *Inorg. Chem. Commun.* **12**, 151 (2009).
- [286] Y. J. Cho and J. Y. Lee, *Adv. Mater.* **23**, 4568 (2011).
- [287] H. Nakanotani, T. Higuchi, T. Furukawa, K. Masui, K. Morimoto, M. Numata, H. Tanaka, Y. Sagara, T. Yasuda, and C. Adachi, *Nature Commun.* **5**, 4016 (2014).
- [288] J. Lee, N. Chopra, S.-H. Eom, Y. Zheng, J. Xue, F. So, and J. Shi, *Appl. Phys. Lett.* **93**, 123306 (2008).
- [289] J. C. Ribierre, A. Ruseckas, K. Knights, S.V. Staton, N. Cumpstey, P. L. Burn, and I. D.W. Samuel, *Phys. Rev. Lett.* **100**, 017402 (2008).
- [290] G. R. Choppin and D. R. Peterman, *Coord. Chem. Rev.* **174**, 283 (1998).
- [291] Z.-Q. Chen, F. Ding, Z.-Q. Bian, and C.-H. Huang, *Org. Electron.* **11**, 369 (2010).
- [292] B. W. D'Andrade, S. Datta, S. R. Forrest, P. Djurovich, E. Polikarpov, and M. E. Thompson, *Org. Electron.* **6**, 11 (2005).
- [293] P. I. Djurovich, E. I. Mayo, S. R. Forrest, and M. E. Thompson, *Org. Electron.* **10**, 515 (2009).
- [294] M.-H. Tsai, Y.-H. Hong, C.-H. Chang, H.-C. Su, C.-C. Wu, A. Matoliukstyte, J. Simokaitiene, S. Grigalevicius, J. V. Grazulevicius, and C.-P. Hsu, *Adv. Mater.* **19**, 862 (2007).
- [295] H. Xu, L.-H. Wang, X.-H. Zhu, K. Yin, G.-Y. Zhong, X.-Y. Hou, and W. Huang, *J. Phys. Chem. B* **110**, 3023 (2006).
- [296] F.J. Steemers, W. Verboom, D.N. Reinhoudt, E.B. van der Tal, and J. W. Verhoeven, *J. Am. Chem. Soc.* **117**, 9408 (1995).
- [297] K. S. Yook and J. Y. Lee, *Org. Electron.* **12**, 1711 (2011).
- [298] S. Scholz, D. Kondakov, B. Lüssem, and K. Leo, *Chem. Rev.* **115**, 8449 (2015).
- [299] E. Gautier-Thianche, C. Sentein, A. Lorin, C. Denis, P. Raimond, and J.M. Nunzi, *J. Appl. Phys.* **83**, 4236 (1998).
- [300] T. Tsuboi, S.-W. Liu, M.-F. Wu, and C.-T. Chen, *Org. Electron.* **10**, 1372 (2009).
- [301] J.C. Ribierre, T. Aoyama, T. Muto, Y. Imase, and T. Wada, *Org. Electron.* **9**, 396 (2008).
- [302] B. Zhao, H. Zhang, Y. Miao, Z. Wang, L. Gao, H. Wang, Y. Hao, B. Xu, and W. Li, *J. Mater. Chem. C* **5**, 12182 (2017).
- [303] T.W. Canzler and J. Kido, *Org. Electron.* **7**, 29 (2006).
- [304] C. Adachi, M. A. Baldo, and S. R. Forrest, *J. Appl. Phys.* **87**, 8049 (2000).
- [305] S. Zhang, G.A. Turnbull, I.D.W. Samuel, *Org. Electron.* **13**, (2012) 3091.

- [306] M. Pietraszkiewicz, M. Maciejczyk, I.D.W. Samuel, and S. Zhang, *J. Mater. Chem. C* **1**, 8028 (2013).
- [307] L. Zhang, B. Li, L. Zhang, and Z. Su, *ACS Appl. Mat. Interfaces* **9**, 1852 (2009).
- [308] J. Yu, L. Zhou, H. Zhang, Y. Zheng, H. Li, R. Deng, Z. Peng, and Z. Li, *Inorg. Chem.* **44**, 1611 (2005).
- [309] Z. Chen, F. Ding, F. Hao, Z. Bian, B. Ding, Y. Zhu, F. Chen, and C. Huang, *Org. Electron.* **10**, 939 (2009).
- [310] J. Chen, C. Shi, Q. Fu., F. Zhao, Y. Hu, Y. Feng, and D. Ma, *J. Mater. Chem.* **22**, 5164 (2012).
- [311] J.-W. Kang, S.-H. Lee, H.-D. Park, W.-I.K. Jeong, K.-M. Yoo, Y.-S. Park, and J.-J. Kim, *Appl. Phys. Lett.* **90**, 223508 (2007).
- [312] X. Du, X. Yang, J. Zhao, H. Lin, C. Zheng, and S. Tao, *Org. Electron.* **38**, 344 (2016).
- [313] X. Liu, B. Yao, Z. Zhang, X. Zhao, B. Zhang, W.-Y. Wong, Y. Cheng, and Z. Xie, *J. Mater. Chem. C* **4**, 5787 (2016).
- [314] D.-Y. Zhou, L.-S. Cui, Y.-J. Zhang, L.-S. Liao, and H. Aziz, *Appl. Phys. Lett.* **105**, 153302 (2014).
- [315] H. Wei, G. Yu, Z. Zhao, Z. Liu, Z. Bian, and C. Huang, *Dalton. Trans.* **42**, 8951 (2013).
- [316] S. Penna, A. Reale, R. Pizzoferrato, G. M. Tosi Belleffi, D. Musella, and W. P. Gillin, *Appl. Phys. Lett.* **91**, 021106 (2007).
- [317] F. X. Zang, W. L. Li, Z. R. Hong, H. Z. Wei, M. T. Li, and X. Y. Sun, *Appl. Phys. Lett.* **84**, 5115 (2004).
- [318] R. Nagata, H. Nakanotani, and C. Adachi, *Adv. Mater.* **29**, 1604265 (2016).
- [319] A. Graf, C. Murawski, Y. Zakharko, J. Zaumseil, and M. C. Gather, *Adv. Mater.* **30**, 1706711 (2018).
- [320] Y. Yin, X. Piao, Y. Li, Y. Wang, J. Liu, K. Xu, and W. Xie, *Appl. Phys. Lett.* **101**, 063306 (2012).
- [321] J. Lee, J.-I. Lee, J. Y. Lee, and H. Y. Chu, *Appl. Phys. Lett.* **94**, 193305 (2009).
- [322] Q. Xin, W. L. Li, G. B. Che, W. M. Su, X. Y. Sun, B. Chu, and B. Li, *Appl. Phys. Lett.* **89**, 223524 (2006).
- [323] M. Mergani, A. Shahalizad, S. Ahmadi-Kandjani, and M. S. Zakerhamidi, *Phys. Scr.* **T157**, 014028 (2013).
- [324] T. Tsuboi, S.-W. Liu, M.-F. Wu, and C.-T. Chen, *Org. Electron.* **10**, 1327 (2009).
- [325] D. Graves, V. Jankus, F. B. Dias, and A. Monkman, *Adv. Funct. Mater.* **24**, 2343 (2014).
- [326] L. Pereira, *Organic Light-Emitting Diodes: The use of Rare-Earth and Transition Metals*, Pan Stanford Publishing Pte. Ltd. (2012).
- [327] H. Xu, L.-H. Wang, X.-H. Zhu, K. Yin, G.-Y. Zhong, X.Y. Hou, and W. Huang, *J. Phys. Chem. B*, **110**, 3023 (2006).
- [328] C.-H. Huang, *Rare Earth Coordination Chemistry: Fundamentals and Applications*, John Wiley & Sons, 592 pp (2010).

- [329] C.-J. Sun, Y. Wu, Z. Xu, B. Hu, J. Bai, J.-P. Wang, and J. Shen, *Appl. Phys. Lett.* **90**, 232110 (2007).
- [330] M. C. Traub, W. Longsine, and V. N. Truskett, *Annu. Rev. Chem. Biomol. Eng.* **7**, 583 (2016).
- [331] K. G. Yager and C. J. Barrett, *Curr. Opin. Solid State Mater. Sci.* **5**, 487 (2001).
- [332] P. Lefin, C. Fiorini, and J.-M. Nunzi, *Pure Appl. Opt.* **7**, 71 (1998).
- [333] C. J. Barrett and A. L. Natansohn, *J. Phys. Chem.* **100**, 8836 (1996).
- [334] S. Ahmadi-Kandjani, R. Barille, S. Dabos-Seignon, J.-M. Nunzi, E. Ortyl and S. Kucharski, *Opt. Lett.* **30**, 1986 (2005).
- [335] D. Roy, J. N. Cambre, and B. S. Sumerlin, *Prog. Poly. Sci.* **35**, 278 (2010).
- [336] J. Jefferies and R. G. Sabat, *Prog. Photovoltaics* **22**, 648 (2014).
- [337] C. Hubert, C. Fiorini-Debuisschert, I. Hassiaoui, L. Rocha, and P. Raimond, and J.-M. Nunzi, *Appl. Phys. Lett.* **87**, 191105 (2005).
- [338] J. P. Monteiro, J. Ferreira, R. G. Sabat, P. Rochon, M. J. L. Santos, E. M. Giroto, *Sens. Actu. B* **174**, 270 (2012).
- [339] L. Rocha, V. Dumarcher, C. Denis, P. Raimond, C. Fiorini, J.-M. Nunzi, *J. Appl. Phys.* **89**, 3067 (2001).
- [340] S. K. Yesodha, C. K. S. Pillai, and N. Tsutsumi, *Prog. Polym. Sci.* **29**, 45 (2004).
- [341] I. Papagiannouli, K. Iliopoulos, D. Gindre, B. Sahraoui, O. Krupka, V. Smokal, A. Kolendo, and S. Couris, *Chem. Phys. Lett.* **554**, 107 (2012).
- [342] R. Kirby, R. G. Sabat, J.-M. Nunzi, and O. Lebel, *Mater. Chem. C* **2**, 841 (2014).
- [343] J. M. Lupton, B. J. Matterson, I. D. W. Samuel, M. J. Jory, and W. L. Barnes, *Appl. Phys. Lett.* **77** (2000) 3340.
- [344] P. A. Hobson, J. A. E. Wasey, I. Sage, and W. L. Barnes, *IEEE J. Selected Topics Quant. Electron.* **8**, 378 (2002).
- [345] C.-W. Chen, S.-Y. Hsiao, C.-Y. Chen, H.-W. Kang, Z.-Y. Huang, and H.-W. Lin, *J. Mater. Chem. A* **3**, 9152 (2015).
- [346] A. D. Rakić, A. B. Djurišić, J. M. Elazar, and M. L. Majewski, *Appl. Opt.* **37**, 5271 (1998).
- [347] Y.-G. Bi, J. Feng, Y.-S. Liu, Y.-F. Li, Y. Chen, X.-L. Zhang, X.-C. Han, and H.-B. Sun, *Sci. Rep.* **4**, 7108 (2014).
- [348] D. E. Walker, M. Major, M. B. Yazdi, A. Klyszcz, M. Haeming, K. Bonrad, C. Melzer, W. Donner, and H. von Seggern, *ACS Appl. Mater. Interfaces* **4**, 6835 (2012).
- [349] A. A. Khosroabadi, P. Gangopadhyay, B. Duong, J. Thomas, A. K. Sigdel, J. J. Berry, T. Gennett, N. Peyghambarian, and R. A. Norwood, *Phys. Status Solidi A* **210**, 831 (2013).
- [350] F. Wang, Z. Tan, and Y. Li, *Energy Environ. Sci.* **8**, 1059 (2015).
- [351] C.-C. Chueh, C.-Z. Li, and A. K.-Y. Jen, *Energy Environ. Sci.* **8**, 1160 (2015).

[352] K. Zilberberg, J. Meyer, and T. Riedl, *J. Mater. Chem. C* **1**, 4796 (2013).

[353] B. Lüssem, M. Riede, and K. Leo, *Phys. Status Solidi A* **210**, 9 (2013).

[354] J. Kim, H.-J. Park, S.-I. Na, Y.-Y. Noh, and D.-Y. Kim, *Jpn. J. Appl. Phys.* **53**, 08NF02 (2014).